Spring 1-1-2012

Observational and Modeling Study of Polar Middle Atmosphere Dynamics and Thermal Structures

Bo Tan
University of Colorado at Bo, bo.tan@colorado.edu

Observational and Modeling Study of Polar Middle Atmosphere Dynamics and Thermal Structures

by

Bo Tan

B.S., Peking University, 2006

M.S., University of Colorado at Boulder, 2009

A thesis submitted to the

Faculty of the Graduate School of the

University of Colorado in partial fulfillment

of the requirements for the degree of

Doctor of Philosophy

Department of Aerospace Engineering Sciences

2012

This thesis entitled:
Observational and Modeling Study of Polar Middle Atmosphere Dynamics and Thermal Structures
written by Bo Tan
has been approved for the Department of Aerospace Engineering Sciences

_____
Professor Xinzhao Chu (Chair)

_____
Professor Han-Li Liu

Date _____

The final copy of this thesis has been examined by the signatories, and we find that both the content and the form meet acceptable presentation standards of scholarly work in the above mentioned discipline.

Tan, Bo (Ph.D., Aerospace Engineering Sciences)

Observational and Modeling study of Polar Middle Atmosphere Dynamics and Thermal Structures

Thesis advised by Professors Xinzhao Chu and Han-Li Liu

A middle atmosphere temperature benchmark in the polar region is critical to monitoring the climate change. However, it is very challenging to establish such a benchmark because it is difficult to observe temperatures in the polar region and numerous factors affect the temperature variations. Ground-base lidars are capable of providing high-resolution and long-duration measurements of temperatures in the polar region, which is critical in advancing our understanding of the middle atmosphere thermal structures and dynamics. In this study, the lidar temperature morphology is formed at Rothera (67.5ºS, 68ºW) and South Pole using the lidar observations from 1999 to 2005. Teleconnection (inter-hemispheric coupling) is one of the new mechanisms causing, e.g., the temperature variations in the southern polar middle and upper atmosphere by regions not physically attached, e.g., the northern polar stratosphere. We study it by deriving the teleconnection patterns over the global latitudes and from the stratosphere to lower thermosphere using 8-year temperature observations of SABER and 54-year temperature and wind simulations of WACCM. A main new finding is that the teleconnection extends well into the lower thermosphere, the thermospheric anomalies are consistent with the corresponding changes of the winter-to-summer lower-thermospheric branch of the residual circulation, and the winter stratosphere perturbations influence the stratosphere, mesosphere and thermosphere globally. Cold pole bias is a long-standing problem in most general circulation and chemistry climate models, referring to the simulated southern winter stratosphere is significantly colder

than observations. Our lidar measurements are used to quantify such bias in WACCM. We then propose a new inertial gravity wave (IGW) parameterization to compensate the missing wave drag in WACCM, with which the simulated temperature is increased by 20 K and the simulated zonal wind jet is decreased by 10−30 m/s in the southern winter stratosphere. Also, the polar vortex breaks earlier and the wind reversal level during spring is lower, making the WACCM simulations closer to observations. Overall this thesis work helps advance our understanding of the polar region thermal structure and how dynamics affect the temperature variations. It lays the foundation to establish the temperature benchmark for studies of climate change.

Dedication

To my parents, Lichun Tan and Ruoxin Qiu, my wife Xianjing Liu, who gave me continuous encouragements and supports.

Acknowledgements

I would like to thank my advisors, Dr. Xinzhao Chu and Dr. Han-Li Liu. I have worked with Dr. Xinzhao Chu for four years since May 2008. I greatly appreciate the tremendous time Dr. Xinzhao Chu spent discussing with me and providing me guidance on lidar observations and teleconnections. I have worked with Dr. Han-Li Liu for two years since November 2010. I'm really grateful for Dr. Han-Li Liu's ideas and guidance on teleconnection and cold pole bias.

I am thankful to Dr. Ling Wang and Dr. Chihoko Yamashita. Your questions and suggestions are so important to my research.

I would like to thank Dr. Jeffrey Thayer and Dr. Cora Randall for their questions on my comprehensive exam and thesis defense.

Thank you to my colleagues and friends Dr. Wentao Huang, Dr. Xian Lu, Zhibin Yu, Cao Chen, John Smith, Weichun Fong and Brendan Roberts for your support during my graduate study.

Finally I would like to acknowledge the National Science Foundation for providing financial support during my PhD study. I would like to acknowledge the National Center for Atmospheric Research (NCAR)/High Altitude Observatory (HAO) for providing the computing resource used in my research.

Contents

Chapter

Tables

Table

Figures

Figure

Chapter 1 Introduction

Temperature is a fundamental atmospheric parameter and is a critical factor to understand climate change [*Roble,* 1995]. Polar temperature is more sensitive to global climate change than equatorial areas which make polar temperature an excellent candidate for monitoring climate change [*IPCC report,* 2011]. Temperature dominates many atmosphere phenomena in Polar region, such as polar mesospheric and stratospheric clouds [*Thomas,* 1991; *Solomon,* 1999]. Temperature is also a critical factor in middle atmosphere chemical process such as ozone and metal species [*Solomon,* 1999; *Plane,* 2003]. Therefore temperature is one of the most important parameters to understand stratosphere and mesosphere.

However, middle atmosphere study has suffered from the lack of high-quality temperature observational data because the middle atmosphere is too high for balloons and too low for most of the satellites. Polar orbit satellites such as SABER are able to provide temperature data, but they cannot provide continual coverage of polar region because of the yaw circle problems [*Russell et al.,* 1999; *Remsberg et al.,* 2004]. Lidar is able to provide year-round, continual high–resolution and range-resolved observations in the Polar Regions and that makes lidar one of the most powerful tools in acquiring polar atmospheric temperatures [*Chu et al.,* 2003; *Chu et al.,* 2004; *Chu and Papen*, 2005]. An iron (Fe) Boltzmann temperature lidar [*Chu et al.*, 2002; *Gelbwachs,* 1994] was operated at the South Pole from December 1999 to October 2001 and at Rothera (67.5 S, 68 W) from December 2002 to March 2005 through collaboration between the British Antarctic Survey and the University of Illinois. In current study, these lidar observational data are used to form the temperature climatology in the southern polar region.

To understand temperature climatology and temperature variations in the polar region, a temperature benchmark is critical but it is not available in the current middle atmosphere community. The lidar observations in Antarctica are critical in the establishment of temperature benchmark in the southern polar region. However, even with lidar observations, it is still a very challenging task to establish temperature benchmark because temperatures are affected by many factors and the variations in the polar region are not fully understood yet, such as inter-hemispheric coupling.

Inter-hemispheric coupling (broadly referred to as teleconnection) is one important mechanism that significantly affects the temperatures in the polar region. Inter-hemispheric coupling refers to the effect that the temperatures in the southern polar region can be affected by regions not physically attached, such as the northern hemisphere. Therefore, it is necessary to understand inter-hemispheric coupling first before a meaningful temperature benchmark can be established precisely. Inter-hemispheric coupling was discovered recently by *Becker and Schmitz* [2003]. Observations have shown that inter-hemispheric coupling can affect temperature and mesospheric cloud occurrence in the summer mesosphere and lower thermosphere, which makes it a deciding factor in the study of climate change and ozone at the polar region. It is believed that inter-hemispheric coupling is caused by a series of wave–mean flow interactions, triggered by the planetary wave activity in the winter troposphere and stratosphere. So inter-hemispheric coupling contains invaluable information about waves, circulations and their interactions, which are almost impossible to observe directly. The information discussed above is very important in the study of temperature climatology and temperature variations in the southern polar region.

To study inter-hemispheric coupling, WACCM simulations and SABER observations are used. Through taking a unique approach of correlations, a zonal-mean global teleconnection

pattern with stable nearly "chess" patterns in the equatorial and northern polar region is discovered, and we also reveal that the inter-hemisphere coupling has inter- and intra-annual variations in the southern polar region. We derive the teleconnection patterns of temperature versus temperature and temperature versus residual circulation over the global latitudes and from the stratosphere to lower thermosphere using temperature data measured by the Sounding of the Atmosphere using Broadband Emission Radiometry (SABER) from 2002 to 2010, and using 54 years of simulations of temperatures and winds by the Whole Atmosphere Community Climate Model (WACCM). We also analyze the possible mechanisms of teleconnection by investigating the correlations between the temperature and residual circulation. The correlation patterns show that teleconnection exists globally over the equatorial, mid- and high-latitudes, and temperature anomalies correspond well to the anomalies of the residual circulations through adiabatic heating/cooling. A main new finding of this study is that the teleconnection extends well into the lower thermosphere, the thermospheric anomalies are consistent with the corresponding changes of the winter-to-summer lower-thermospheric branch of the residual circulation, and the winter stratosphere perturbations influence the stratosphere, mesosphere and thermosphere globally. Using a reference point chosen in the northern winter stratosphere, we find that the teleconnection structures for time periods with and without Sudden Stratospheric Warmings (SSWs) display similar patterns in SABER, and teleconnection patterns in WACCM are nearly identical for days with major SSWs, minor SSWs and without SSWs. WACCM results show strong inter-annual and intra-annual altitude variations of the teleconnection patterns in the southern polar region but stable altitudes of correlation regions in the equatorial and northern latitudes. The altitude variations are likely responsible for the weak correlations poleward of 60°S when multi-year or multi-month data are used.

Moreover, high-quality lidar temperature measurements are essential for validating and calibrating modern global circulation models. Then the models in turn facilitate the study of temperature climatology and variations in the polar region, since experiments can be carried out in the model simulations with different chemistry and dynamics settings. Simulation results from the Whole Atmosphere Community Climate Model (WACCM) are compared with the lidar temperature morphology. The bias in WACCM simulation in the polar region can be identified. The cold pole bias in WACCM, which is a long lasting problem in many models, is quantified.

The cold pole bias refers to the cold bias of polar stratosphere temperature at southern hemisphere simulated in most general circulation models (GCMs) and chemistry climate models (CCMs) during the winter and spring when compared to the observations. The cold pole bias is a long-standing problem in most models, implying the lack of wave forcing in the southern stratosphere. Lower temperatures lead to the formations of polar stratospheric clouds (PSC), which in turn increase ozone depletion. Through this, the colder temperatures lead to a false ozone depletion in these models, which is too strong and recovers too late during spring. Accompanying the cold pole bias, the jet in the stratosphere is too strong and the polar vortex breaks too late.

In current study we try to reduce the cold pole bias in WACCM through new gravity wave parameterization. Inertial gravity waves (IGWs) exist in the atmosphere globally; however, the parameterized gravity waves in WACCM are mesoscale waves without including any inertial gravity waves. Furthermore, inertial gravity waves usually break at lower altitudes than mesoscale waves according to Lindzen's theory. Therefore, inertial gravity waves are a candidate of providing the missing wave drag and additional inertial gravity waves may be able to reduce the cold pole bias in WACCM. To test this hypothesis, additional inertial gravity waves are

launched while the original mesoscale gravity waves in WACCM are kept. Using the new gravity wave parameterization, the simulated wintertime temperature is ~20 K warmer in the southern polar stratosphere while the simulated wintertime zonal wind jet is about 10 to 30 m/s slower than the originals. Also, the polar vortex in the southern hemisphere breaks earlier and the wind reversal level during spring is lower. All these changes make the WACCM simulations closer to ERA-40, suggesting that additional inertial gravity waves are able to reduce the cold pole bias.

In summary, this dissertation aims to study (1) the temperature morphology in the southern polar region observed by lidar, (2) the teleconnection patterns in SABER observations and WACCM simulations, (3) whether inertial gravity waves are able to reduce the cold pole bias in the southern polar region in WACCM simulations.

(1) Lidar observations are important in the study of climate change in the southern polar region for its high resolution and ability in providing continuous observations covering both stratosphere and mesosphere. In current study, lidar observations will be used to form the morphology in the southern polar region and compared with SABER and WACCM for the purpose of mutual validation. Moreover, by comparing with lidar observations, the cold pole bias in WACCM in the southern polar region can be quantified.

(2) Teleconnection has received considerable attention in the middle atmosphere community over the past few years. It can reveal critical information about the residual circulation and wave-flow interaction in the middle atmosphere. But it is challenging to study due to the lack of observations and insufficient latitude or altitude coverage of model simulations. In current study, we utilize WACCM simulations and SABER observations, which provide global scale coverage from less than 20 km to over 120 km, to form the global scale teleconnection patterns and study the inter- and intra-annual variations.

(3) Cold pole bias is a long lasting problem in many GCM and CCM models and it significantly affects the temperature and ozone simulation in the southern polar region. Thus it is critical to reduce this bias in simulations. In current study, we aim to provide a method to resolve this problem in WACCM simulation. We propose to use additional inertial gravity waves launched at both hemispheres above 30 degree in WACCM simulation to compensate the missing wave forcing, which is believed to be the cause of the cold pole bias. The inertial gravity waves exist physically in the atmosphere, making it a reasonable candidate to compensate the missing wave forcing. The effects of inertial gravity wave scheme will be tested in current study.

This dissertation consists of five chapters. Following the introduction, Chapter 2 displays the temperature climatology in Antarctica observed by lidar and the comparison with SABER and WACCM. Chapter 3 summarizes the teleconnection results we derived from SABER and WACCM. Chapter 4 discusses the effects of inertial gravity wave scheme in reducing the cold pole bias in WACCM simulation. Chapter 5 concludes all the results in current dissertation.

Chapter 2 Antarctic Temperature Morphology in the Stratosphere and Mesosphere Observed by Lidar and Comparison to WACCM

High-quality lidar measurements of atmospheric parameters and constituents are essential for validating and calibrating modern global circulation models. Lidar measurements of temperatures in the polar region provide a convenient means of testing model calculations. The satellites are able to provide observations at lower latitudes but it is difficult for them to provide high resolution observation in the polar region, which makes lidar observation in the southern polar region invaluable. WACCM simulations at the southern polar region are compared with temperature morphology formed by lidar to quantify the magnitude of cold pole bias. In teleconnection study, to form the teleconnection pattern, high resolution temperature observations at the polar region are essential which makes lidar temperature morphology a potential candidate in the future study of teleconnection. In current dissertation, the temperature morphology will be formed at Rothera and South Pole using Lidar observation. The Fe Boltzmann lidar that made the temperature measurements at these two Antarctic stations is currently deployed to McMurdo Station (77.83ºS, 166.67ºE) and will continue to provide observation data for several years. The morphology formed in this dissertation can be combined with the new observations in the future to produce a more complete temperature characterization in Antarctica.

2.1 Introduction

Atmospheric temperature is among the most important parameters in many polar science studies. Temperature dominates numerous geophysical phenomena, such as polar mesospheric

clouds (PMCs) and polar stratospheric clouds (PSCs) – both of which form only at extremely cold temperatures [*Thomas,* 1991; *Solomon,* 1999]. Temperature is a key variable in climate change studies [*Roble,* 1995], while important chemical processes involving MLT odd-oxygen and metal species are temperature dependent [*Solomon,* 1999; *Plane,* 2003]. Acquisition of range-resolved temperature from the stratosphere into the lower thermosphere is challenging. Although several satellite instruments are making progress, most lack absolute temperature calibration and many observations do not reach high latitudes. Thus, ground-truth temperature measurements at high southern latitudes are essential, not only for validating space-based measurements, but also as a key parameter in many polar science and climate studies. Year-round, range-resolved temperature measurements at multiple high-latitude sites are crucial for establishing the initial benchmark against which potential long-term climate changes can be compared many decades into the future.

WACCM simulations at the southern polar region are compared with temperature morphology formed by lidar to quantify the magnitude of cold pole bias. In teleconnection study, to form the teleconnection pattern, high resolution temperature observations at the polar region are essential which makes lidar temperature morphology a potential candidate in the future study teleconnection. In current dissertation, the temperature morphology will be formed at Rothera and South Pole using Lidar observation. This Fe Boltzmann lidar is currently deployed to McMurdo Station (77.83ºS, 166.67ºE) and will continue to provide observation data for several years. The morphology formed in this dissertation can be combined with the new observation in the future to produce a more complete temperature measurement at Antarctica.

2.2 Description of Lidar Observations

From November 1999 to October 2001, the University of Illinois Fe/Rayleigh lidar was

operated at Atmospheric Research Laboratory, which is located 488 meters north of the geographic South Pole [*Pan and Gardner* 2003]. From January 2003 to March 2005, the same Fe/Rayleigh lidar was operated at Rothera (67.5 S, 68.0 W), Antarctica through a collaboration between the British Antarctic Survey and the University of Illinois. The total observational time is listed in Table 2.1. Rayleigh signal is the molecular scattered lidar signal and it is proportional to atmosphere density. Relative density profile can be derived from Rayleigh signal. Then temperatures can be derived by integrating the relative density profile downward using the hydrostatic equation and a starting temperature at 65 km (seeding temperature). Temperature at 65 km from MSIS-00 is used as the seeding temperature. *Chu et al.* [2002] provided a detailed description of instrument design for this lidar and its temperature measurement capabilities.

	Jan	Feb	Mar	Apr	May	Jun	Jul	Aug	Sep	Oct	Nov	Dec	Total
Rothera (Day)	19	10	3	3	3	11	7	1	2	5	7	15	86
Rothera (Hour)	385	116	32	37	42	136	68	15	10	38	85	297	1261
South Pole (Day)	23	8	6	6	5	9	6	4	5	5	8	16	101
South Pole (Hour)	194	51	60	52	42	66	52	33	31	34	110	139	864

Table 2.1: Lidar observation statistics at Rothera and South Pole.

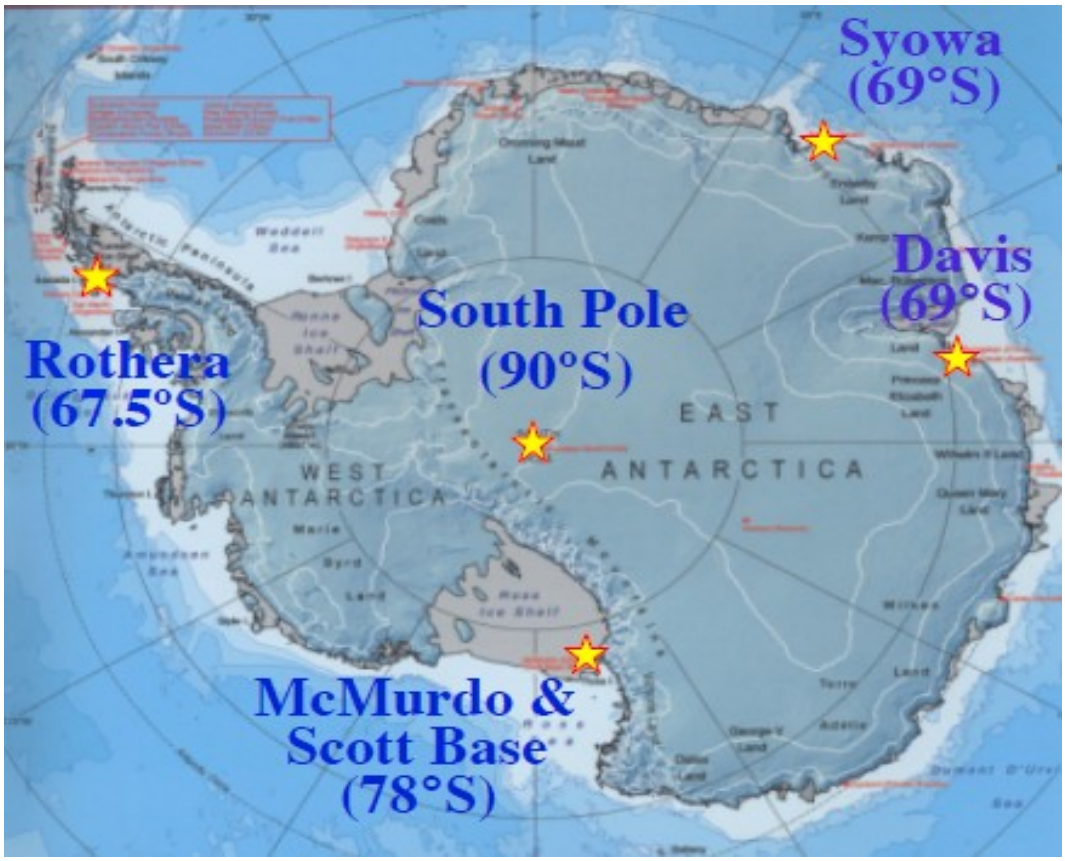

Figure 2.1: Rothera station and South Pole station in Antarctica.

2.3 Temperature Morphology Observed by lidar at Rothera and the South Pole

Rayleigh lidar technique is used to calculate daily temperature profile from the returned photo counts [*Chu et al.,* 2002; *Hauchecorne and Chanin*, 1980; *Gardner*, 1989; *Whiteway and Carswell,* 1994]. The daily temperature profile is used to form the temperature morphology at polar region using a lidar data processing method which has been used in various lidar observations such as *Pan and Gardner* [2003]. For each day in which the lidar is operated, a daily temperature profile can be calculated. These daily temperature profiles are combined together to form monthly mean temperature profiles from January to December. January at Rothera for instance, all the daily temperature profiles at Rothera in January 2003, January 2004,

and January 2005 are averaged to form the composite monthly mean temperature profile of January. The composite monthly mean temperature profiles of other months are formed using the same method for both Rothera and South Pole. To smooth the monthly mean temperature profiles, 6-order polynomial fit was used to calculate a fitted monthly mean temperature profiles. Original temperature profiles minus fitted temperature profiles are the residuals which are affected by the noise of the observed return photon counts. To reduce the effects of noise on the temperature morphology, the residuals are smoothed using a Hamming window with a full width at half maximum (FWHM) of 7.5 km. The smoothed residuals are then added back to the fitted monthly mean temperature profiles to form the monthly mean temperature profiles of each month.

The monthly mean temperature profiles from January to December at Rothera and South Pole are displayed in Figure 2.2 and Figure 2.3 respectively. The altitude range of the monthly mean temperature profiles are 25 km to 65 km and the resolution is 500 meters. Below 25 km, aerosol scattering contaminates Rayleigh signal, so the derived temperature is not trustable. Above 65 km, the signal to noise ratio is too small and the signal can be contaminated by the resonance fluorescence of Fe, the derived temperature is not trustable either. In Figure 2.2, monthly mean temperature profiles from lidar observations, SABER observations and MSIS simulations are displayed as blue line, green line and red line respectively. The error bars for the temperature from lidar observation are displayed as horizontal blue solid lines.

SABER data are plotted here for the purpose of mutual validation. SABER has the yaw cycle problem and cannot cover every month. From 2003 to 2005, SABER does not have data at Rothera during February, June and October. For the other nine months, monthly mean temperature profiles from lidar and SABER corresponds to each other well except for March. Currently, we cannot explain this temperature discrepancy in March.

MSIS-00 temperature at 65 km is used as seeding temperature in the derivation of temperature profile using Rayleigh integration technique. MSIS temperature is chosen as seeding temperature for the following reasons. MSIS simulations have temperature data at both Rothera and South Pole at 65 km which many other models do not. According to Figure 2.2, even though MSIS have large bias comparing to SABER and lidar below 45 km from April to July, MSIS agrees well with SABER data above 55 km. Moreover, the errors introduced by seeding temperature will be attenuated within one scale height.

The South Pole is very hard to observe for satellites and SABER cannot observe the South Pole at all. Thus the continual high-resolution lidar observation data is invaluable in the study of South Pole. Monthly mean temperature profiles of lidar data at South Pole are displayed in Figure 2.3 as purple lines. Monthly mean temperature profiles of Rothera are displayed in Figure 2.3 as blue line for comparison. Comparing with Rothera, temperature at South Pole above 45 km is colder than Rothera in most of the months. This can be explained by radiative cooling at the South Pole since the South Pole has less sunlight than Rothera. The temperature difference between South Pole and Rothera decrease during winter. For some altitudes, temperature at South Pole is even higher than Rothera during winter, one possible reason is that downwelling introduced by meridional circulation at the South Pole is stronger than at Rothera, and the adiabatic heating will compensate the radiative cooling more at the South Pole.

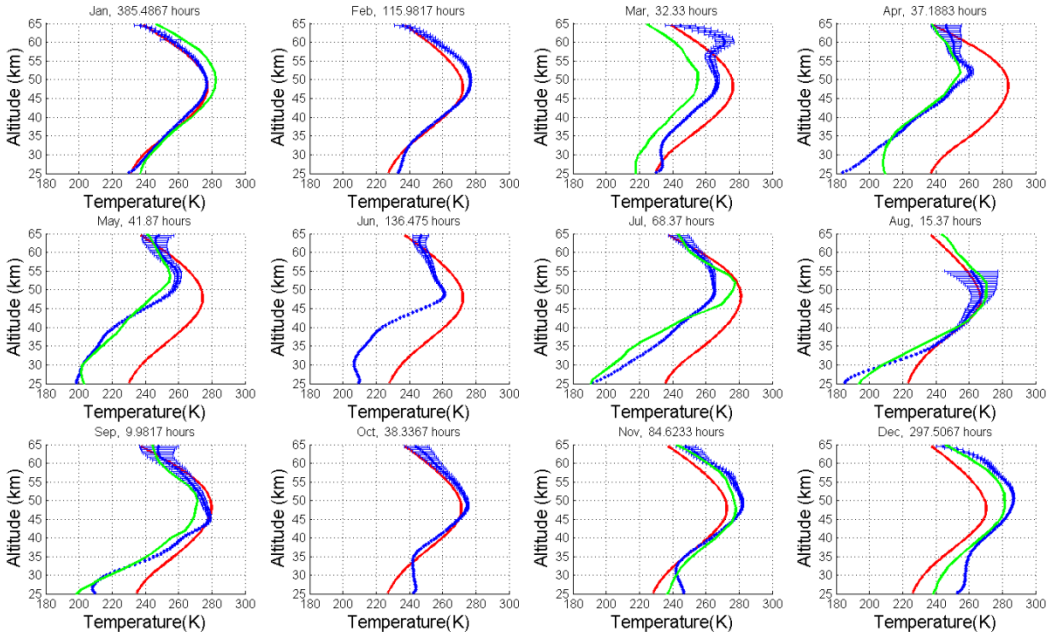

Figure 2.2: Monthly average temperature Climatology at Rothera from lidar (Solid blue), SABER (Solid green) and MSIS (Solid red)

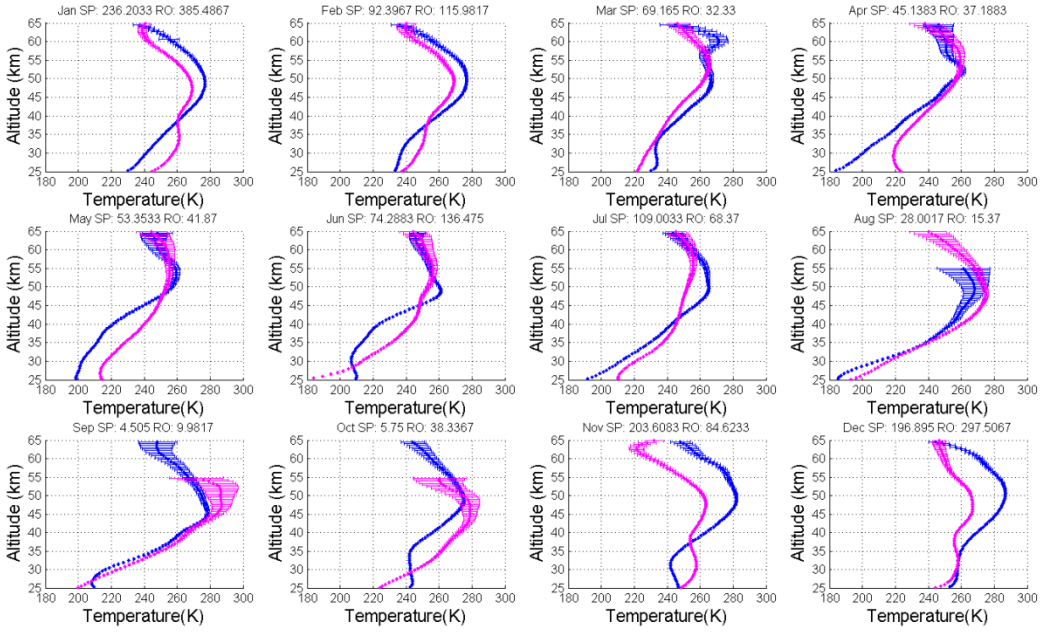

Figure 2.3: Monthly average temperature climatology at South Pole (Solid pink) and Rothera (Solid blue)

To form the temperature morphology at Rothera and the South Pole, monthly mean temperature profiles are combined to form annual temperature contour. To study the seasonal variations of temperature at polar region, at each altitude the temperature time series will be decomposed into 12-, 6-, 4-, 3-, and 2.4-month sinusoidal oscillations. These frequency components were identified to be dominant by analyzing the power spectral density (PSD) [*Pan and Gardner,* 2003]. The data processing procedure are described below. First the 12-month oscillation is derived using harmonic fit at each altitude and subtracted from the observations. Then 6-month oscillation was derived using harmonic fit at each altitude from the residuals of previous step (observations – 12-month oscillation) and subtracted from the residuals. Using the same method, 4-month oscillation, 3-month oscillation and 2.4-month oscillations are derived and subtracted one by one. After the calculation, the annual temperature contour is separated into 12-month oscillation, 6-month oscillation, 4-month oscillation, 3-month oscillation, 2.4-month oscillations along with the residuals. The residual is the leftover when all other oscillations have been subtracted from the original temperature observation signal. The amplitudes and phases of each oscillation are displayed in Figure 2.4. At each altitude, the residuals were smoothed using a Hamming window with a full width at half maximum (FWHM) of 6 weeks. The smoothed residuals and the oscillations are added together to form the temperature morphology contour of Rothera and South Pole. The temperature morphology contours of Rothera and South Pole are shown in Figure 2.5a and Figure 2.5b respectively.

According to Figure 2.4, the annual oscillation has the largest amplitude among all oscillations. Amplitude of the annual oscillation is largest at 25 km and decrease as the altitude increase. The speed of decrease is about 0.75 K per km. Semi-annual oscillation is the next largest oscillation, and the maximum amplitude located at about 37 km. But the maximum

amplitude of semi-annual oscillation is about 10 K, much smaller than the maximum amplitude of annual oscillation which is 30 K. The amplitude of semi-annual oscillation has another local maximum at about 25 km. Amplitudes of 4-month, 3-month and 2.4-month oscillations are around 2 to 3 K, very small comparing to the amplitudes of annual and semi-annual oscillations. But for these oscillations, the maximum amplitudes located at about 25 km, similar to the local maximum altitude of semi-annual oscillation. The maximum amplitude for 3-month and 2.4-month oscillations at 25 km are about 7 K while the maximum for 4-month oscillation is about 12 K.

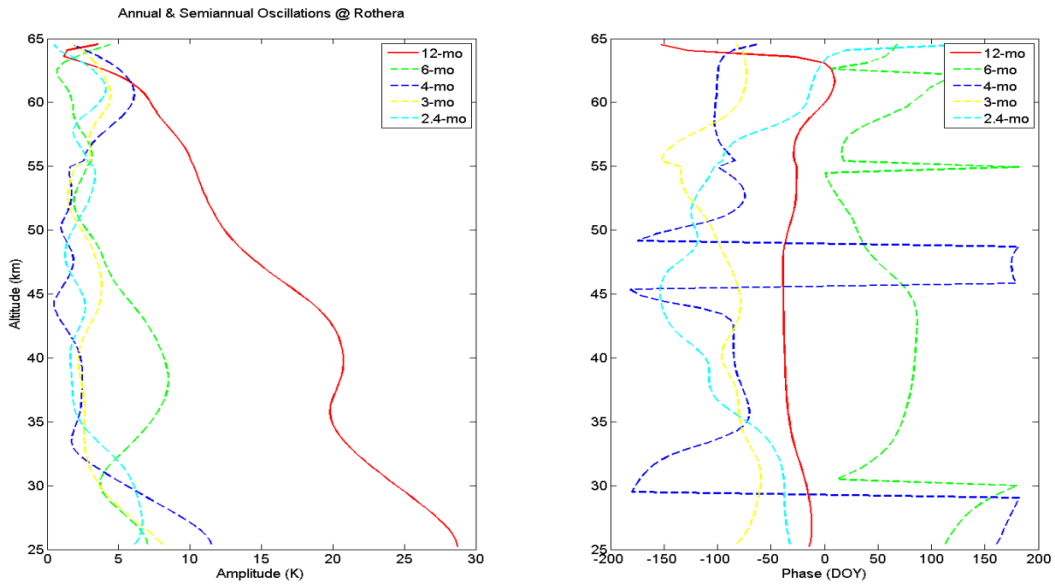

Figure 2.4: Harmonic fit of temperature climatology at Rothera. On the left is amplitude of various oscillations marked on the figure. On the right is the phase of various oscillations marked on the figure.

2.4 Comparison of Lidar Observations with SABER Observations and WACCM Simulations

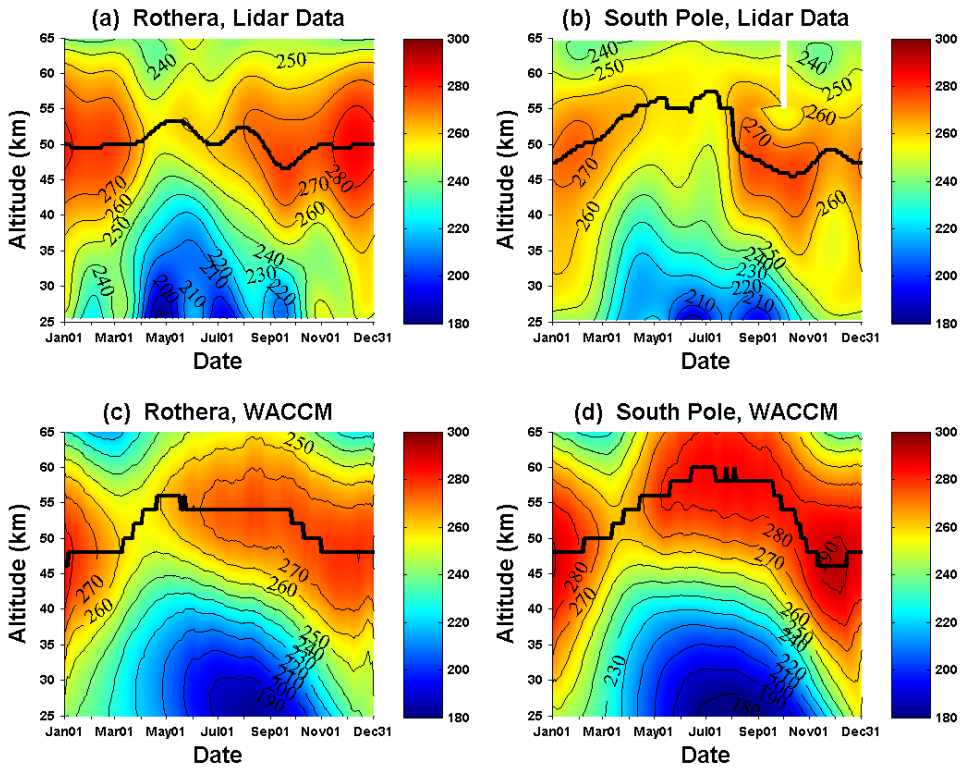

Figure 2.5: Temperature climatology at Rothera and South Pole from WACCM outputs and lidar observations. Stratopause are marked as solid black lines in each figure.

Figure 2.5a and Figure 2.5b illustrate the temperature morphology observed by lidar at Rothera and South Pole, while annual temperature contours from WACCM simulation are plotted Figure 2.5c and Figure 2.5d for comparison. The thick black lines in each subplot of Figure 2.5 denote the stratopause.

Comparing the lidar observations at Rothera and South Pole, the winter temperature below 45 km at the South Pole is colder than Rothera and the stratopause at South Pole is higher than Rothera. This can be verified by temperature morphology of WACCM simulation. The

temperature morphology from lidar observation and WACCM simulation has similar pattern and temperature magnitude though the pattern of WACCM simulation has less fluctuation than lidar observation. This is reasonable since the observations can be affected by various kinds of waves and noise while the WACCM simulation is calculated in a more idealized situation.

The temperature morphology shows asymmetry between the spring and fall. During fall the altitude range with lidar observation temperature below 250 K extends to about 48 km at both Rothera and South Pole while during spring this range can only reach about 38 km. WACCM simulations show similar patterns to lidar observations but the range below 250 K can extends to about 43 km during spring, 5 km higher than lidar observations. Moreover, the WACCM simulated temperature between 45 and 65 km from May to September are higher than lidar observed temperature while the WACCM simulated temperature below 45 km during winter are lower than lidar observed temperature.

To better display the difference between temperature morphology at Rothera and South Pole and the difference between lidar observation and WACCM simulation, the difference between lidar observation and WACCM simulation at Rothera, the difference between lidar observation and WACCM simulation at South Pole, the difference between lidar observation at Rothera and lidar observation at South Pole, the difference between WACCM simulation at Rothera and WACCM simulation at South Pole are displayed at Figure 2.6a, Figure 2.6b, Figure 2.6c and Figure 2.6d respectively.

According to Figure 2.6a−b, the temperatures from lidar observations are warmer than WACCM simulations below 45 km and colder than WACCM simulations above 45 km during the winter months. At Rothera, the lidar observed temperatures are about 20 K warmer than WACCM simulations below 45 km during winter and 10 K colder than WACCM simulations

above 45 km. This temperature difference at the South Pole becomes larger, as lidar observation is 30 K warmer below 45 km and 30 K colder above 45 km than WACCM simulations during the winter. This can be partially explained by the 'cold pole' problem of WACCM, which causes the simulated temperatures in the southern polar region to be significant colder than observations during winter. The 'cold pole' problem affects higher latitudes more and so the effects of 'cold pole' at South Pole should be larger than Rothera. This 'cold pole' problem is a long lasting problem in many models and will be discussed in more details in Chapter 4 of this thesis. During fall and spring, the temperature differences between lidar observation and WACCM simulation are much smaller than winter, and the negative and positive difference areas are small and mixed together. The shapes of the temperature contours from lidar observation and WACCM simulation are similar but not exactly the same, when the difference is calculated, this can cause the scattered pattern of positive and negative difference we observed during fall and spring. Therefore, the difference during fall and spring does not necessarily represent that the magnitudes of temperature from lidar observation and WACCM simulation are different.

Comparing the temperature difference at Rothera and South Pole which is displayed in Figure 2.6c—d , the temperature difference is very clear for WACCM simulation, possibly caused by relative stable pattern of the temperature contour. During winter, the temperature at South Pole is colder than Rothera below 50 km by less than 10 K and warmer than Rothera above 50 km by 10 to 20 K. In Figure 2.6c, this temperature difference is not clear and the pattern of temperature difference is scattered and interwound and cannot be used to reach a conclusion.

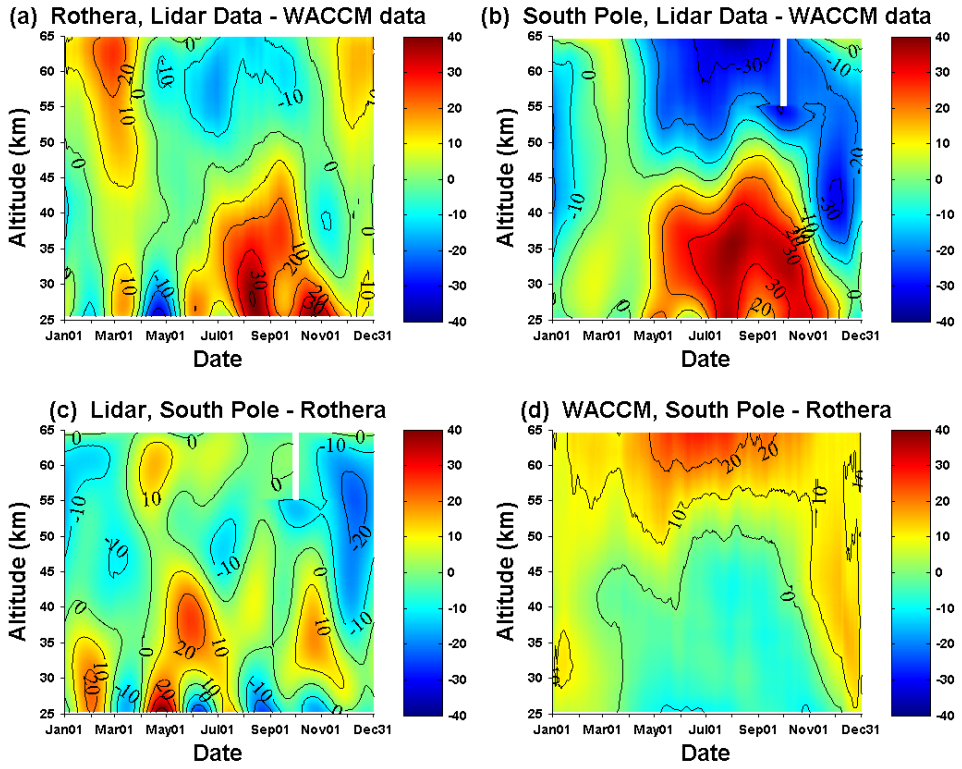

Figure 2.6: The upper two figures are temperature difference between lidar and WACCM at Rothera (upper left) and South Pole (upper right). The bottom two figures are temperature difference between South Pole and Rothera from lidar (bottom left) and WACCM (bottom right).

According to Figure 2.5, the stratopause at South Pole and Rothera is elevated during winter comparing to summer. To better study the stratopause elevation, the altitude of stratopause from lidar observation and WACCM simulation at Rothera and South Pole are compared and the results are displayed in Figure 2.7. Figure 2.7a and Figure 2.7b compare the stratopause altitude between Rothera and South Pole. Figure 2.7c and Figure 2.7d compare the stratopause altitude between lidar observation and WACCM simulation.

During winter, the stratopause at South Pole is elevated from 47 km to 57 km according to lidar observed results shown in Figure 2.7a. The elevation of stratopause at South Pole begins in March and reaches a maximum around June, then returns to about 45 km in September. At

Rothera, the lidar observed stratopause is elevated from 50 km to 53 km. The magnitude of lidar observed stratopause elevation at Rothera and South Pole are 3 km and 10 km respectively. Through the comparison between lidar observed stratopause and WACCM simulated stratopause at Rothera (Figure 2.7c) and South Pole (Figure 2.7d), WACCM simulated stratopause is always several km higher than lidar during winter. The magnitude of WACCM simulated stratopause elevations at Rothera and South Pole are about 6 km and 12 km, respectively, 2—3 km larger than lidar observed stratopause elevations. Moreover, the lidar observed stratopause elevation begins in March and ends in September, while the WACCM simulated stratopause elevation begins in March and ends in November, 2 months later than lidar observation. This later transition is possibly due to the cold pole bias in WACCM that causes the polar vortex break too late in the spring.

In both lidar observation and WACCM simulation, stratopause elevation in winter is observed and the magnitudes of stratopause elevations are similar, this verifies the existence of stratopause elevation at southern polar region during winter. However the WACCM simulated temperature morphology and lidar observed temperature morphology has discrepancies and the elevated stratopause returns to the original altitude 2 months later in WACCM comparing with lidar. These discrepancies can partially be explained by the ‘cold pole’ problem of WACCM in southern polar region which causes the too cold simulated temperature in stratosphere due to the too strong simulated residual circulation , and causes the polar vortex break too late in the spring.

While the stratopause altitude is elevated during winter, stratopause temperature will change too. Stratopause temperature from lidar observation and WACCM simulation at Rothera and South Pole are compared and the results are displayed in Figure 2.8. Figure 2.8a and Figure

2.8b compare the stratopause altitude between Rothera and South Pole. Figure 2.8c and Figure 2.8d compare the stratopause altitude between Lidar observation and WACCM simulation.

During winter, for both lidar observations and WACCM simulations, the stratopause temperature decreases during winter when the stratopause is elevated. The magnitude of decreasing is about 25 K for both lidar observations and WACCM simulations. For lidar observation, the temperature at Rothera and South Pole decrease during the winter months when the stratopause is elevated. However, in WACCM simulation, the temperature at both Rothera and South Pole decrease from March to June while the stratopause is elevated from March to November, this inconsistency cannot be explained in current study.

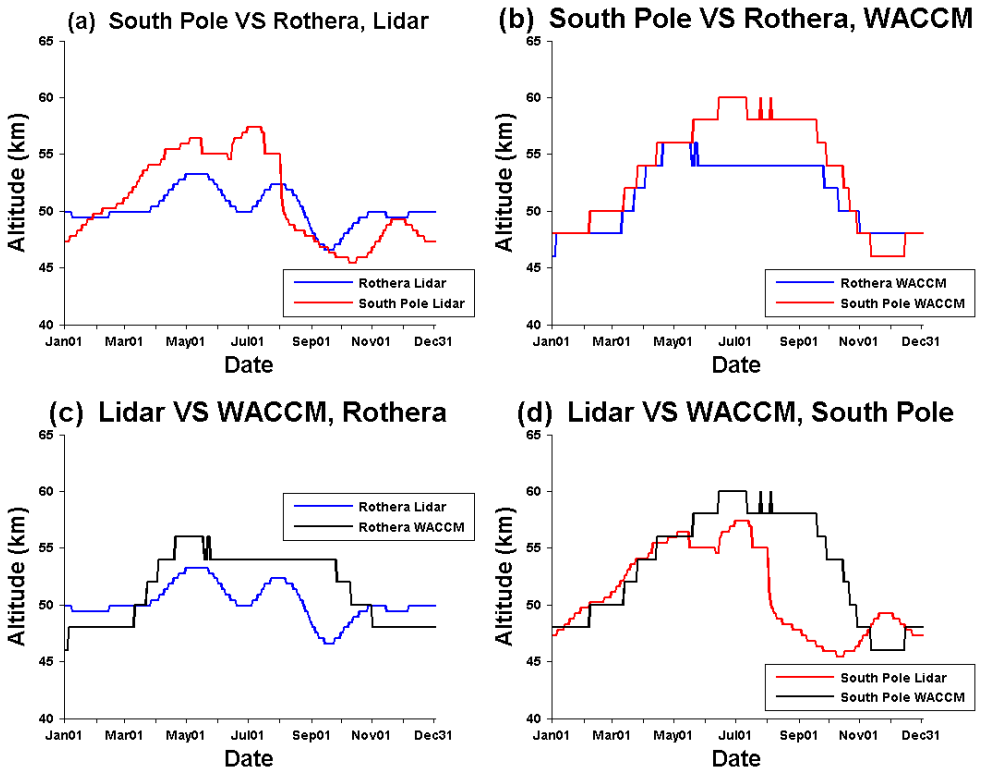

Figure 2.7: Stratopause altitudes at Rothera and South Pole from WACCM simulation or lidar observation. Stratopause altitude from lidar observation at Rothera (blue) and South Pole (red) are

displayed in (a). Stratopause altitude from WACCM simulation at Rothera (blue) and South Pole are displayed in (b). Stratopause altitude at Rothera from lidar observation (blue) and WACCM simulation (black) are displayed in (c). Stratopause altitude at South Pole from lidar observation (red) and WACCM simulation (black) are displayed in (d).

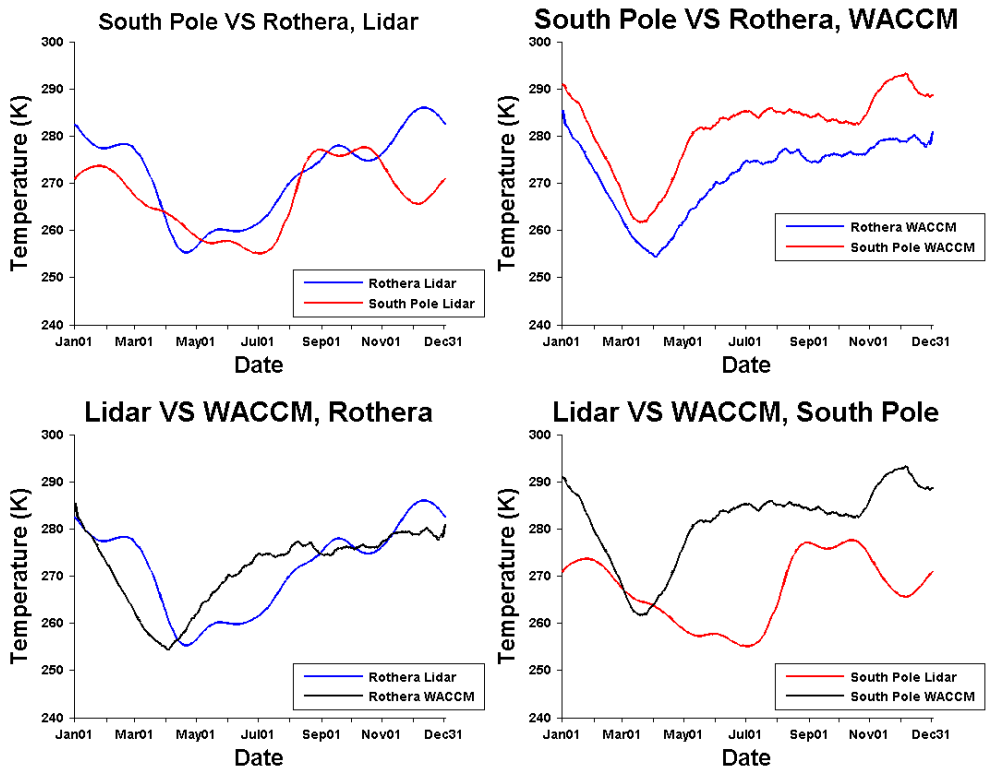

Figure 2.8: Stratopause temperature at Rothera and South Pole from WACCM outputs and lidar observations. Stratopause temperature from lidar observation at Rothera (blue) and South Pole (red) are displayed in (a). Stratopause temperature from WACCM simulation at Rothera (blue) and South Pole are displayed in (b). Stratopause temperature at Rothera from lidar observation (blue) and WACCM simulation (black) are displayed in (c). Stratopause temperature at South Pole from lidar observation (red) and WACCM simulation (black) are displayed in (d).

Lidar observations are only available at Rothera and South Pole, so stratopause elevation can only be identified at two locations in the southern polar region. To better study the stratopause elevation, stratopause elevations at more locations are necessary. Model simulations have the advantage of global scale coverage; therefore model simulations will be used to identify

the global scale stratopause elevations. WACCM simulations and ECMWF simulations will be used to identify the stratopause globally and the stratopause altitude contours are displayed in Figure 2.9 and Figure 2.10 respectively.

In WACCM, the elevated stratopause exists in both northern and southern polar region during their winter and can reach as low as 50 degree in latitude. At southern polar region, the stratopause is elevated for latitudes higher than 60°S. The magnitude of elevation at higher latitudes is larger, which corresponds to lidar observations. The largest stratopause elevation occurs at the South Pole, while Rothera (67.5 S) is located at the edge of stratopause elevation region so showing relative smaller stratopause elevation. In middle-low latitudes, no stratopause elevation is found in WACCM simulation. The stronger stratopause elevation may be explained by the dynamics. Since during winter time, there is no radiation heating and adiabatic heating/cooling from residual circulation dominates. Residual circulation, which is downwelling during winter at upper stratosphere, is strongest at South Pole. Thus, the South Pole has the largest adiabatic heating and this leads to the largest stratopause elevations [*Hitchman et al.,* 1989].

In ECMWF, the stratopause elevations are difference from WACCM simulation and lidar observations. So we conclude that maybe there is some problem with the temperature climatology of ECMWF at polar region. In ECMWF, Rayleigh friction is added above 45 km, the waves be damped and make the amplitude of waves unreality. The vertical resolution of ECMWF is not good above 50 km, the vertical resolution is 7 – 10 km above 50 km. The upper boundary of ECMWF is 80 km, the same altitude range of meridional circulation. So the meridional circulation in mesosphere may not be completely included in ECMWF. These are

some potential explanations for the unreality stratopause in ECMWF simulation, especially in the southern polar region.

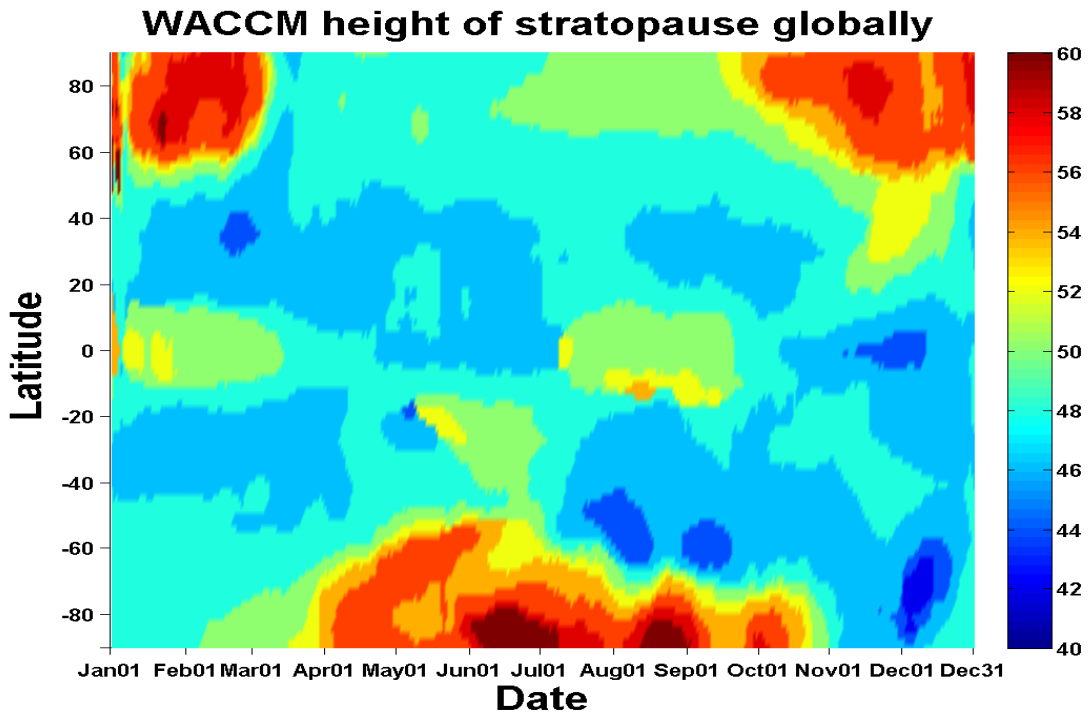

Figure 2.9: Global scale stratopause altitude seasonal variations contour from WACCM. The color represents the altitude of stratopause. The unit of color bar is km.

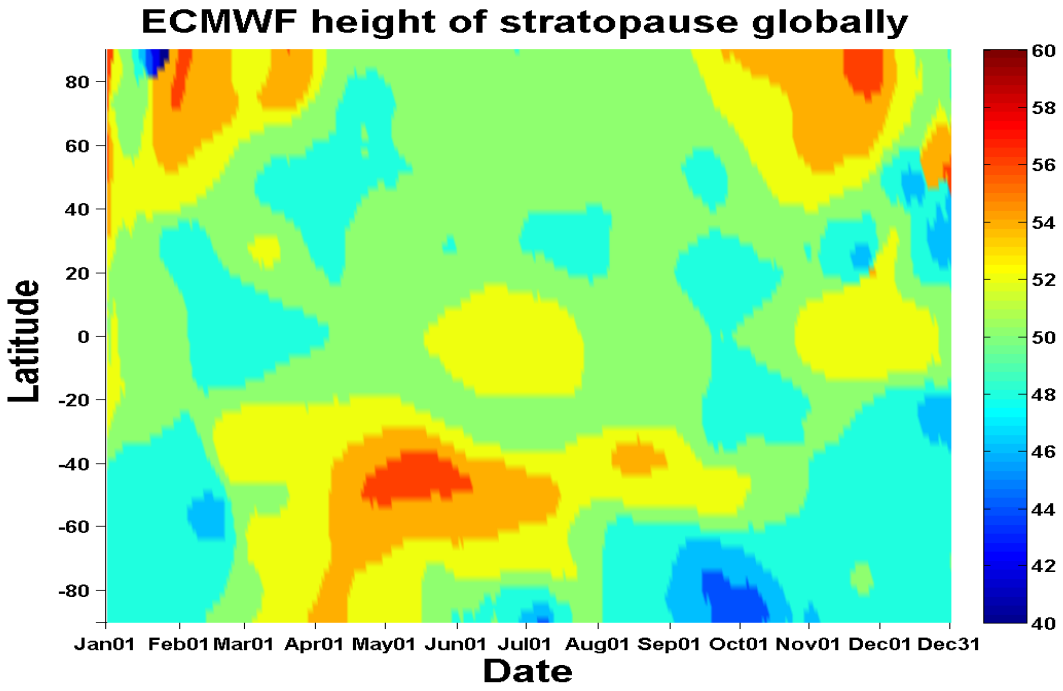

Figure 2.10: Global scale stratopause altitude seasonal variations contour from ECMWF. The color represents the altitude of stratopause. The unit of color bar is km.

2.5 Correlation Study of the Stratopause and Mesopause

From lidar observation, we observed that the stratopause altitude and stratopause temperature are anti-correlated which is displayed in Figure 2.11. The stratopause altitude at Rothera (blue) and South Pole (red) are displayed in the upper panel of Figure 2.11. The stratopause temperature at Rothera (blue) and South Pole (red) are displayed in the lower panel of Figure 2.11. Since stratopause altitude and stratopause temperature has this interesting anti-correlation, we speculate that mesopause altitude and mesopause temperature may have similar correlation.

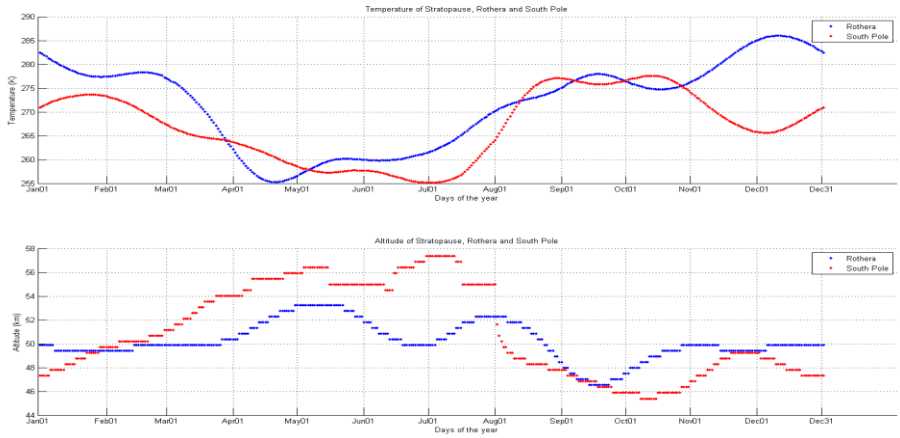

Figure 2.11: Stratopause altitude and temperature from lidar observations at Rothera

To further study the correlation of stratopause altitude, stratopause temperature, mesopause altitude and mesopause temperature, SABER observation are used because SABER has the advantage of global coverage and altitude coverage which can be used to identify both stratopause and mesopause globally. The latitude resolution we used is 4 degree. For every 4 degree in latitude and every month from 2002 to 2008, a zonal mean monthly mean temperature profiles from 15 km to about 100 km is calculated from SABER observation and this profile will be used to identify the stratopause and mesopause. From 2002 to 2008, there are totally 84 months. For each month, stratopause altitude, stratopause temperature, mesopause altitude and mesopause temperature are identified for all latitudes from 80 S to 80 N. The correlation between 84 months stratopause temperature and 84 months mesopause temperature are calculated for all latitudes from 80 S to 80 N and the results are displayed in Figure 2.12a. The correlation between mesopause altitude and stratopause altitude, mesopause temperature and stratopause altitude, mesopause altitude and stratopause temperature, mesopause altitude and mesopause temperature,

stratopause altitude and stratopause temperature are calculated using similar method and the results are displayed in Figure 2.12b—f respectively.

According to Figure 2.12a, the mesopause temperature and stratopause temperature have large negative correlations of about -0.9 at high latitudes (above 50 S or above 50 N). At equatorial region, the correlation is relative small, around 0 for most of the time and the maximum correlation is smaller than 0.5. The correlation plots between the mesopause altitude and stratopause temperature (Figure 2.12d) and between the mesopause altitude and mesopause temperature (Figure 2.12e) show similar patterns to Figure 2.12a, large absolute value of correlation at high latitude and small correlation at equatorial region. The correlation between the mesopause altitude and stratopause altitude (Figure 2.12b), between the mesopause temperature and stratopause altitude (Figure 2.12c), and between the stratopause altitude and stratopause temperature (Figure 2.12f) are small. The correlation in these three cases are smaller than 0.5 for all the latitudes and fluctuate around 0. These results show that the mesopause temperature, mesopause altitude and stratopause temperature are correlated with each other at high latitude while stratopause altitude is not correlated with any of them.

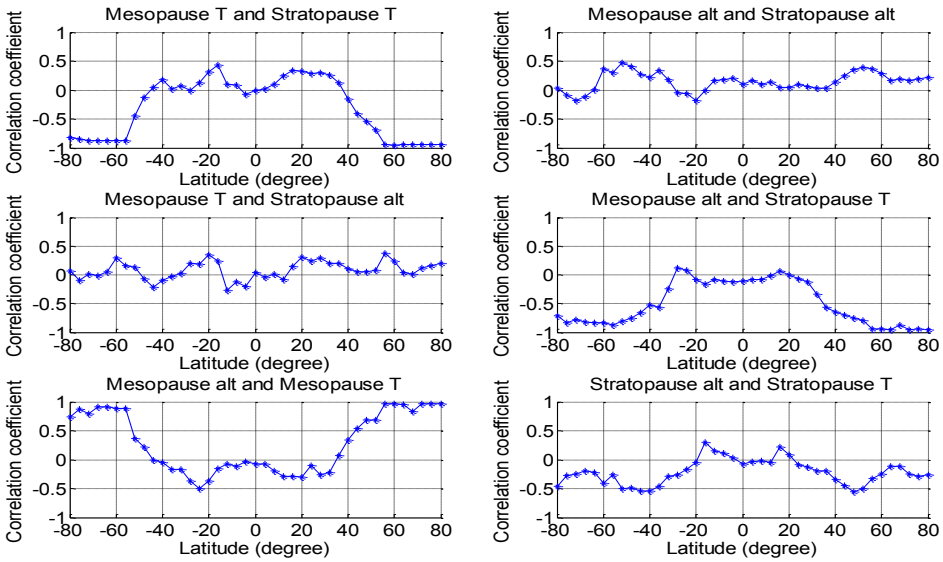

Figure 2.12: Correlation of Mesopause and Stratopause.

The seasonal variations contain annual oscillation (AO), semi-annual oscillation (SAO), quasi-biennial oscillation (QBO) and 4 month oscillation according to analysis of lidar data. Each oscillation may have different contributions to the total correlation. To analysis the correlation of each component, the lidar data processing described in section 3.3.1 will be used here to separate the 84 months time series of stratopause altitude, stratopause temperature, mesopause altitude and mesopause temperature at each latitude into AO, SAO, QBO, 4 month oscillation and residual. In Figure 2.13 a, the correlations between the AO of mesopause altitude and the AO of mesopause temperature at all latitudes are displayed. The correlation of the SAO, 4 month oscillation, QBO, residual are displayed in Figure 2.13 b—e respectively. The correlation of each component between stratopause temperature and mesopause temperature is displayed in Figure 2.14. The correlation of each component between stratopause temperature and stratopause altitude is displayed in Figure 2.15.

The annual oscillation and semi-annual oscillation dominate the total correlation. The annual oscillation is subtracted from 84 months time series of mesopause altitude and mesopause temperature and the correlation calculated using the remaining signal is displayed in Figure 2.13f. The correlation is still significant and this shows the remaining signal still have significant contributions to the total correlation. The annual oscillation and semi-annual are both subtracted from 84 months time series of mesopause altitude and mesopause temperature and the correlation calculated using the remaining signal is displayed in Figure 2.13g. The calculated correlations fluctuate around 0 and this show that the contributions from the remaining signal are not significant and the AO and SAO are main contributors to the total correlation. In Figure 2.15, between stratopause altitude and stratopause temperature, the correlation of AO and SAO show opposite correlation at most of the latitudes, these correlation cancel each other and this may be the reason the overall correlation between stratopause temperature and stratopause altitude are small. AO and SAO have opposite correlation may also explain why the correlation between stratopause altitude and mesopause altitude and between stratopoause altitude and mesopause temperature are small.

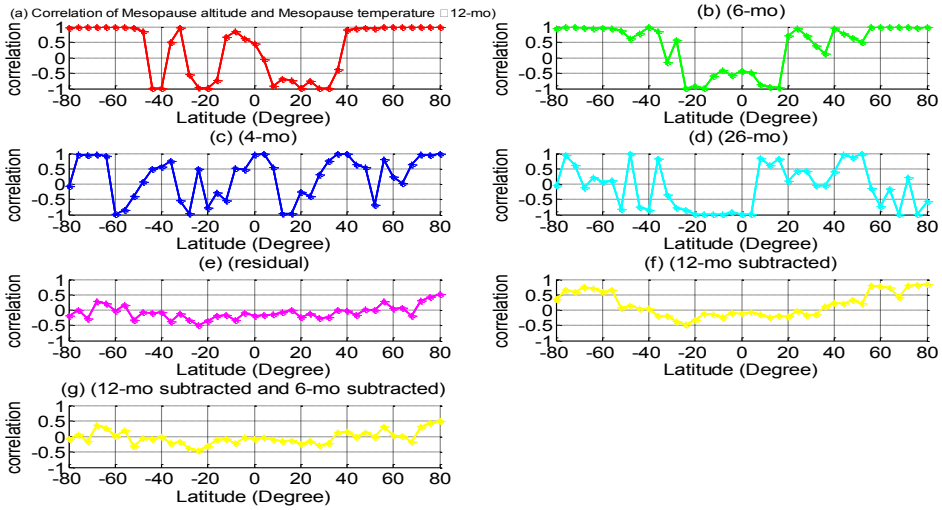

Figure 2.13: Correlation of Oscillations between Mesopause Altitude and Mesopause Temperature

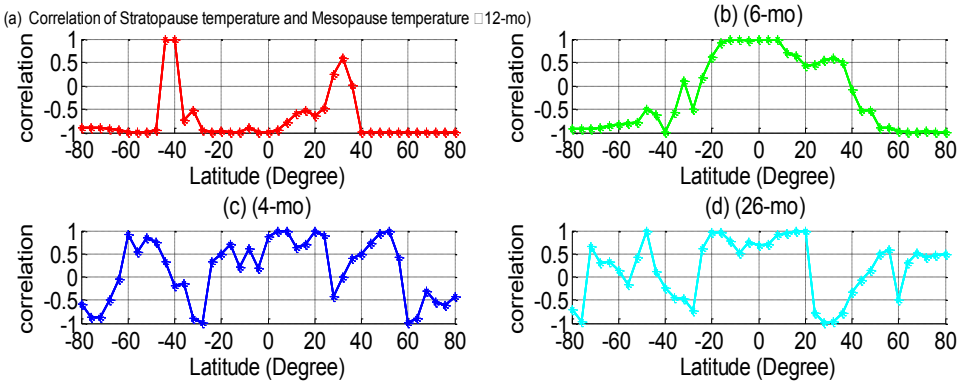

Figure 2.14: Correlation of Oscillations between Stratopause Temperature and Mesopause Temperature

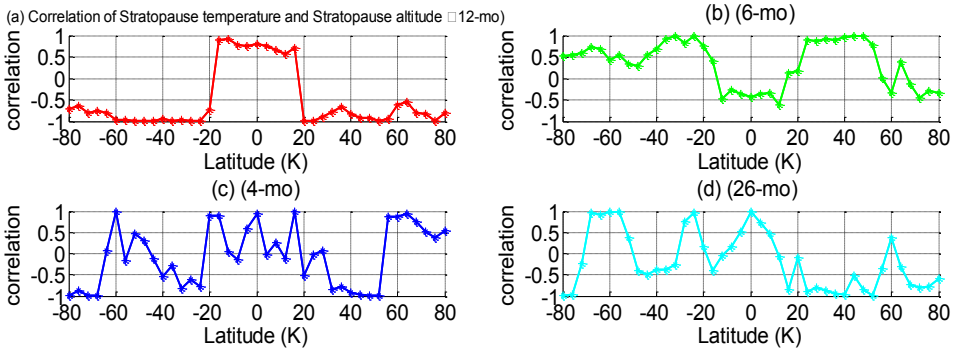

Figure 2.15: Correlation of Oscillations between Stratopause Temperature and Stratopause altitude

2.6 Conclusions

The temperature morphology at Rothera and South Pole is formed using lidar observations. Annual oscillation, semi-annual, 4-month, 3-month and 2.4-month oscillations are decomposed and analysed respectively. Temperature morphology at Rothera from lidar observation and SABER observation are compared and they show very good consistency. SABER does not have data at South Pole so the comparison is only at Rothera.

Through the comparison of lidar observation between winter and summer at both Rothera and South Pole, we observed that the stratopause is elevated during winter. The magnitude of elevation is about 10 K at South Pole and 4 K at Rothera. WACCM simulation is used to verify the existence of elevated stratopause and the magnitudes of stratopause elevation from WACCM simulation are similar to lidar observations. Even though WACCM suffers from cold pole bias during winter, the temperature morphology from WACCM simulation is consistent with lidar observations.

The stratopause temperature and stratopause altitude identified using lidar observation show significant anti-correlation and this inspires us to further study the relationship between the stratopause altitude and stratopause temperature, together with the mesopause altitude and mesopause temperature. SABER data is used in this study because SABER has global coverage from 80 S to 80 N and enough altitude coverage for the definition of both stratopause and mesopause. According to the stratopause and mesopause identified using SABER observation, the stratopause temperature, mesopause temperature and mesopause altitude have significant correlation with each other at high latitude (higher than 50 S or higher than 50 N), the correlations at equatorial region are small and fluctuate around 0. But the stratopause altitude

does not show large correlation with the stratopause temperature, mesopause temperature and mesopause altitude; all the correlations are smaller than 0.5 and most of them fluctuate around 0.

The study in this thesis provides essential ground-truth temperature measurements at high southern latitudes, which is not only critical for validating space-based measurements but also a key parameter in many polar science and climate studies. The temperature variations in the polar region need to be understood to establish a stable temperature benchmark. Temperatures have inter-, intra- annual variations and long term trends. Temperatures in the polar region are also affected by many factors such as teleconnections and gravity wave breakings. Currently the lidar observations are not enough to reveal all the temperature variations. For both Rothera and the South Pole, the lidar observations are only available for about 2 to 3 years, these data are not enough to clearly show inter-annual variations. At least one solar cycle lidar observations are needed in the future to provide more invaluable temperature measurements in establishing the temperature benchmark. The year-round, range-resolved temperature morphology such as the one formed in this thesis are crucial for establishing the initial benchmark against which potential long-term climate changes can be compared many decades into the future.

Chapter 3 Zonal-Mean Global Teleconnection from 15 to 110 km Derived from SABER and WACCM

In establishing the initial temperature benchmark in the polar middle atmosphere against which potential long-term climate changes can be compared many decades into the future, a major challenge is to understand the temperature variations on various scales and the mechanisms responsible for these variations. In this chapter we study teleconnection, an important mechanism in the polar region that causes significant temperature variations, through deriving the correlation patterns globally. Teleconnection refers to the effect that the temperatures in the southern polar middle and upper atmosphere can be influenced by regions not physically attached, such as the northern polar stratosphere. We derive the correlation patterns of temperature versus temperature and temperature versus residual circulation over the global latitudes and from the stratosphere to lower thermosphere (broadly referred to as teleconnection) using temperature data measured by the Sounding of the Atmosphere using Broadband Emission Radiometry (SABER) from 2002 to 2010, and using 54 years of simulations of temperatures and winds by the Whole Atmosphere Community Climate Model (WACCM). We also analyze the possible mechanisms of teleconnection by investigating the correlations between the temperature and residual circulation. The correlation patterns show that teleconnection exists globally over the equatorial, mid- and high-latitudes, and temperature anomalies correspond well to the anomalies of the residual circulations through adiabatic heating/cooling. A main new finding of this study is that the teleconnection extends well into the lower thermosphere, the thermospheric anomalies are consistent with the corresponding changes

of the winter-to-summer lower-thermospheric branch of the residual circulation, and the winter stratosphere perturbations influence the thermosphere globally. Using a reference point chosen in the northern winter stratosphere, we find that the teleconnection structures for time periods with and without Sudden Stratospheric Warmings (SSWs) display similar patterns in SABER, and teleconnection patterns in WACCM are nearly identical for days with major SSWs, minor SSWs and without SSWs. WACCM results show strong inter-annual and intra-annual altitude variations of the teleconnection patterns in the southern polar region but stable altitudes of correlation regions in the equatorial and northern latitudes. The altitude variations are likely responsible for the weak correlations poleward of 60°S when multi-year or multi-month data are used.

3.1 Introduction

Coupling of the atmosphere over altitudes and latitudes is important to understand the impacts of the lower atmosphere on the middle and upper atmosphere. Inter-hemispheric coupling between the northern winter polar stratosphere and southern summer polar mesosphere was first noted by *Becker and Schmitz* [2003]. In their paper, a general circulation model was used to study how the winter mesosphere responds to a planetary wave anomaly in the winter troposphere and lower stratosphere. Heating in the summer mesosphere and lower thermosphere (MLT) at all latitudes south of 60°N and cooling in the winter mesosphere north of 30°N are produced along with warming of the winter stratosphere during periods when planetary wave activity is increased. Adiabatic heating and direct heating caused by breaking of internal gravity waves are believed to contribute to the temperature change in the mesosphere. It is found from this modeling study that below 0.01 hPa adiabatic heating dominates, while at higher altitudes and between 30°N and 60°N, the direct gravity wave heating overcompensates for the changes in

dynamic heating [*Becker and Schmitz*, 2003]. However, the mechanism of inter-hemispheric coupling was not clearly identified in this paper. *Becker et al.* [2004] and *Becker and Fritts* [2006] used a general circulation model to reproduce the temperature and wind anomalies observed by rocket measurements in the northern summer mesosphere at Andoya in 2002. They provide model and experimental evidence showing that those anomalies are linked to enhanced planetary Rossby-wave activity in the austral winter troposphere during June–August through inter-hemispheric coupling. *Karlsson et al.* [2009a] used a comprehensive middle atmosphere model, the Canadian Middle Atmosphere Model (CMAM), to reproduce inter-hemispheric coupling and to identify possible mechanisms. They argue that the mechanism behind inter-hemispheric coupling is a series of wave-mean flow interactions, triggered by the planetary wave activity in the winter troposphere and stratosphere. The anomaly of planetary-wave forcing in the winter stratosphere produces an anomaly of zonal wind and induces a gravity wave drag (GWD) anomaly in the winter mesosphere through the change of filtering conditions. This GWD anomaly will in turn lead to an anomaly of the mesospheric pole-to-pole circulation. The anomaly of this circulation causes a heating or cooling anomaly in the equatorial mesosphere and this heating or cooling anomaly produces a thermal unbalance in the summer hemisphere. To reach balance again, the zonal wind in the summer polar region will be modified such that the filtering of mesospheric gravity waves is changed, which will affect the temperature in the summer mesosphere. *Körnich and Becker* [2010] confirmed the mechanism of inter-hemispheric coupling using a zonally symmetric model that excluded any additional effects due to resolved waves and non-zonally propagating gravity waves. They have pointed out that gravity waves in the summer hemisphere at latitudes higher than 30 deg are essential for inter-hemispheric coupling while gravity waves around the equator are not.

Karlsson et al. [2007], *Karlsson et al.* [2009b], *Xu et al.* [2009], *Gumbel and Karlsson* [2011] and *Espy et al.* [2011] provide observational evidence of inter-hemispheric coupling. *Karlsson et al.* [2007] found anti-correlations between the effective optical radius of polar mesospheric clouds (PMCs) in the summer hemisphere and temperature given by the European Centre for Medium-Range Weather Forecasts (ECMWF) in the winter stratosphere. The PMC effective radius and ECMWF temperature they used were monthly averages in July or January from 2002 to 2007. *Karlsson et al.* [2009b] used daily PMC frequencies from the Aeronomy of Ice in the Mesosphere (AIM) satellite during the Southern Hemisphere (SH) 2007-2008 summer, daily zonal-mean temperature profiles from the Microwave Limb Sounder (MLS), and zonal mean winds from the Goddard Earth Observing System (GEOS-5) in the Northern Hemisphere (NH) to study inter-hemispheric coupling. They found positive/negative correlations between SH PMC frequency and NH stratospheric zonal wind/temperature. The results indicate that intra-seasonal PMC variability is, in large measure, caused by inter-hemispheric coupling [*Karlsson et al.,* 2009b]. *Xu et al.* [2009] formed the correlation patterns of 4 independent years using MLS temperature data, where the correlations are taken between the southern summer mesosphere temperature at 0.002 hPa from 80° to 85°S and the temperatures elsewhere. This is similar to the methods used by *Karlsson et al*. [2009a], although the extent of the MLS datasets was still insufficient to fully reveal inter-annual variations of teleconnection patterns. Utilizing 9 years of Odin satellite observations of PMC occurrence frequency to represent the state of the summer mesosphere and ECMWF temperature and wind to represent stratosphere conditions, *Gumbel and Karlsson* [2011] showed the seasonal behavior of the summer mesosphere being affected by both intra- and inter-hemispheric coupling processes. *Espy et al.* [2011] confirmed the inter-hemispheric coupling between the polar summer mesosphere and planetary-wave

activity in the extra-tropical winter stratosphere using a 10-year time series of summer mesospheric temperatures near 60°N derived from OH nightglow. Their time-lagged correlation between the OH temperatures and the ECMWF winter stratospheric temperatures displayed a strong Quasi-Biennial Oscillation (QBO).

In the chapter 3 of this dissertation, we further study the correlation patterns over latitudes and from the stratosphere to the lower thermosphere (herein referred to as teleconnection) using SABER temperature data and WACCM simulations of temperatures and winds. We also analyze the possible mechanisms of teleconnection by investigating the correlations between the residual circulation and temperature. A new finding of this study is that the teleconnection extends well into the lower thermosphere, and the thermospheric anomalies are consistent with the corresponding changes of the winter-to-summer lower-thermospheric branch of the residual circulation. We examine the teleconnection for periods with and without SSWs using a reference point chosen in the northern winter stratosphere (instead of southern summer mesosphere in previous studies) in order to be consistent with the definition of a SSW. Furthermore, the 54 years of WACCM simulation results are used to calculate annual and monthly correlation patterns and analyze the inter-annual and intra-annual variations of each response region.

3.2 Data and Simulations

The SABER instrument, aboard the Thermosphere, Ionosphere, Mesosphere, Energetics, and Dynamics (TIMED) satellite, measures infrared radiance coming from the Earth's limb in the 4.3 μm and 15 μm CO2 bands to retrieve temperatures over the 15 – 110 km altitude range with 2 km vertical resolution. The orbital plane of the TIMED satellite precesses slowly because

of its 74 deg orbital inclination. It takes 60 days for SABER to cover all local times [*Russell et al.*, 1999; *Remsberg et al*., 2004]. The data are sampled at different longitudes due to the rotation of the Earth relative to the orbital plane and at different latitudes due to the motion of the satellite along the orbit. SABER began its observations in January 2002. We use temperature data from 2002 to 2010 (version 1.07), and calculate zonal mean temperature for each day. For our purpose of examining the teleconnection with and without SSW, four northern winter months (November through February) are desired for this study. However, because of the TIMED 60-day yaw cycle, SABER only covers the high northern latitudes in winter from mid January to mid March. Consequently, the data used in this study include the ~60-day period from mid January to mid March for each year.

The NCAR WACCM model extends from the ground to 140 km [*Garcia et al.*, 2007]. In this study, we use daily-mean temperature and wind profiles at each longitude and latitude calculated using a free running simulation of WACCM 3.5 for the period of 1953 to 2006. In WACCM 3.5, there are 66 pressure levels from 1000 hPa to 1×10-5 hPa and the model altitude intervals change with altitude. The intervals are ~1 and 3 km at 20 and 100 km, respectively. WACCM 3.5 employs a new scheme of gravity wave parameterization as described in *Richter et al*. [2008, 2010]. According to *Richter et al.* [2010], WACCM3.5 does not produce a QBO internally. QBO is imposed by nudging the tropical wind to observations based on *Balachandran and Rind* [1995]. At each latitude, zonal mean temperature is calculated at each pressure surface. Residual circulation is calculated using the following equation (Equations (3.5.1) of *Andrews et al.,* [1987]):

$$V = \bar{v} - \rho_o^{-1}\left(\frac{\rho_o \overline{v'\theta'}}{\bar{\theta}_z}\right)_z \qquad \text{and} \qquad W = \bar{w} + (a\cos\phi)^{-1}\left(\cos\phi \frac{\overline{v'\theta'}}{\bar{\theta}_z}\right)_\phi$$

where V and W are the meridional and vertical components of the residual circulation; $\bar{v}$ and $\bar{w}$ are the zonal mean meridional and vertical wind velocities; $\overline{v'\theta'}$ is eddy heat flux, ϕ is latitude, v' is the perturbation of the residual circulation, a is the mean radius of the Earth, and ρ_o is atmosphere density at the height of interest. Note that the z in above equation is a log-pressure height, and a scale height of 7 km is used to convert the WACCM output pressure to the log-pressure height z. As mentioned above, to examine the correlations for different SSW periods, the four northern winter months (November through February) are desired for this study. Further considering the analysis for time lags of -10 to +10 days, extra 10 days in October and in March respectively are included to ensure that the lag analysis has all four months of winter covered. Therefore, the simulation data used in this study are from October 20 to March 10 for each year. Note that tidal aliasing may be present in the derived zonal-mean temperature of SABER, but such aliasing has been removed in WACCM zonal means. Since the correlation patterns of SABER and WACCM are similar in general as shown in Section 3, it is most likely that tides are not a dominant factor in the correlation.

3.3 Teleconnection Analysis

Zonal means derived from SABER data (from mid January to mid March) are used to study teleconnection. At each latitude and altitude (with resolutions of 4 deg and 2 km), the long-term average of daily zonal-mean temperature for each day-of-year (DOY) is obtained by taking the average of the 9 years of SABER data on the same DOY. The temperature anomalies at each latitude and altitude for all 9 years are then calculated as the deviations from the long-term average of daily mean temperatures at that latitude and altitude. These anomalies are used to calculate the correlations between a chosen reference point (10 hPa, 76°N) and all other

latitudes and altitudes. All the SABER data during northern winters are separated into two categories: category 1 contains all the episodes with SSW events (both major and minor SSWs), and category 2 contains all the days without SSWs. Here a SSW event is identified using the National Center for Environmental Prediction (NCEP) temperatures at (10 hPa, 80°N). An event with the NCEP temperature increasing more than 25 K within three weeks is defined as a SSW, and all days within this temperature peak are taken as the days of this SSW. For each latitude and altitude, the temperature series in category 1 contains the SABER temperature anomalies on all days during SSWs, and all 9 years of temperature data in category 1 are combined into one array. All 9 years of temperature anomalies in category 2 are combined into one array using the same methods. The major and minor SSWs were included in the same category because there are not enough data to calculate the correlations for major and minor SSWs separately. Figure 3.1 shows the correlation patterns calculated from SABER data for days with and without SSWs, respectively. The white contour lines in Figure 3.1 indicate the 95% level of significance. In general, the regions with larger correlation magnitudes have significant levels above 95%, while the smaller correlation regions (close to zero) with colors close to green are insignificant. Both cases show very similar correlation patterns for the regions with significant levels above 95%, but the correlation magnitudes are different. The absolute values of correlation coefficients for days with SSWs are larger than for those without SSWs. This is expected because temperature anomalies are most significant during SSWs. Due to the 60-day yaw cycle of the TIMED spacecraft, SABER cannot cover the high latitudes in both hemispheres simultaneously, so no correlation is calculated poleward of 50°S in Figure 3.1.

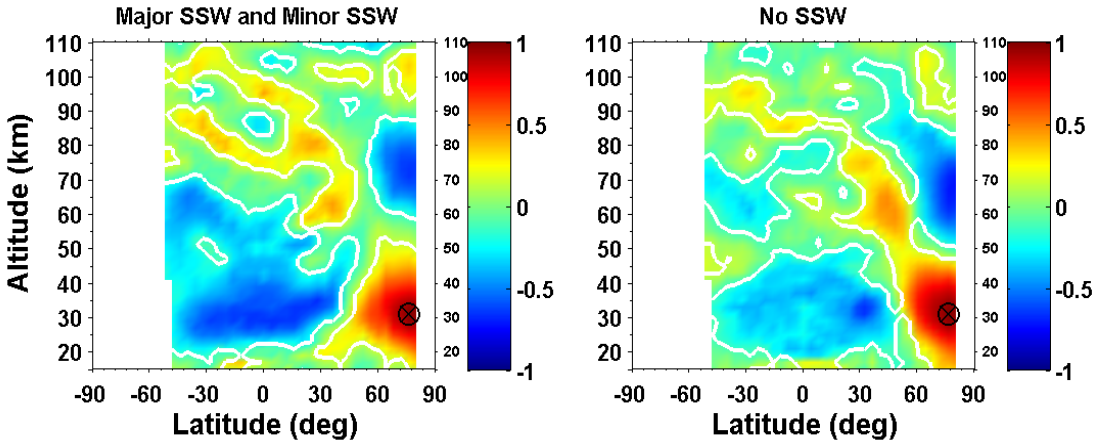

Figure 3.1: Correlation patterns between the temperature anomalies of SABER temperature series at a reference point (10 hPa, 76°N) and at all other latitudes and altitudes for days with SSWs (left) and without SSWs (right). The circle with an "X" is the reference point used for the correlation calculations. White solid lines denote the 95% significance level.

WACCM 3.5 simulation outputs during northern winter (from October 20 to March 10) are employed to reproduce the temperature correlation patterns and extend them to the global range from -90° to +90° in latitudes. The temperature anomalies of WACCM data from 1953 to 2006 are derived as the deviations from a long-term average for a given day at each latitude and altitude in a similar way as SABER, where the long-term average at that latitude and altitude is the mean over the 54 years of WACCM temperatures. The correlations of temperature anomalies are between a reference point at (10 hPa, 80°N) and all other latitudes and altitudes. The temperature correlation patterns for days with major SSWs, with minor SSWs and without SSWs are plotted in Figure 3.2a–c. Here SSW events are identified using WACCM temperatures at the reference point. Temperature increases exceeding 25 K within three weeks are defined as SSWs, while the wind reversal at 10 hPa and 60°N is used to separate major and minor SSWs according to the World Meteorological Organization's definition. The daily averaged profiles of WACCM

are used and four measurements are provided everyday (every 6 hours) in WACCM simulation, so the tides are smoothed out and won't be considered in this study.

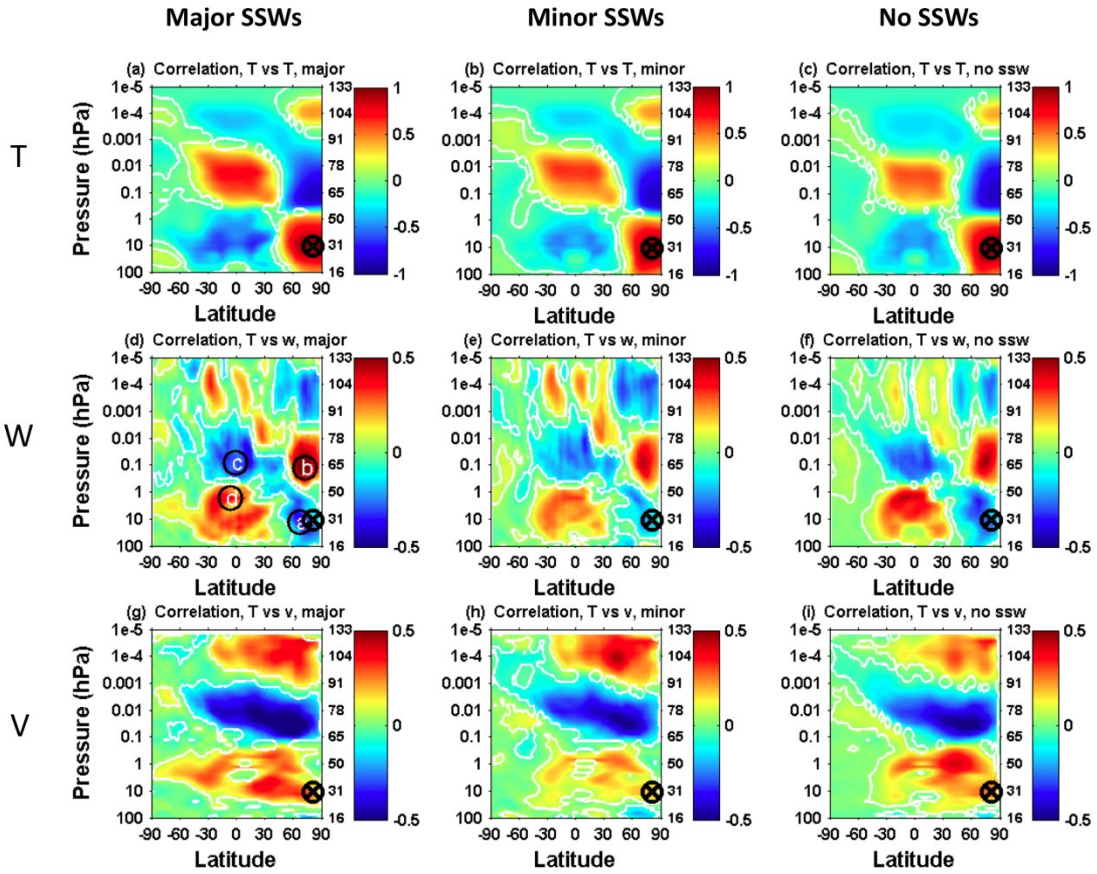

Figure 3.2: Correlation patterns between the WACCM (Oct 20 – Mar 10) temperature anomalies at the reference point (10 hPa, 80°N) and anomalies of temperature T (first row), vertical wind W (second row) and meridional wind V (third row) associated with the residual circulations at all latitudes and altitudes for days with major SSWs (left column), minor SSWs (middle column) and without SSWs (right column). The correlation scale for T is -1 to 1 and the correlation scales for W and V are -0.5 to 0.5. The symbol "X" is the reference point used for the correlation calculations. White solid lines denote the 95% significance level.

Comparing the temperature correlation results between WACCM and SABER, both show very similar patterns at high northern latitudes with positive correlation regions from 20 to 50 km,

negative correlation regions from 55 to 90 km and positive correlation regions from 90 to 110 km. In the equatorial areas, both SABER and WACCM show a negative correlation region from 20 to 50 km and a positive correlation region from 50 to 90 km. Although this equatorial positive region in SABER has more structures than the result in WACCM, the correlations are significant as indicated by the 95% significant levels. A negative correlation region is also observed in the lower thermosphere from 90 to 110 km above the equator in WACCM, while in SABER this negative correlation is observed but the boundary of the region is not well defined. Such complicated correlation patterns of SABER from 70 to 110 km in the equatorial areas are likely due to the tidal aliasing effect as indicated by the alternated positive and negative correlations from 70 to 110 km. The observed temperature anomalies may contain components of tides and this may contaminate the correlation calculated. On the other hand, since the tides have been removed from the WACCM zonal means, the WACCM simulations give a very clear pattern of negative correlations in the lower thermosphere above the equatorial regions. As for the high northern latitudes, because the tidal amplitudes are generally smaller than in the equatorial regions, the aliasing effect is likely small enough so that SABER shows the clear positive correlation in the lower thermosphere from 90 to 110 km, which is very similar to the WACCM results. Overall the comparison demonstrates that WACCM resembles the SABER temperature correlation patterns quite well, confirming that WACCM resolves the underlying mechanisms of teleconnection.

Besides the temperature correlations, the WACCM outputs are also used to derive the correlation patterns between the temperature anomalies at the reference point and the meridional (V) and vertical (W) components of the WACCM residual circulation anomalies (Figure 3.2d–i). The circulation anomalies are derived in the same manner as the temperature anomalies. Here

northward and upward directions are defined as positive for V and W, respectively. The correlation patterns of W in Figure 3.2d–f correspond to the correlation patterns of temperature in Figure 3.2a–c very well but with opposite signs and smaller magnitudes for the correlation coefficients. Note the change of the correlation scales in Figure 3.2d-i. Such a correspondence is very clear for the three correlation regions at high northern latitudes and two regions in the equatorial stratosphere and mesosphere. The correlations of W vs. T in the equatorial lower thermosphere exhibit more structures than those of T vs. T, but in general have an opposite sign. Although the correlation magnitudes are small in the southern polar region, for the correlation regions with significance levels above 95%, the W vs. T patterns still correspond with the T vs. T patterns in opposite signs. To demonstrate the meanings of these correlations, we take the case of positive temperature anomaly as an example. When the temperature at the reference point increases, the positive (negative) temperature correlation represents the regions of heating (cooling). The corresponding negative (positive) correlation regions in the vertical wind patterns indicate the enhanced (reduced) downwelling or reduced (enhanced) upwelling. In the meantime, the positive (negative) correlations in the meridional wind patterns shown in Figure 3.2g–i imply either the enhanced (reduced) northward wind or the reduced (enhanced) southward wind. The good correspondence between the W vs. T patterns and the T vs. T patterns confirms that adiabatic heating (cooling) controls the temperature anomalies.

3.4 Circulation Changes in the Stratosphere, Mesosphere and Lower Thermosphere

The correlations of V vs. T (Figure 3.2g–i) exhibit three cell patterns from the stratosphere to the lower thermosphere. They reflect the changes of the residual circulations (Figure 3.3) that will be discussed in this section. The negative and positive correlation regions

in the stratosphere as displayed in Figure 3.2a–c are induced by the anomalies of the Brewer-Dobson circulation [*Körnich and Becker,* 2010]. The increase of planetary wave forcing in the northern stratosphere induces a stronger poleward Brewer-Dobson circulation [*Holton,* 1992; *Yulaeva et al.,* 1994], which is displayed as the positive response regions below 60 km in the correlation patterns of meridional wind in Figure 3.2g–i. The stronger poleward circulation leads to an increase of downwelling (upwelling) in the northern polar (equatorial) stratosphere region, which is shown as negative (positive) correlations in Figure 3.2d–f. Such increased downwelling (upwelling) results in enhanced adiabatic heating (cooling) in the polar (equatorial) stratosphere. The consequences are positive (negative) temperature correlations below 60 km in the corresponding regions as shown in Figure 3.2a–c.

Mesosphere correlation patterns in Figure 3.2a–c are mainly induced by the anomalies of the summer-to-winter pole flow in the mesosphere. The increase of westward planetary-wave driving in the northern stratosphere decelerates the eastward wind in the winter stratosphere which in turn changes the filtering of gravity waves. Consequently, westward gravity wave forcing is reduced and thus the mesosphere summer-to-winter pole circulation is weakened [*Karlsson et al.,* 2009b; *Körnich and Becker,* 2010]. The decrease of this circulation is evident in the negative correlation of the meridional wind in Figure 3.2g–i. The weakened circulation leads to weaker downwelling thus reduced adiabatic heating in the northern polar mesosphere, resulting in the negative temperature correlation from 55 to 90 km in Figure 3.2a–c and positive vertical wind correlation in Figure 3.2d–f in the same height range. In the equatorial mesosphere, the increasing temperature corresponds to the enhanced adiabatic heating or reduced adiabatic cooling associated with the negative anomalies of vertical wind according to Figure 3.2d–f. Vertical wind anomalies in the equatorial mesosphere are manifested either as an increase of

downwelling or a decrease of upwelling, but whether or not these anomalies of downwelling or upwelling are caused by the meridional mesospheric circulation anomalies deserves further study in the future. Figure 3.2g–i show that the negative correlation regions of the meridional circulation in the mesosphere extend from the northern polar region to ~50°S, suggesting that the mesosphere response to the winter stratosphere anomalies is a global effect.

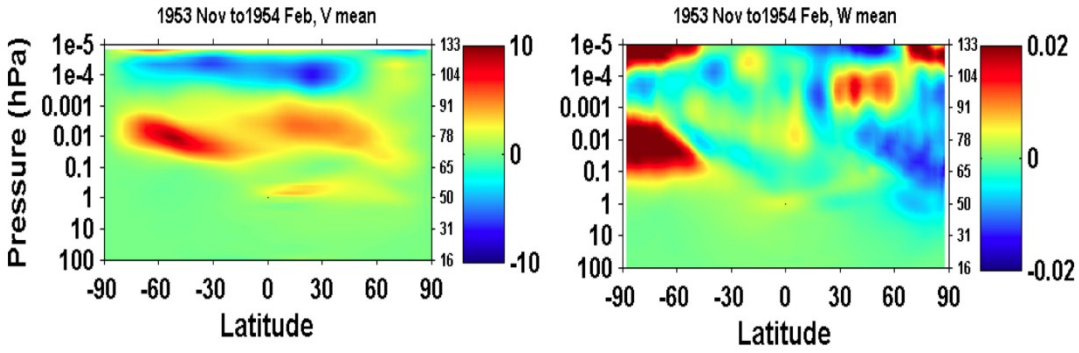

Figure 3.3: Meridional wind V (left) and vertical wind W (right) associated with the residual circulations computed from WACCM. The data were averaged from 1 Nov 1953 to 28 Feb 1954. The units for V and W are m/s. Northward and upward directions are defined as positive for V and W, respectively.

According to the residual circulation calculated from WACCM (Figure 3.3), there is a winter-to-summer circulation in the lower thermosphere (above 95 km). As illustrated in Figure 3.2d–i, the change of this winter-to-summer circulation in the lower thermosphere responds to the temperature anomalies in the northern stratosphere and produces the equatorial negative temperature correlation and the positive temperature correlation in the northern polar regions from 90 km to 120 km in Figure 3.2a–c. Likely associated with the weakening of the summer-to-winter circulation in the mesosphere, this winter-to-summer circulation in the lower

thermosphere also weakens and leads to temperature anomalies in the corresponding regions through adiabatic heating/cooling.

The results presented here show that the modeled temperature anomalies in the winter polar stratosphere are correlated with temperature and circulation anomalies at all latitudes between 15 and 110 km. Although the correlation coefficients at the high southern latitudes are small in Figure 3.2, the majority of them are statistically significant as indicated by the significance levels being above 95%. The small magnitudes of the southern correlation coefficients are most likely due to the inter- and intra-annual variations of the correlation patterns, as will be discussed in Section 3.3. Figure 3.2g–i show that all the circulations are affected by the anomalies in the winter polar stratosphere: the Brewer-Dobson circulation in the stratosphere, the summer-to-winter circulation in the mesosphere and the winter-to-summer circulation in the lower thermosphere. Changes in the circulations are responsible for the correlation patterns in the corresponding regions. Therefore, the temperature correlation patterns can be used as a proxy to identify the range and boundary of the circulations.

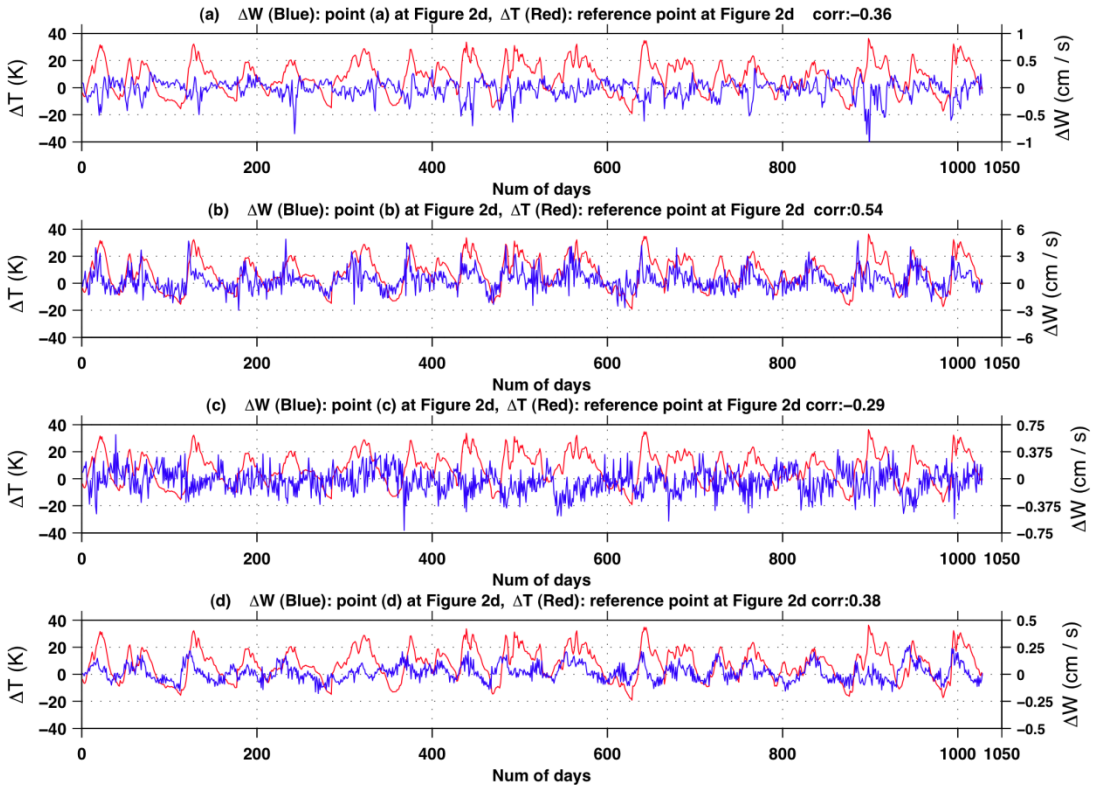

Figure 3.4: The time series of WACCM temperature anomalies (ΔT) (red solid line) at the reference point and the time series of WACCM vertical wind anomaly (ΔW) (blue solid lines) at four chosen points in Figure 3.2d. Figure 3.4a–d correspond to the points a, b, c and d in Figure 3.2d, respectively.

To directly examine the correlations between the residual circulation and temperature, we compare in Figure 3.4 the vertical wind time series taken at 4 different locations (a, b, c and d in Figure 3.2d) with the temperature time series at the reference point. The time series are formed by splicing together segments of temperature and wind every winter during the period of SSW, which is the same method used in forming time series in the calculation of Figure 3.2. The positive or negative correlations between the anomalies of the two quantities are significant, and all four correlations have significance levels above 99%. The correlations become even more evident when the wind data are smoothed over 10-days for every year before spliced together so

short-period fluctuations (periods of several days) are removed. The correlation coefficients are recalculated using the smoothed winds and the results are displayed in Figure 3.5. After the smoothing, the correlation patterns are nearly identical to the unsmoothed patterns shown in Figure 3.2 but with larger magnitudes of correlation coefficients in most regions. These tests confirm the existence of the correlations between temperature and vertical wind derived above. Figure 3.5 further suggests that the correlations exist in the multi-day periods more strongly than in the day-to-day variations.

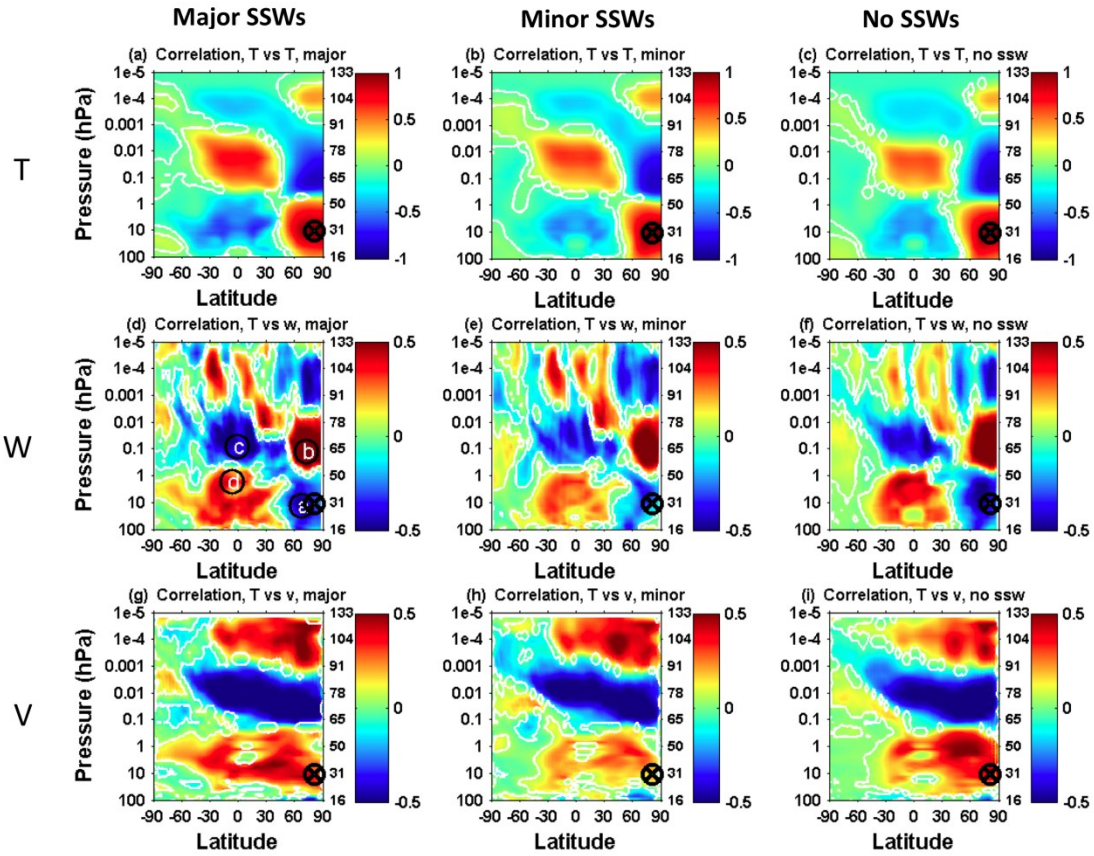

Figure 3.5: Similar to Figure 3.2, but the correlation patterns are calculated using the vertical wind and meridional wind smoothed over 10 day

3.5 Teleconnection Patterns versus SSW, Inter-Annual and Intra-Annual Variability

According to Figure 3.2, the correlation patterns from WACCM for the days with major SSWs, with minor SSWs and without SSWs are nearly identical. In Figure 3.1, the correlations from SABER for days with and without SSWs also have similar patterns. These results provide evidence that temperature anomalies during the periods of major SSWs, minor SSWs and no SSWs are all induced by anomalies of the planetary-wave driven branch of the residual circulation in the winter stratosphere. The differences among these three cases are in the amplitudes and signs of planetary wave anomalies and temperature perturbations. Strong positive perturbations show up as SSWs, while other perturbations are not considered as SSW. Our results are in agreement with a finding in CMAM by *Karlsson et al.* [2009] that either sign of the vertical component of the Eliassen-Palm flux in the winter stratosphere leads to the similar inter-hemispheric coupling patterns.

We notice in Figure 3.2 that the correlation magnitudes in the SH poleward of 60°S are relatively small when compared to the previous studies by, e.g., *Karlsson et al.* [2009a] and *Xu et al.* [2009]. Several factors may have contributed to the weak correlations in the southern polar region in the current study, including the time lag, the different reference point used in the current study, the intra-annual and inter-annual variations of correlation regions. We examine these factors one by one in the following.

In previous studies, *Becker and Fritts* [2006] suggested a time lag of ~1 month for the SH mesosphere temperature anomaly to respond to the NH planetary wave anomaly. *Karlsson et al*. [2009a] showed in the CMAM that the response time of the SH temperature to the NH planetary wave was 15–20 days while the temperature-to-temperature response time between two hemispheres was instantaneous. Using the MLS data, *Xu et al*. [2009] showed a

temperature-to-temperature response time ranging from 1 to 7 days at different correlation regions. To study the effects of time lag on the derived correlation patterns in Figure 3.2, we calculate the correlation coefficients for the time lags ranging from -10 days to +10 days relative to the temperatures at the reference point. The results are displayed in Figure 3.6. It is worth to point out that the time series used in Figure 3.6 are formed by simply joining 54 years of winter temperature or wind data together without separating them into different periods of major, minor and no SSWs. Figure 3.6a, 3.6c and 3.6e illustrate the maximum correlations obtained within the lags of -10 to +10 days, while the associated time lags for achieving the maximum correlations are plotted in Figure 3.6b, 3.6d and 3.6f. The maximum correlation patterns of T versus T in Figure 3.6a are nearly identical to the patterns of Figure 3.2a–c with zero lags. They all show strong correlations in the NH and equatorial regions but weak correlations in the SH poleward of 60°S. As a result, we conclude that the time lag is not the cause of the weak correlations in the southern polar region plotted in Figure 3.2. Furthermore, the time lags shown in Figure 3.6b for the regions with relatively large positive or negative correlations are close to zero, indicating that the temperature-to-temperature responses are instantaneous north of 60°S. Some large lag values show up in Figure 3.6b for the regions with small correlation magnitudes. Such lags should be discarded in the analysis because the correlations are fluctuated around 0, resulting in meaningless lags. The maximum correlation patterns of T versus W in Figure 3.6c and of T versus V in Figure 3.6e are similar to the corresponding correlation patterns with zero lags in Figure 3.2d–f and Figures 3.2g–i, respectively. Again, the time lags have very little effects on the correlation patterns. Interestingly, the time lags from 100 hPa to 0.001 hPa in the equatorial and northern hemisphere regions in Figure 3.6d and 3.6f are negative in general, indicating that the W and V wind anomalies lead the temperature anomaly at the reference point by 2 to 10 days.

This time lag of 2–10 days is smaller than the lag of temperature response to the planetary wave anomaly (15 days to 1 month) but larger than the lag of temperature response to temperature anomaly (instantaneous–7 days) in the northern stratosphere. Such a result is anticipated because the planetary wave anomaly occurs first and induces the residual circulation anomaly. The residual circulation anomaly in turn leads to the temperature anomaly that occurs last in the sequence.

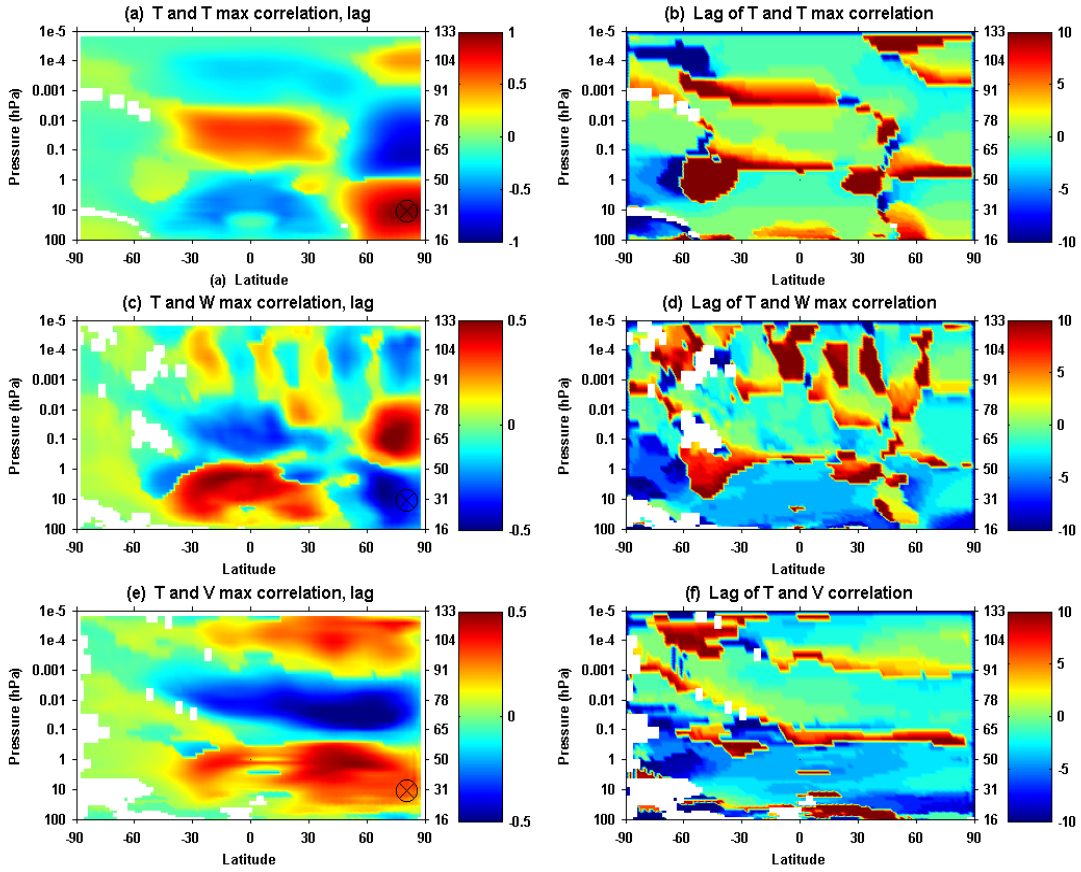

Figure 3.6: The maximum correlation coefficients for temperature (T) in Figure 3.6a, vertical wind (W) in Figure 3.6c and meridional wind (V) in Figure 3.6e obtained within the time lags of -10 to +10 days. The time lags corresponding to the maximum correlation coefficients are plotted in Figure 3.6b, 3.6d and 3.6f. The insignificant points have been removed from all plots and appear as white spots or areas.

The reference point chosen in the northern stratosphere to calculate the correlations in the current study is different than the southern mesosphere reference used in previous studies. To investigate whether the reference point plays a role in the correlation magnitudes, we calculate the correlation patterns for January of 1953–1955 using both reference points in Figure 3.7. We chose those three years for demonstration, other years show similar results. On the left, Figure 3.7a, 3.7c and 3.7e employ a reference point in the southern mesosphere (averaged from 50°S to 90°S and from 1.2×10^{-4} hPa to 4×10^{-3} hPa), similar to that used in Figure 1a of *Karlsson et al.* [2009a]. The area used to calculate the reference point is marked as a black rectangle in each plot. On the right, Figure 3.7b, 3.7d and 3.7f use the same reference point in the northern stratosphere as Figure 3.2. Figure 3.7a and 3.7b show very similar correlation patterns; however, Figure 3.7c and 3.7d exhibit the opposite correlations in general. Comparing Figure 3.7e with Figure 3.7f, while Figure 3.7f using the NH stratosphere reference point gives clear correlation pattern with large correlation magnitudes, Figure 3.7e using the SH mesosphere reference point gives very small correlations globally. The puzzling results above can be explained by the height variations of the correlation regions in the southern polar region. In Figure 3.7b, the reference point in the NH stratosphere and the reference point area in the SH mesosphere (inside the black rectangle) are positively correlated, leading to the similar correlation patterns of Figure3 3.7a and b. According to Figure 3.7d, the temperature anomalies at two reference points are anti-correlated; therefore, Figure 3.7c and 3.7d have opposite signs of correlation patterns. In Figure 3.7f, half of the reference point area in the SH mesosphere is positively correlated with the reference point in the NH stratosphere while the other half is anti-correlated. Consequently, Figure 3.7e does not show clear correlation patterns when the reference point rectangle in the SH mesosphere is used. Regarding the high southern latitudes, Figure 3.7b and 3.7f show that the large correlations

(nearly 1) are achieved in the SH poleward of 60°S using the single year and single month data with the reference point in the NH stratosphere. This means that the reference point chosen in this study is not the cause of small correlation coefficients in the southern polar region. Furthermore, the results shown in Figure 3.7 indicate the advantages of choosing a reference point in the NH stratosphere. That is, despite some changes in the SH polar region in Figure 3.7d, the patterns in the equatorial and NH regions are stable and consistent in Figure 3.7b, 3.7d and 3.7f. Such advantages can be seen even more clearly in the inter-annual and intra-annual variations of correlation regions to be discussed below.

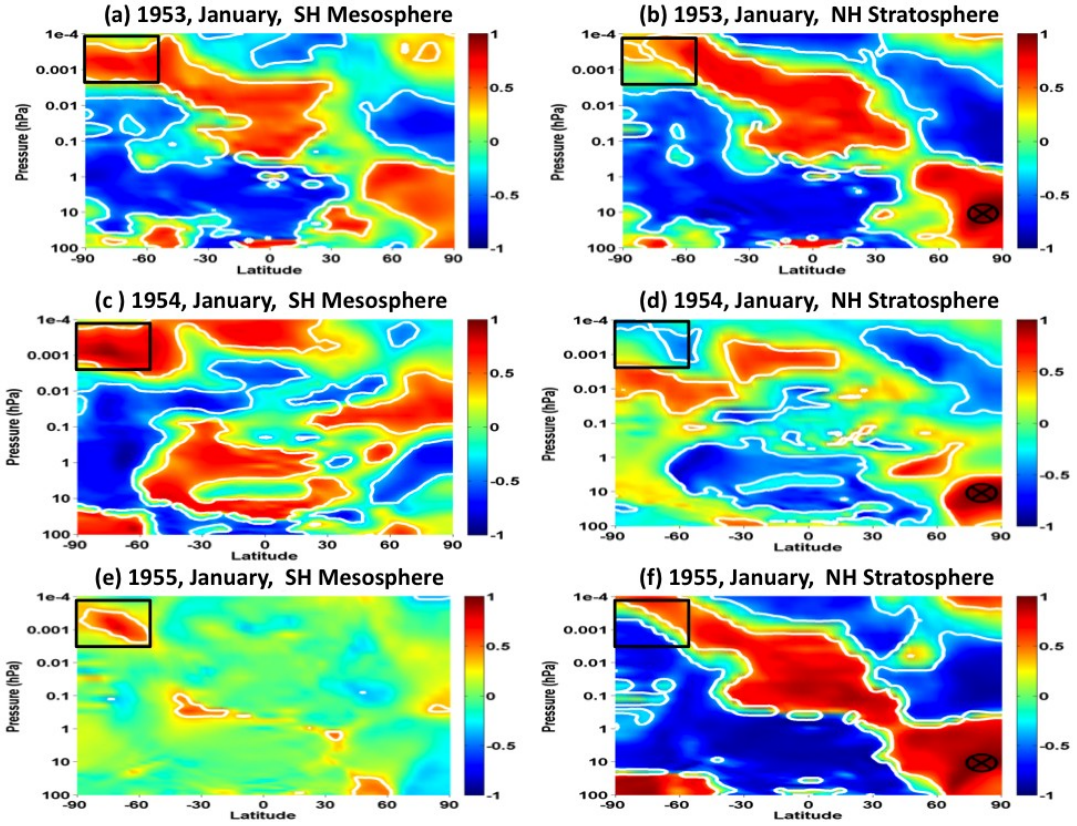

Figure 3.7: Correlation patterns of WACCM temperatures for January 1953, 1954 and 1955. In Figure 3.7a, 3.7c and 3.7e, the reference points are located in the southern mesosphere (averaged from 50°S to 90°S and from 0.00012 to 0.004 hPa), similar to the reference point used in Figure 1a of *Karlsson et al.* [2009a]. In Figure 3.7b, 3.7d and 3.7f, the reference points are located in the northern stratosphere, marked as symbol 'X' inside black solid cycles. White solid lines denote the 95% significance level.

To study the inter-annual variations of teleconnection, the temperature correlation patterns are calculated from WACCM for individual years from 1953 to 2006. Regions with significant positive and negative correlations exists poleward of 60°S each year, but the altitudes of these regions vary from year to year through all 54 years. Figure 3.8 illustrates the yearly correlation patterns from 1953 to 1958 as examples. For the winters of 1953–1954 and 1954–1955, a positive correlation region with a significance level above 95% occurred poleward of 60°S in the altitude range of 80–90 km. However, it moved to 90–100 km in the winter of 1956–1957. For the winters of 1957–1958 and 1958–1959, the positive correlation region was located even above 100 km. Similarly, the negative and positive correlation regions below 80 km exhibit inter-annual altitude variations at the latitudes poleward of 60°S. Indeed, the inter-annual variations have shown up in Figure 3.7 where using the January data and a reference point in the NH stratosphere, the correlation regions in the southern polar region have different altitudes every year, further confirming the existence of inter-annual variations. Therefore, when averaged over multiple years, the correlations in the SH poleward of 60°S are largely canceled out due to the inter-annual variations. A direct consequence is the correlations calculated in the current study being small in the SH poleward of 60°S as shown in Figure 3.2. In contrast, the positive and negative correlation regions in the equatorial and NH regions are quite consistent over the years, leading to the clear patterns after multiple-year averaging. These facts also demonstrate the advantage of stable patterns around the equator and in the NH when a reference point in the NH stratosphere is chosen in the correlation studies.

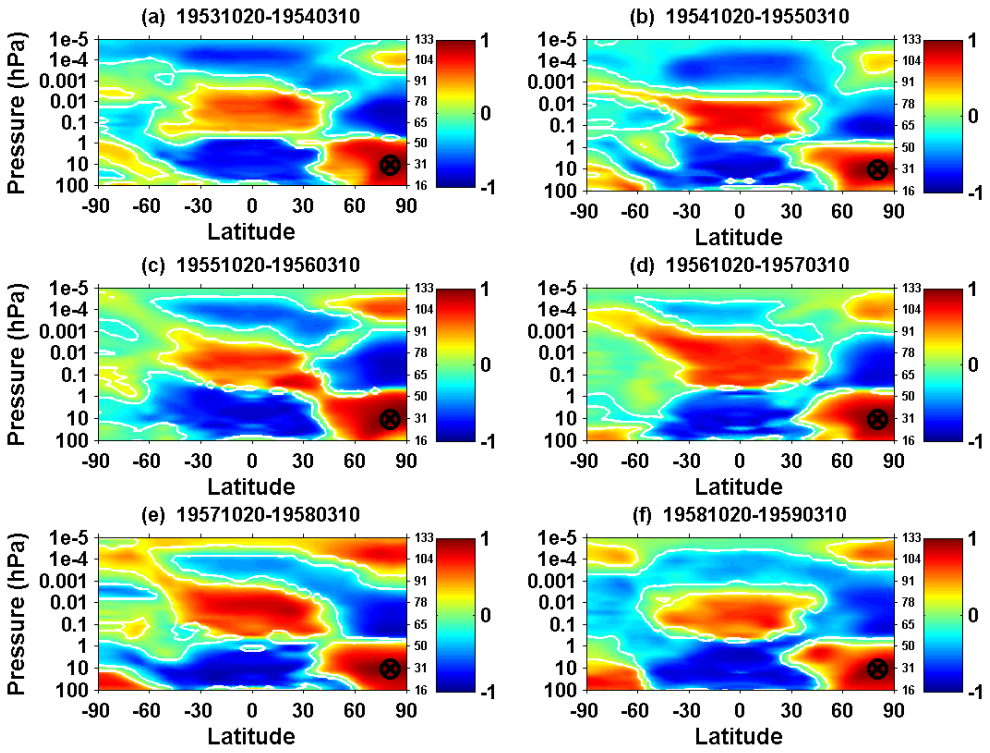

Figure 3.8: Correlation patterns between the WACCM temperature anomalies at the reference point (10 hPa, 80°N) and at all latitudes and altitudes for the winters from 1953 to 1958. The title of each subplot gives the dates of data period in the format of "yyyymmdd–yyyymmdd". The symbol "X" is the reference point used for the correlations. White solid lines denote the 95% significance level.

In addition to the inter-annual variability, the results in Figure 3.7 and Figure 3.8 also indicate the intra-annual variations. The correlation patterns for January 1955 (Figure 3.7f) show strong correlations at the high southern latitudes; however, the correlation patterns for the entire winter from 20 October 1954 to 10 March 1955 (Figure 3.8) give much weaker correlations at the same latitudes. This difference can be easily explained by the altitude variations from November through February, as the correlations are largely smoothed out when 4 winter months are combined together. To further investigate the intra-annual variations, the monthly correlation

patterns are calculated using all 54 years of WACCM data and the results are displayed in Figure 3.9. The time series used in Figure 3.9 are formed via splicing together the 54 years of temperature data in each of the months (November through February). The intra-annual altitude variations of the correlation regions are obvious at the high southern latitudes. Three correlation regions with the significance levels above 95% (i.e., the positive correlation from ~1×10^{-3} to 1×10^{-4} hPa, the negative correlation from ~10 to 0.001 hPa, and the positive correlation from about 100 to 10 hPa) in the SH poleward of 60°S all have altitudes varying from one month to another. The intra-annual variations of correlation pattern altitudes cause the correlations at the high southern latitudes to be smoothed out when the correlations are calculated for all the winter months. Therefore, the intra-annual variations likely contribute to the weak correlations in the southern polar region shown in Figure 3.2 and Figure 3.5. Note that the correlation patterns in the equatorial and NH regions are located at the same altitudes from the stratosphere to the lower thermosphere for all winter months, suggesting the advantage of choosing a reference point in the northern polar stratosphere.

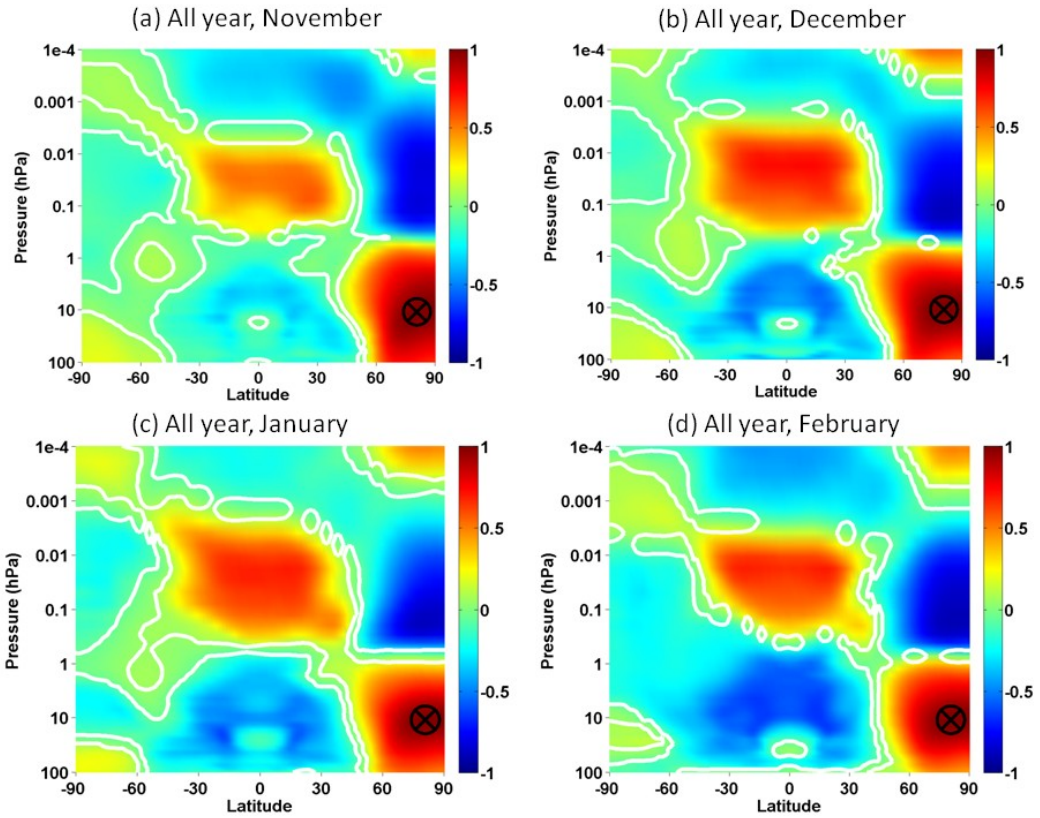

Figure 3.9: Correlation patterns between the WACCM temperature anomalies at the reference point (10 hPa, 80°N) and temperature anomalies at all latitudes and altitudes for November (a), December (b), January (c) and February (d). The symbol "X" is the reference point used for the correlation calculations. White solid lines denote the 95% significance level.

In summary, the time lag is not the reason of weak correlations at the high southern latitudes. The reference point in the northern stratosphere has the advantage to show stable teleconnection patterns in the equatorial and NH regions, but it is not the cause of weak correlations in the southern polar region. The inter-annual and intra-annual altitude variations of the correlation regions are most likely responsible for the weak correlations at the high southern latitudes. It is worth to point out that time series of daily and zonally averaged data from WACCM are used to calculate the correlation patterns in this study, while *Karlsson et al*. [2009a]

used monthly and zonally averaged data from CMAM. The WACCM results do not necessarily represent a difference to the teleconnection in the CMAM.

3.6 Magnitudes of Temperature Anomalies

It is of interest to quantify the magnitudes of temperature anomalies under different SSW conditions. We take the time series of WACCM temperature anomalies (like the example shown as the red lines in Figure 3.4) for each location and compute its root-mean-square (RMS) value. The result represents the RMS magnitude of temperature anomalies at that location. Such computation is repeated for major, minor and no SSWs, respectively. The resulted global maps of RMS magnitude versus latitude and altitude are displayed in Figure 3.10. The RMS magnitudes at the northern polar region reach local maxima around 0.1 hPa and 5 hPa. At the southern polar MLT region, the RMS magnitudes reach a local maximum around 0.001 hPa with values of 14, 11 and 11 K for major, minor and no SSWs, respectively. Around equatorial regions, the RMS magnitudes of temperature anomalies are less than 5 K below the thermosphere. In general, the magnitudes of temperature anomalies during major SSWs are larger than those during minor and no SSWs. To some extent, these RMS magnitudes of temperature anomalies indicate the temperature responses to different SSW conditions. But cautions must be taken when interpreting the results, because altitude variations and annual variations may obscure the temperature anomalies to reveal the real temperature responses.

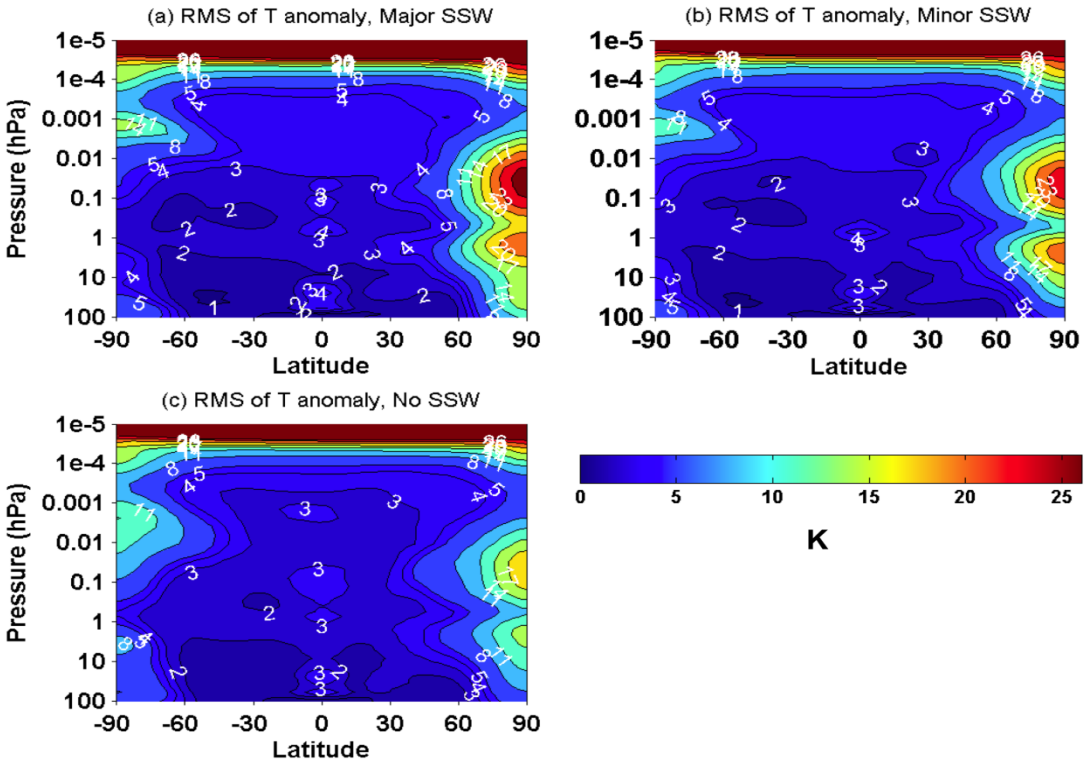

Figure 3.10: RMS magnitudes of temperature anomalies (unit: K) during (a) major, (b) minor and (c) no SSWs.

3.7 Mechanisms of Teleconnection

The teleconnection patterns and the changes of residual circulations are plotted in the Figure 3.11. Figure 3.11a shows the residual circulation simulated in WACCM. During the northern winter, Brewer-Dobson circulation at the stratosphere is from the equatorial region to the North Pole. The pole-to-pole meridional circulation in the mesosphere is northward and the pole-to-pole meridional circulation in the lower thermosphere is southward. A planetary wave anomaly in the winter stratosphere triggers the whole teleconnection process [*Körnich and Becker*, 2010]. In the following description we consider an increase of planetary wave forcing. A decrease of planetary wave forcing is equally valid with opposite signs for all the temperature

and circulation changes. When there is an increase of planetary wave forcing in the northern stratosphere, the associated circulation changes are marked as black arrows in the Figure 3.11.

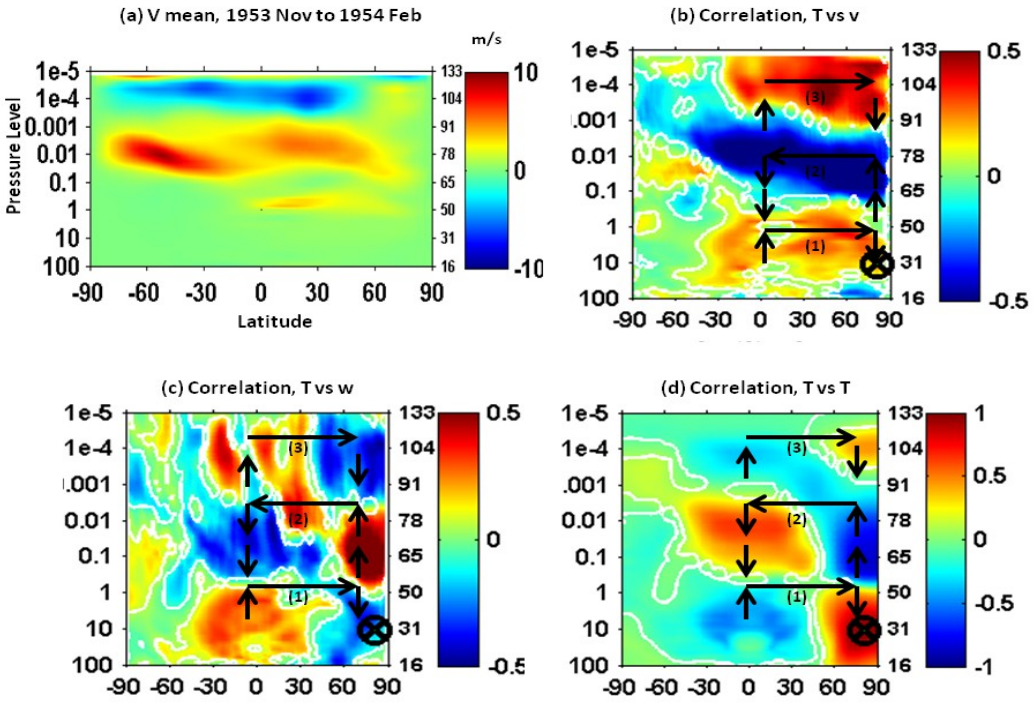

Figure 3.11: Residual circulation and teleconnection pattern, same patterns as Figure 3.2 and Figure 3.3. Black arrows represent the change of residual circulation associated with an increase of planetary wave forcing in the northern stratosphere.

The planetary wave forcing in the northern stratosphere during winter is westward in the quiet atmosphere, as shown in Figure 1 of *Körnich and Becker* [2010]. In step (1), as marked in Figure 3.11b–d, when an increase of westward planetary wave forcing occurs in the northern stratosphere, an increase of the northward Brewer-Dobson circulation and a decrease of eastward zonal wind jet in the northern stratosphere are induced. In the northern polar region above 45ºN,

the increase of Brewer-Dobson circulation induces more downwelling below 1 hPa and more upwelling above 1 hPa because of the atmosphere continuity as illustrated in Figure 3.11c. In the equatorial region, this increase induces more downwelling above 1 hPa and more upwelling below 1 hPa. The downwelling and upwelling lead to heating and cooling respectively through adiabatic heating/cooling. Therefore, temperature at the reference point is increased due to adiabatic heating. When the temperature at the reference point increases, the positive (negative) correlation patterns of temperature in Figure 3.11d represent the regions of heating (cooling). The corresponding negative (positive) correlation regions of vertical wind in Figure 3.11c indicate the enhanced downwelling (upwelling) or reduced upwelling (downwelling). In the meantime, the positive (negative) correlations in the meridional wind patterns shown in Figure 3.11b imply either the enhanced (reduced) northward circulation or the reduced (enhanced) southward circulation.

In step (2), as marked in Figure 3.11b–d, when the eastward zonal wind in the northern stratosphere is decelerated by the increase of westward planetary wave forcing, the filter conditions of gravity waves are changed and more eastward gravity waves are able to propagate to the mesosphere. During the northern winter, the total gravity wave forcing in the northern mesosphere is westward and the increase of eastward gravity wave decreases the westward wave forcing. This decrease of westward gravity wave forcing decelerates the meridional circulation in the mesosphere therefore the direction of circulation change in the mesosphere is southward. In the northern polar region above 45ºN, the circulation change in the mesosphere leads to more downwelling above 0.01 hPa and more upwelling below 0.01 hPa. In the equatorial region, this circulation change leads to more upwelling above 0.01 hPa and more downwelling below 0.01

hPa. The adiabatic heating and cooling associated with the downwelling and upwelling are responsible for the observed correlations in the mesosphere in Figure 3.11.

In step (3), as marked in Figure 3.11b–d, the southward meridional circulation in the lower thermosphere is decelerated therefore the direction of circulation change in the lower thermosphere is northward. One potential mechanism for this circulation change is the continuity of atmosphere. The mesosphere circulation changes not only cause upwelling and downwelling below this circulation altitude but also induce more upwelling in the equatorial region and more downwelling in the northern polar region above this mesosphere circulation. This may drive the circulation in the lower thermosphere with opposite direction to the mesospheric circulation.

In Figure 3.11a, the two residual circulations in the mesosphere and lower thermosphere appear to be pole-to-pole. However, the circulation speeds in the middle-high latitude in both hemispheres are larger than near the equatorial region, which implies the existence of vertical wind between the two circulations in the equatorial region. The pole-to-pole meridional circulation can be considered as the superposition of a pole-to-pole circulation, an equator-to-north pole circulation in the northern hemisphere and an equator-to-south pole circulation in the southern hemisphere. This description works for both the mesosphere circulation and the lower thermosphere circulation. When the meridional circulation in the mesosphere in the northern polar region has an anomaly, this anomaly leads to anomaly in both the pole-to-pole circulation and equator-to-north pole circulation. The anomaly of equator-to-north pole circulation leads to vertical wind anomaly in the equatorial region which produces positive correlation region in the equatorial mesosphere and negative correlation region in the equatorial thermosphere as showed in Figure 3.11d. The pole-to-pole circulation anomaly

is able to reach the southern polar region as shown in Figure 3.11b and produce positive correlation region in the southern upper mesosphere as shown in Figure 3.11d.

The results in current study agree with previous studies on the mechanism of wave-mean flow interaction for the planetary waves in the northern stratosphere and gravity waves in the northern mesosphere. However, we extend the teleconnection to the lower thermosphere and introduce a potential mechanism of the thermosphere circulation. This study shows very clear teleconnection pattern in the lower thermosphere which has opposite signs to the mesospheric teleconnection pattern. The relationship between temperature anomalies and vertical wind anomalies are established in the equatorial region and in the northern hemisphere from the stratosphere to the lower thermosphere. From the facts that the changes of temperature and vertical wind are always in opposite direction, we conclude that the mechanism of temperature changes in the teleconnection process are mainly adiabatic cooling/heating induced by the residual circulation anomalies. Based on the continuity of atmosphere around mesopause, we provide a potential explanation for the formation of residual circulation in the lower thermosphere. Furthermore, from the circulation and teleconnection patterns, it is reasonable to assume that the meridional circulation in the mesosphere and lower thermosphere have vertical components in the equatorial region, even though the main components of both circulations appear to be pole-to-pole. The vertical components transport the circulation anomalies between these two meridional circulations.

3.8 Conclusions

We have established the teleconnection patterns of temperature anomalies in the northern polar stratosphere with temperature or wind anomalies at global latitudes and altitudes from 15 to 110 km using SABER temperature data and WACCM simulations of zonally and daily averaged

temperatures and winds. The correlation patterns show that teleconnection exists globally over the entire equatorial, mid- and high-latitudes and from the stratosphere to the lower thermosphere. Along with previous studies, these two new datasets further demonstrate the robustness of the teleconnection pattern and its role as an important atmospheric coupling mechanism. The correlation patterns between the temperature anomalies and residual circulation anomalies are established using the WACCM simulations. The WACCM correlation patterns reveal that temperature anomalies from the stratosphere to the thermosphere correspond well to the corresponding anomalies of residual circulations through adiabatic heating and cooling. These circulation anomalies are induced by planetary wave anomalies in the northern polar stratosphere. Since the residual circulations have clear responses to the anomalies and form different correlation regions, the correlation patterns may be used as a proxy to identify the boundaries of the circulations.

A main new finding of this study is that the teleconnection extends well into the lower thermosphere and the thermospheric anomalies are consistent with the corresponding changes of the winter-to-summer lower-thermospheric branch of the residual circulation. Although this is the first report in which the teleconnection between the stratosphere and the thermosphere is clearly identified, we notice that the Figure 4b and 4d in *Karlsson et al.* [2009b] derived from MLS temperature data hint some coupling between the thermosphere and the stratosphere, thus another dataset supporting our finding. Our results demonstrate that the stratosphere perturbations can have strong influences on the thermosphere via teleconnection, which may have important implications to the thermosphere research. For example, the temperature perturbations will lead to the changes in the thermosphere density, affecting space weather, especially the satellite drag. The changes in the thermospheric residual circulation will influence

the constituent transport, e.g., affecting the $[O]/[N_2]$ ratio that can impact the ionosphere via various processes.

We have examined the teleconnection for time periods with and without SSWs using a reference point chosen in the northern winter stratosphere in order to be consistent with the definition of a SSW. It is found that the teleconnection patterns do not depend on the presence of SSWs. That is, the teleconnection structures for time periods with and without SSWs display similar patterns in SABER, and teleconnection patterns in WACCM are nearly identical for days with major SSWs, minor SSWs and without SSWs. Such similarities occur in the correlation patterns of temperature versus temperature and also of temperature versus residual circulation. These results indicate that major SSWs, minor SSWs and small temperature anomalies are likely caused by similar mechanisms but with different magnitudes; that is, anomalies of circulations driven by planetary waves in the winter stratosphere.

The current study using WACCM simulations discovers strong inter-annual and intra-annual altitude variations of the teleconnection patterns in the southern polar region but stable altitudes of correlation regions in the equatorial and northern latitudes. The correlation magnitudes in the SH poleward of 60°S are relatively small in the current study when compared to the previous studies by, e.g., *Karlsson et al.* [2009a] and *Xu et al.* [2009]. Our investigations of the weak correlations conclude the following. The time lag is not the reason of weak correlations at the high southern latitudes. The reference point in the northern stratosphere has the advantage to show clear and stable teleconnection patterns in the equatorial and NH regions when 54 years of data are combined together to calculate the correlation patterns, and it is not the cause of weak correlations in the southern polar region. The inter-annual and intra-annual altitude variations of the correlation regions are most likely responsible for the weak correlations at the high southern

latitudes. This is because the positive and negative correlations are largely canceled out when the correlation patterns are averaged over 54 years or over 4 winter months, although single year and single month data yield large correlations in the southern polar region.

The time lag has very little effects on the teleconnection patterns as shown by the current study; however, our time lag analysis indicates that from 100 to 0.001 hPa in the equatorial and northern hemisphere regions, the vertical and meridional wind anomalies lead the temperature anomaly at the reference point by 2 to 10 days. This time lag is smaller than the lag of temperature response to the planetary wave anomaly (15 days to 1 month) but larger than the lag of temperature response to temperature anomaly (instantaneous–7 days) in the northern stratosphere. Such a result suggests that the planetary wave anomaly occurs first and induces the residual circulation anomaly. The residual circulation anomaly in turn leads to the temperature anomaly that occurs last in the sequence.

We believe that the current study with SABER and WACCM has effectively broadened and furthered our understanding of the global teleconnection phenomena and possible underlying mechanisms. The correlation patterns in the region from 50°S to the North Pole are stable from year to year, within a year and with various SSW intensities in WACCM. It implies that the first two stages of the inter-hemispheric coupling mechanism as outlined in *Körnich and Becker* [2010], which are responsible for the correlation patterns northward of 50°S, are generally stable. On the other hand, the third stage of the coupling, where the perturbation propagates through the mesosphere and lower thermosphere from the equator to the summer pole, is much more variable, particularly poleward of 60°S, and this leads to the strong inter- and intra-annual altitude variations in the southern polar region as found by the current study. Nevertheless, there are still considerable issues to be addressed in the future studies and we have identified several in Section

3. Furthermore, the origin of the inter-annual and intra-annual variations of the correlation patterns in the southern polar region deserves good attentions. One possible mechanism is the intra-hemispheric coupling proposed by *Karlsson et al.* [2011]. Variations in the timing of the late-spring breakdown of the stratospheric polar vortex in the SH [*Langematz and Kunze*, 2008] may influence the propagation of gravity waves up to the mesosphere, thus adding an intra-hemispheric control from the stratosphere to the MLT temperature. This is additional to the inter-hemispheric coupling discussed above. When a reference point is chosen in the northern polar winter stratosphere as we did in the current study, only if the anomalies in the southern MLT region is mainly controlled by the anomalies of the planetary-wave driven branch of the residual circulation (that is, the inter-hemispheric coupling), will the correlation regions occur with stable altitudes in the southern MLT. It is possible that the intra-hemispheric waves within the southern polar region strongly influence the southern MLT region, leading to the large altitude variations of the correlation regions in different months or years. Using a reference point in the northern winter stratosphere may help the studies of intra-hemispheric coupling by revealing the variations of correlation regions under different dynamic conditions.

Chapter 4 Modeling Study of the Impacts of Inertial Gravity Wave on the Cold Pole Bias in WACCM Simulation

The 'cold pole' problem refers to the cold bias of polar stratosphere temperature in the southern hemisphere in most general circulation models (GCMs) and chemistry climate models (CCMs) during the winter and spring. Accompanying the 'cold pole' is the stronger jet in the stratosphere and later vortex breaking. It is a long-standing problem in most models, implying the lack of wave forcing in the southern stratosphere. In current study we try to reduce the 'cold pole' bias in the Whole Atmosphere Community Climate Model (WACCM 4.0) through new gravity wave parameterization. Although inertial gravity waves can strongly affect the middle and upper atmosphere circulation, they are missing from the current parameterization scheme in WACCM. Furthermore, inertial gravity waves usually break at lower altitudes than mesoscale waves according to linear saturation theory. Inertial gravity wave drag is thus a candidate of the missing wave forcing responsible for the 'Cold Pole' bias in WACCM. To test this hypothesis, additional inertial gravity waves are launched while the original mesoscale gravity waves in WACCM are kept. Using the new gravity wave scheme, the simulated wintertime temperature is ~20 K warmer in the southern polar region while the simulated wintertime zonal wind jet is about 10 to 30 m/s slower than the originals. Also, the polar vortex in the southern hemisphere breaks earlier and the wind reversal level during spring is lower. All these changes make the WACCM simulations closer to ERA-40, suggesting that additional inertial gravity waves are able to reduce the 'cold pole' bias.

4.1 Introduction

In many general-circulation models (GCMs) and chemistry-climate models (CCMs), the simulated temperature in the southern polar region during winter is colder than observations. This is called 'cold pole' problem and it is a long lasting problem in most models. Associated with the cold pole bias in the southern polar region, the wintertime stratospheric polar vortex is excessively strong and persists too long into the southern summer, and the wind reversal level during spring is too high. For most of the CCMs, cold bias mainly exists in the southern hemisphere during winter and spring. In the northern hemisphere, the cold pole bias is much smaller [*Austin et al.* 2003; *Erying et al.* 2006; *Garica et al.* 2007].

Austin et al. [2003] studied the simulation results of nine CCMs using 10 years of UKMO assimilation temperature as a reference. All nine models have a cold pole bias from 5 K to 30 K during winter at the southern polar region, while the temperature climatology at the northern hemisphere is generally consistent with UKMO. In *Erying et al.* [2006], thirteen CCM models are studied and compared with ERA-40. Twelve out of thirteen models show definite cold pole bias from 5 K to 15 K at the southern polar region during winter. Most of these models show correct temperature simulations during the northern winter.

Resolving this cold pole bias is critical in the study of stratosphere dynamics, chemistry and middle atmosphere climate. For example, stratospheric wind is crucial for the propagation of planetary waves and gravity waves, and temperature is a critical factor in the study of ozone chemistry. Ozone depletion during southern winter and spring in the polar region is very sensitive to the simulated temperature. Low temperatures lead to the formations of polar stratospheric clouds (PSC), which in turn increase ozone depletion in the southern polar region during spring, making the ozone depletion too strong and the ozone recovers too late. This can

lead unphysical simulation of ozone hole in Antarctica. The stratospheric wind and temperature structure may also affect tropospheric climate. It is therefore important to reduce such cold bias in model simulations.

The cold pole bias which exists in most CCMs is believed to be caused by the lack of wave forcing in the southern stratosphere. This waving forcing could be planetary wave drag or gravity wave drag. In most of the models, planetary wave can be resolved, but gravity waves need to be parameterized in the models due to its small spatial scale, and wave breaking cannot be directly resolved. To make the models computational practical, a limited number of gravity wave components are used, and in current standard WACCM parameterization their horizontal wavelengths are all set to 100km. Therefore, the cold pole bias can be attributed to missing gravity waves (GWs) (orographic, nonorographic, or both) in the southern hemisphere. *Austin et al.* [2003] stated that the development of non-orographic GW schemes for climate models [*Medvedev and Klaassen,* 1995; *Hines,* 1997; *Warner and McIntyre,* 1999] significantly reduce the cold pole bias in the southern polar region during winter comparing with those models relying on Rayleigh friction to decelerate the polar night jet such as *Manzini and McFarlane* [1998]. *McLandress et al* [2011] successfully used orographic GW drag around 60° S to reduce the cold pole bias in the Canadian Middle Atmosphere Model (CMAM). They justify their GW scheme that even though most of the mountains are at the northern hemisphere, there are some small islands located at 60° S and they can produce large local drag forces [*Alexander et al.,* 2009]. But those small islands are not resolved in many current models. Moreover, in current GWD parameterizations orographic and nonorographic GW waves propagate straight up, however *Sato et al*. [2009] reveals that mountain waves forced over the Antarctic Peninsula and Southern Andes are refracted toward 60ºS [*McLandress et al,* 2011]. Those evidences imply that

the orographic gravity wave forcing around 60° S is missing and this missing orography wave forcing may be the reason of the cold pole bias.

This missing orographic gravity wave forcing around 60° S is one possible source of the missing wave forcing, but it is may not the only one. *Wang et al* [2005] used 5 years (1998 – 2002) of high resolution radiosonde data over almost 90 stations to derive the gravity wave information in troposphere and lower stratosphere. The gravity wave parameters are estimated using the derived temperature and wind perturbations. The horizontal wavelength of gravity waves they observed is from 2500 km at the low latitudes to 300 km at the northern polar region. They also stated that gravity waves have a wide spectrum but radiosonde can only detect part of the spectrum. *Alexander et al* [2008] used the high resolution temperature profiles from High Resolution Dynamics Limb Sounder (HIRDLS) to derive gravity wave parameters globally. In their study, the averaged gravity wave horizontal wave lengths over the altitude range 20 – 30 km are analysed in three latitude bands, 15° S to 15° N, 40° S to 63° S and 40° N to 63° N. All three latitude bands shows horizontal wavelength from around 300 km to more than 3000 km. Gravity waves with horizontal wavelength more than 1000 km dominates the observed gravity waves in all three latitude bands. Moreover, *Wang et al* [2005] and *Alexander et al* [2008] showed that gravity waves also have latitude dependence and seasonal variance. Although it is not practical to fully parameterize the wide spectrum of gravity waves and the latitude and seasonal variances of gravity waves in CCMs, a simplified representation of the inertial gravity waves (IGWs), in addition to the mesoscale gravity waves, is necessary and feasible.

In WACCM, both orographic and nonorographic gravity waves are parameterized, but all the parameterized gravity waves are mesoscale internal gravity waves with a horizontal wavelength of 100 km, which break mostly in the mesosphere. The gravity waves with longer

horizontal wavelength are neither resolved or parameterized in WACCM, even though they are observed by radiosonde and HIRDLS. This is a likely cause for the absence of quasi-biennial oscillation (QBO) in WACCM. To address this problem, *Xue et al*., [2012] developed and implemented an IGW scheme for the latitudes between 30° S to 30° N in WACCM, which is capable of producing QBO internally. In reality, however, inertial gravity waves exist at all latitudes and should be properly parameterized globally. IGWs generally have much longer horizontal wavelengths than mesoscale waves, so they tend to break at lower altitudes than mesoscale waves [*Holton* ,1982]. It is conceivable that the IGWs at middle to high latitudes can provide additional wave forcing in the stratosphere that helps reducing the cold pole bias. This hypothesis will be tested in WACCM simulation. Like in *Xue et al* [2012], the representative horizontal wavelength we choose is 1000 km for the IGW parameterization. Specifically, this study extends the IGW parameterization in WACCM developed in *Xue et al.* [2012] to higher latitudes, and examines its effects in the stratosphere and its capability in reducing the cold bias. The simulated wintertime temperature, zonal wind, polar vortex breaking and wind reversal level will be compared with European Centre for Medium-Range Weather Forecasts (ECMWF) 40 year Re-analysis (ERA-40) to identify the difference between WACCM simulation and observation. Section 4.2 gives a description of the newly implemented inertial gravity wave scheme. Section 4.3 and Section 4.4 shows the simulated results using the new inertial gravity wave scheme and compares the results with observations and the simulated results using the original gravity wave scheme. Section 4.5 is the summary and discussion of the above results.

4.2 Model and Data Description

The National Center for Atmospheric Research (NCAR) Whole Atmosphere Community Climate Model (referred to as WACCM 4.0) used in this paper is a comprehensive numerical model which is released in June 2010 as part of the NCAR CESM1.0. WACCM4.0 is an extension of the Community Atmosphere Model (CAM), which form the atmosphere component of the Community Earth System Model, version 1.0 (CESM 1.0). The WACCM4.0 model has 66 pressure levels from the ground to $5.1 \times$ hPa. The top level is at ~145 km. The model altitude intervals change with altitude. The intervals are about 1 km at 20 km and 3 km at 100 km. The longitude and latitude resolution used for this study are 1.9 degree and 2.5 degree.

WACCM4.0 incorporates a parameterization for a spectrum of vertically propagating internal gravity waves based on the work of *Lindzen* [1981], *Holton* [1982], Garcia and *Solomon* [1985] and *McFarlane* [1987]. Non-orographical gravity waves are launched from deep convection and frontogenesis according to the trigger functions that depend on the atmospheric state computed in WACCM4.0 at any given time and location, as discussed by *Richter et al.* [2010] and *Neale et al*. [2010].

With the gravity wave parameterizations described above, QBO cannot be produced internally. WACCM4.0 provides the choice to impose QBO by nudging the tropical wind to observations based on *Balachandran and Rind* [1995]. *Xue et al.* [2012] modified the gravity wave parameterization of WACCM4.0 and successfully produce a QBO internally by adding an IGW scheme. In the current study, the inertial gravity wave scheme of *Xue at al.,* [2012] will extended to higher latitudes.

ECMWF is the data set provided by The European Centre for Medium-Range Weather Forecasts. ECMWF data are derived from global four-dimensional assimilation of various

atmospheric observations into the ECMWF model. The outputs are average temperature profiles every 6 hour. Resolution of latitude and longitude are both 2.5 degrees. ERA-40 is an ECMWF re-analysis of the global atmosphere and surface conditions from mid-1957 to mid-2002. There are 60 levels in the vertical from 0.1 to 1000 hPa. The latitude and longitude are 1.4 deg and 1.4 deg, respectively. The monthly mean temperatures are averaged over 45 years to form the temperature climatology each month [*Uppala et al.* 2005]. The ERA-40 temperature climatology is used to compare with WACCM simulations.

4.3 New Gravity Wave Scheme

The originally parameterized GWs in WACCM4.0 are mesoscale waves with a horizontal wavelength of 100 km. The breaking of these waves is formulated based on the linear saturation theory by *Lindzen* [1981]. Most of these waves break in the mesosphere and lower thermosphere (MLT). According to *Holton* [1982], the gravity wave breaking altitudes $z \propto 2H\ln(\frac{2\pi}{\lambda_h A})$, where z, H, λ_h and A represent the breaking level, scale height, horizontal wavelength and amplitude of vertical winds at launching level, respectively. Accordingly, 10 times increase in horizontal wavelength will lead to a decrease of z by about 32 km, which may account for the missing forcing in the stratosphere. Because these waves are likely IGWs, the linear saturation theory of *Lindzen* [1981] needs to be extended to include Coriolis force [*Xue et al.,* 2012].

The dispersion relation of IGW with Coriolis effect [*Xue et al.*, 2012]:

$$m^2 = \frac{N^2}{(c-U)^2 - f^2/k^2}$$

m, N, U, c, f, k are the vertical wave number, buoyancy frequency, the background zonal wind speed, the gravity wave phase speed, the Coriolis parameter and horizontal wave number, respectively.

The new critical level for IGW [*Xue et al.*, 2012]:

$$c = U \pm \frac{|f|}{k}$$

The momentum flux at the saturation level for IGW [*Xue et al.*, 2012]:

$$\tau^* = \frac{k\overline{\rho_0}}{2N}\left[(c-U)^2 - \frac{f^2}{k^2}\right]^{\frac{1}{2}}(c-U)^2$$

The acceleration rate within a saturated region for IGW [*Xue et al.*, 2012]:

$$\frac{\partial U}{\partial t} = -\epsilon\frac{1}{\overline{\rho_0}}\frac{\partial \tau^*}{\partial z} = \epsilon\frac{k\left[(c-U)^2 - \frac{f^2}{k^2}\right]^{\frac{1}{2}}(c-U)^2}{2NH}$$

$\overline{\rho_0}$, ϵ, H are the atmospheric density, efficiency factor and scale height, respectively

The wave components of the newly added IGWs are specified by phase velocity from –20 to 20 m/s with a uniform spacing of 2 m/s. The momentum fluxes are assumed to be uniform across these components. These GWs are launched uniformly at the chosen latitude range at model level 200 hPa with an initial momentum flux τ= 0.001 Pa for each spectral element. The efficiency factor is used to adjust the magnitude of gravity wave forcing in WACCM. Through numerical experiments, we found that the differences between the WACCM simulated temperature climatology and ERA-40 are smallest using an efficient factor of 0.05 for SC-WACCM and 0.1 for interactive chemistry WACCM. These efficient factors will be used in all the IGW gravity wave scheme of current study (30ºS to 90ºS and 30ºN to 90ºN).

4.4 Experiments Setup in WACCM

As mentioned earlier, the IGW scheme is now applied to all latitudes, while the original internal gravity wave scheme in WACCM is kept the same. We designed WACCM simulation experiments aimed to study the effects of the new IGW scheme we proposed.

In the standard WACCM configuration, the chemistry is included interactively during simulation. WACCM does provide the option to specify the chemistry to replace the interactive chemistry (SC-WACCM). In SC-WACCM configuration, the heating rates are prescribed. We will use SC-WACCM first to isolate the dynamic effects of the new IGW scheme. WACCM simulations with interactive chemistry will also be performed and compared with the SC-WACCM results.

The experiments include 4 SC-WACCM simulations and 4 interactive chemistry WACCM simulations. The 4 SC-WACCM simulations are named cases 1 – 4 respectively. In case 1, the original GW scheme is used (without inertial gravity waves) and the imposed QBO at equatorial region is turned off. In case 2, the gravity wave scheme in *Xue et al.,* [2012] (IGW launched between 30^{o} S to 30^{o} N) is added. In case 3, additional IGWs are launched from 30^{o} S to 90^{o} S, and in case 4, additional the IGWs are launched globally. For case 1, case 3 and case 4, 10 years simulations are used to form the climatology of zonal mean wind and temperature in order to remove the inter-annual variations in simulation. For case 2, only 3 years simulations are used, since it is mainly used to rule out the effects of equatorial IGW on the cold bias.

The 4 interactive chemistry WACCM simulations are named cases 5 – 8. Similar to Cases 1 – 4, Cases 5–8 are simulated using interactive chemistry WACCM with originally GW scheme, Xue's scheme at equatorial region, IGW scheme in the southern hemisphere and IGW scheme in both southern and northern hemisphere respectively.

4.5 WACCM Specified Chemistry Simulations and the Effects of New GW Scheme

Temperature from SC-WACCM simulation and ERA-40 are compared in Figure 4.1. The monthly mean temperature of 10 years SC-WACCM simulations and 40 years ERA-40 are

averaged to form the temperature climatology. The difference of temperature climatology between SC-WACCM and ERA-40 are averaged from 70ºS to 90ºS and the results are displayed in Figure 4.1. ERA-40 does not have data above 0.1 hPa, so the contour of temperature difference is only available from 1000 hPa to 0.1 hPa. Figures 4.1a–d represents the temperature differences between cases 1–4 and ERA-40, respectively. According to Figure 4.1a, it is clear that SC-WACCM simulated temperatures from 10 hPa to 1 hPa are colder than ERA-40 during winter in the southern polar region when the original GW scheme is used. The cold bias in SC-WACCM begins in April and reaches a maximum of about 20 K in late June. In October, the cold bias in SC-WACCM begins to descend to lower altitudes and no clear cold bias is observed in November and December. These results demonstrate the cold pole bias in SC-WACCM simulation using the original GW scheme during winter and spring at the southern polar region. Displayed in Figure 4.1b are the temperature differences between simulation in case 2 and ERA-40. When Xue's GW scheme are used in the equatorial region, the QBO in the equatorial region can be produced internally [*Xue et al.,* 2012], but a cold bias up to 20 K still exists in the southern polar region from May to October. The result indicates that the IGWs launched in the equatorial region have almost no effect on the temperature bias in the southern polar region. The missing gravity wave forcing in the equatorial region are not the reason of the cold pole bias in SC-WACCM.

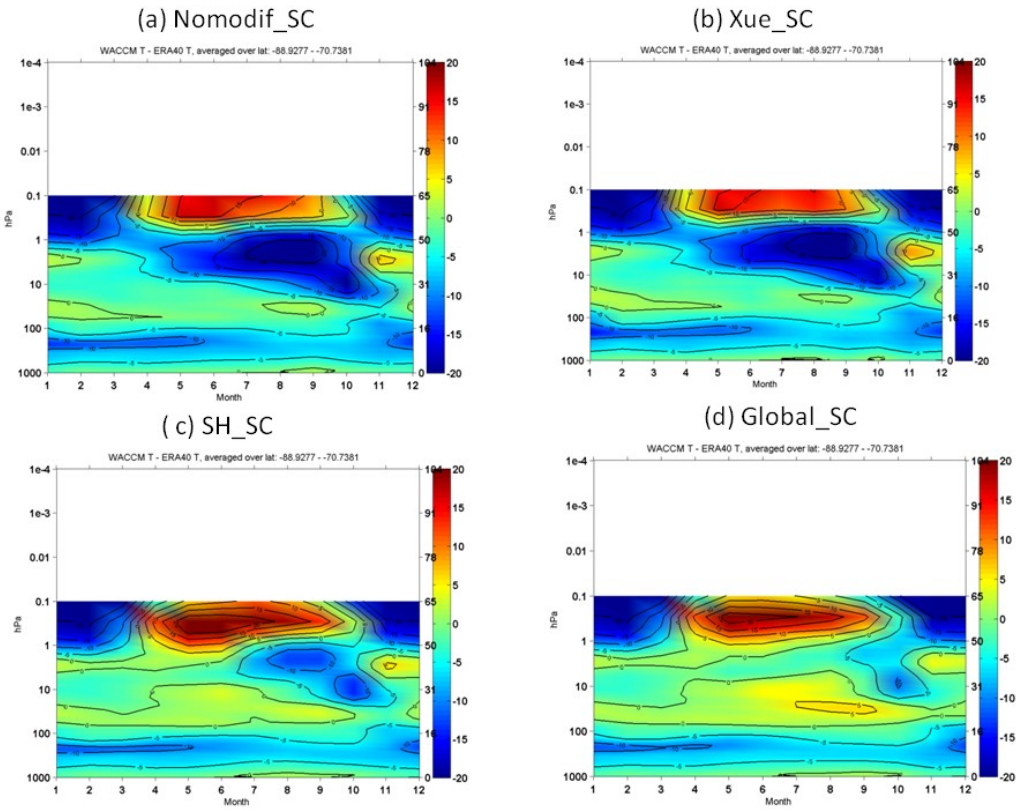

Figure 4.1: Temperature difference between specified chemistry WACCM simulation and ERA-40 averaged from 70ºS to 90ºS. The gravity wave parameterization used in the WACCM simulation are (a) original mesoscale gravity wave scheme, (b) inertial gravity wave launched in the equatorial region, (c) inertial gravity wave launched in southern hemisphere, and (d) inertial gravity wave launched in both hemispheres.

The differences between the simulated temperatures in case 3 with new IGW scheme at the southern hemisphere and ERA-40 are displayed in Figure 4.1c. When the new IGWs are launched in the southern hemisphere in case 3, the simulated temperature is 15-20 K higher than case 1 between 10 hPa and 1 hPa from April to October and the cold bias are reduced. It is thus evident that the parameterized IGWs forcing in the southern hemisphere from 30S to 90S are able to reduce the cold bias in SC-WACCM. The effects of including inertial gravity waves in both hemispheres are examined in case 4, with IGWs launched from 30S to 90S and from 30N to

90N. The temperature difference between case 4 and ERA-40 is displayed in Figure 4.1d. In case 4, the cold bias between 10 hPa and 1 hPa from April to October are significantly reduced, ~15K smaller than case 1. Figures 4.1c and 1d indicate that the simulation results of case 3 and case 4 are similar. The temperature bias is reduced by approximately the same amount for both cases. The inertial gravity waves launched in the northern hemisphere have little effects on the simulated winter temperature bias in the southern polar region.

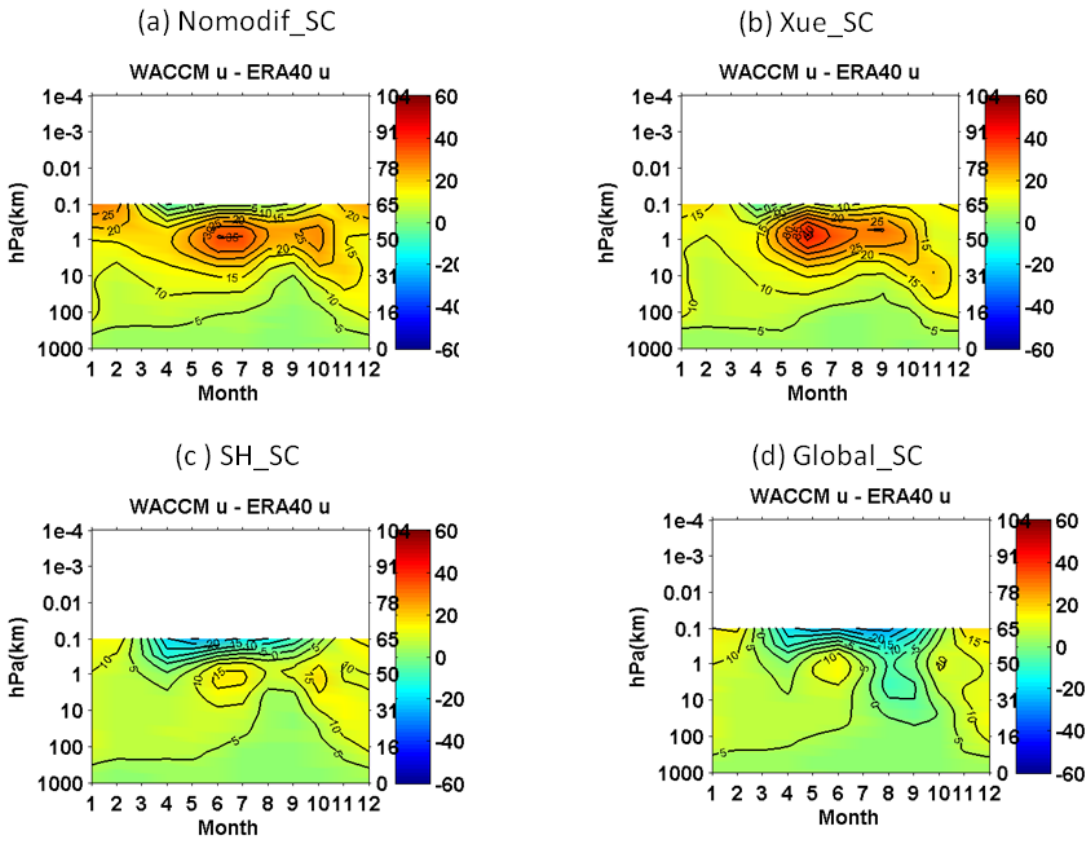

Figure 4.2: Zonal wind difference between specified chemistry WACCM simulation and ERA-40 averaged 50ºS to 70ºS. The gravity wave parameterization used in the simulation are original gravity wave (a), inertial gravity wave launched at equatorial region (b), inertial gravity wave launched at southern hemisphere (c) and inertial gravity wave launched at both hemispheres (d)

The new IGW scheme reduces the cold bias mainly through modifying the zonal wind and meridional circulation in simulation. In the new scheme, additional IGW waves mean more westward wave forcing at lower altitudes during winter in the southern hemisphere. The additional westward wave forcing decelerates the eastward zonal wind. Due to Coriolis effects, the westward forcing enhances the poleward meridional circulation and thus enhances downwelling and adiabatic warming in the southern polar stratosphere. Zonal wind simulations of SC-WACCM using different gravity wave parameterizations are compared with ERA-40 in Figure 4.2. The monthly mean zonal wind of WACCM simulations are averaged from 50° S to 70 ° S for each pressure level. The zonal wind of ERA-40 is averaged using the same method for the same latitude range. The difference of WACCM monthly mean zonal wind and ERA-40 monthly mean zonal wind are calculated using the averaged wind climatology. The latitude range 50° S to 70° S in Figure 4.2 is chosen because this is where the maximum jet in the southern polar region is located during winter. As displayed in Figure 4.2a, the simulated wind between 10 hPa and 0.1 hPa is 35 m/s larger than ERA-40 from April to December in case 1. In case 2, when Xue's scheme is used in the equatorial region from 30° S to 30° N, the jet in the southern polar region during September and October are almost the same as case 1. This result again confirms that the IGWs launched in the equatorial region have little effects on the bias of SC-WACCM simulation. In case 3, when the IGWs are launched in the southern hemisphere from 30° S to 90° S, the zonal wind difference between SC-WACCM and ERA-40 is significantly reduced from 20–35 m/s to 5–15 m/s in the southern hemisphere between 10 hPa and 0.1 hPa from April to October. In case 4, when the IGWs are launched in both hemispheres from 30S to 90S and 30N to 90N, the simulated zonal winds are similar to the simulated zonal winds in case 3. These results show that

the IGWs launched in the northern hemisphere have little effects on the wind climatology of the southern hemisphere, which is corresponding to the results of simulated temperature in the southern polar region.

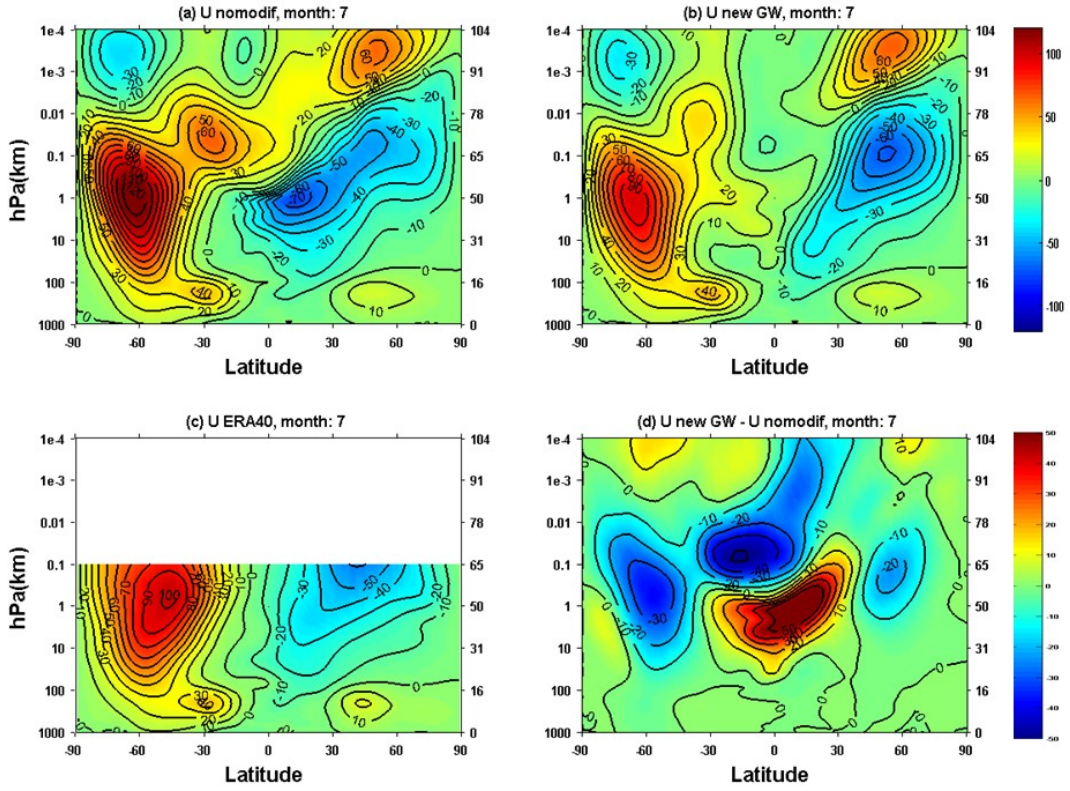

Figure 4.3: Monthly mean zonal wind climatology of July. The specified chemistry WACCM simulated zonal wind using original gravity wave scheme (a), inertial gravity wave at both hemisphere (b), the zonal wind from ERA-40 (c) and zonal wind from inertial GW scheme minus zonal wind from original GW scheme (d) are displayed.

To illustrate the modification of zonal wind at different latitudes, we plotted the zonal wind climatology in pressure versus latitude contours every month (only July and November are shown here for winter and spring time). The monthly zonal wind climatology of all the other

months can be found in the appendix at the end of this thesis. Monthly mean zonal wind climatology from SC-WACCM simulations during July and November are displayed in Figure 4.3 and Figure 4.4 respectively. During winter, the maximum simulated jet speeds in the southern hemisphere using the original GW scheme (case 1) are about 120 m/s, 20 m/s larger than the maximum jet speed of ERA-40, according to Figure 4.3(a) and (c). When the IGWs are launched from 30^{o} S to 90^{o} S and from 30^{o} N to 90^{o} N, the maximum jet speed in the southern hemisphere is 90 m/s, reduced by 30 m/s comparing to case 1. At the same time, the westward wind in the northern/summer stratopause and mesosphere increases around 60^{o} N with the IGW forcing, which seems to improve the wind climatology according to ERA-40 (Figure 4.3(c)). Similar wind changes are see over all the winter month from June to October.

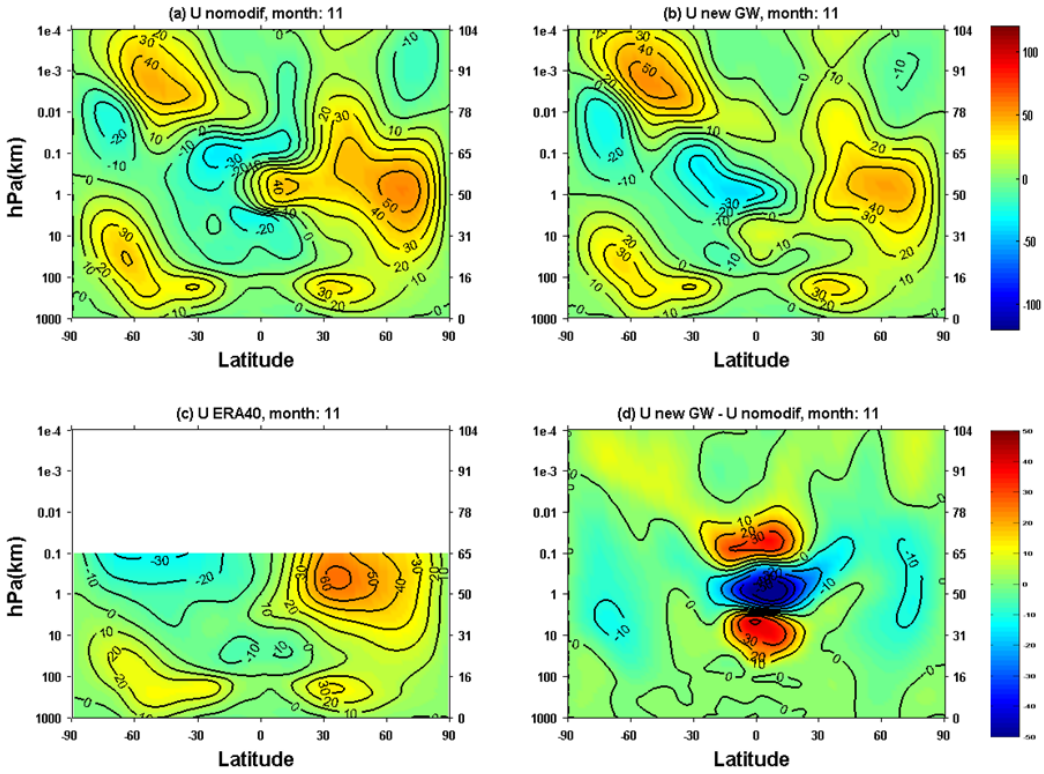

Figure 4.4: Similar to Figure 4.3, but display the monthly mean zonal wind of November.

During spring, as showed in Figure 4.4, the simulated zonal wind between 10 hPa ad 100 hPa at 60ºS is about 40 m/s, 20 m/s faster than ERA-40. With the new IGW scheme, the simulated zonal wind is reduced to 30 m/s, though still faster than ERA-40. Moreover, the simulated wind reversal level during spring is improved by the new IGW scheme. In Figures 4.4(a), the simulated wind reversal level near the South Pole is about 0.5 hPa in November, 0.5 hPa higher than ERA-40. When the IGWs are launched, this wind reversal level decrease to about 1 hPa as displayed in Figure 4.4(b), which is the same as the wind reversal level observed in ERA-40. The wind climatology of November is chosen as a demonstration representing the southern spring. During December, the deceleration of wind is similar to November. The wind

reversal level during December is about 2 hPa with original GW scheme and about 4 hPa with new IGW scheme. New IGW scheme is making the wind reversal level lower during December.

According to the results discussed above, the zonal wind climatology is in better agreement with observation in the southern hemisphere with the new IGW scheme. Now we discussed the zonal wind climatology in the northern hemisphere with the new IGW scheme. In the northern hemisphere, comparing to case 1, the westward zonal wind climatology in case 3 has been modified by the new IGW scheme, as displayed in Figure 4.3. In case 1, the westward wind (blue area) has a speed up to 70 m/s within 0^{o} N-30^{o} N and 10 hPa-1 hPa, and westward wind up to 50 m/s within 30^{o} N-60^{o} N and 1 hPa-0.01 hPa. In case 3, the maximum of the westward wind shifts to 30^{o} N-60^{o} N and 1 hPa-0.01 hPa with a speed up to 60 m/s. Comparing to ERA-40, the simulated westward wind climatology of case 3 corresponds to ERA-40 better than case 1. Therefore we conclude that the new IGW scheme is able to improve the zonal wind climatology in the northern hemisphere during winter.

The zonal wind change induced by the IGW scheme can be quantified through the zonal wind difference with and without the IGW scheme. Simulated zonal winds using the new IGW scheme minus simulated zonal winds using the original GW scheme in SC-WACCM are calculated and plotted in Figure 4.3(d) and Figure 4.4(d). The blue areas and red areas represent the westward zonal wind increase and eastward zonal wind increase induced by new IGW scheme correspondingly. The zonal wind changes from 30ºS to 30ºN are induced by forcing from Xue's scheme and they are not the topic of the current study. The new IGWs are launched from 30ºS to 90ºS and from 30ºN to 90ºN and they propagate vertically. Therefore the new IGWs are responsible for the deceleration or acceleration above 30ºS or above 30ºN. During austral winter month such as July in Figure 4.3(d), this new IGW scheme mainly induce decelerations up to 30

m/s from 40ºS to 80ºS and from 10 hPa to 0.01 hPa. The change induced in the northern hemisphere is much smaller both in speed and area. One possible reason is that the southern hemisphere is mainly ocean and the continents are mainly in the northern hemisphere. The continents produce orographic gravity waves which slow down the zonal wind. In the southern hemisphere, the orographic gravity waves are small and this lead to higher zonal wind in the southern hemisphere. The acceleration (or deceleration) of the zonal wind due to wave breaking is proportional to $(\bar{u} - c)^3$, c is the phase speed and u is the zonal wind [*Lindzen* 1981]. According to the equation, the effects of the inertial gravity wave scheme in the southern hemisphere are larger than the northern hemisphere. Therefore this IGW scheme has the advantage of improving the cold pole bias in the southern hemisphere while does not significantly change the state in the northern hemisphere (actually there are signs of further improvement). This may relieve the concern that WACCM simulation in the northern hemisphere may deteriorate when the cold pole bias is reduced in the southern hemisphere.

Compare the decelerations in July and November displayed in Figure 4.3(d) and Figure 4.4(d), the decelerations induced by the new IGW scheme in spring are much smaller than in winter. In November, as displayed in Figure 4.4(d), the deceleration in the southern hemisphere above 30^o S is 10 m/s, much smaller than the 30 m/s deceleration in July, while the two months use the same efficient factor thus have the same IGW magnitude. For lack of any physical constraint, the same efficient factor is used for every month, and as a result the bias in some months may be overcompensated while in other months it is undercompensated.

In summary, using SC-WACCM numerical experiments we demontrate that the IGWs launched from mid to high latitudes are able to reduce the zonal wind and increase the temperature in the southern polar stratosphere during winter, thus reducing the cold pole bias.

The wind reversal level is lower in November using new IGW scheme too. Through choosing an appropriate efficiency factor, both the simulated wind and stratosphere temperature in the southern hemisphere during the winter and spring are in better agreement with ERA-40. Since we use the specified chemistry version of WACCM, the cold bias is reduced by this new IGW scheme through dynamic effects.

4.6 WACCM Interactive Chemistry Simulations and the Effects of New GW Scheme

In this section, we will test the capability of IGW scheme in reducing the cold pole bias when the atmosphere chemistry is included interactively in the simulation. To facilitate better comparison, the simulation results of cases 5 – 8 are displayed using the same method as the previous section.

Figure 4.5 and Figure 4.6 display the temperature and wind differences between case 5 – 8 and ERA-40 respectively. In Figure 4.5a and 4.5b, the cold bias up to 20 K exists at 10–1 hPa from May to September and this is similar to the SC-WACCM. Starts from October, the cold bias in the interactive chemistry WACCM simulation continues at progressively lower levels (from 10–1 hPa to 100–10 hPa), which is not observed in the SC-WACCM. This is probably because the version of SC-WACCM used in this study employs ozone heating from a CAM-CHEM simulation, where the ozone hole is very weak. According to Figure 4.5c and 4.5d, the new IGW scheme is able to reduce the simulated temperature bias from May to October between 10 hPa and 1hPa and from November to March between 200 hPa and 10 hPa. But the temperature increases induced by IGW scheme during winter from April to October are much larger than spring from November to December.

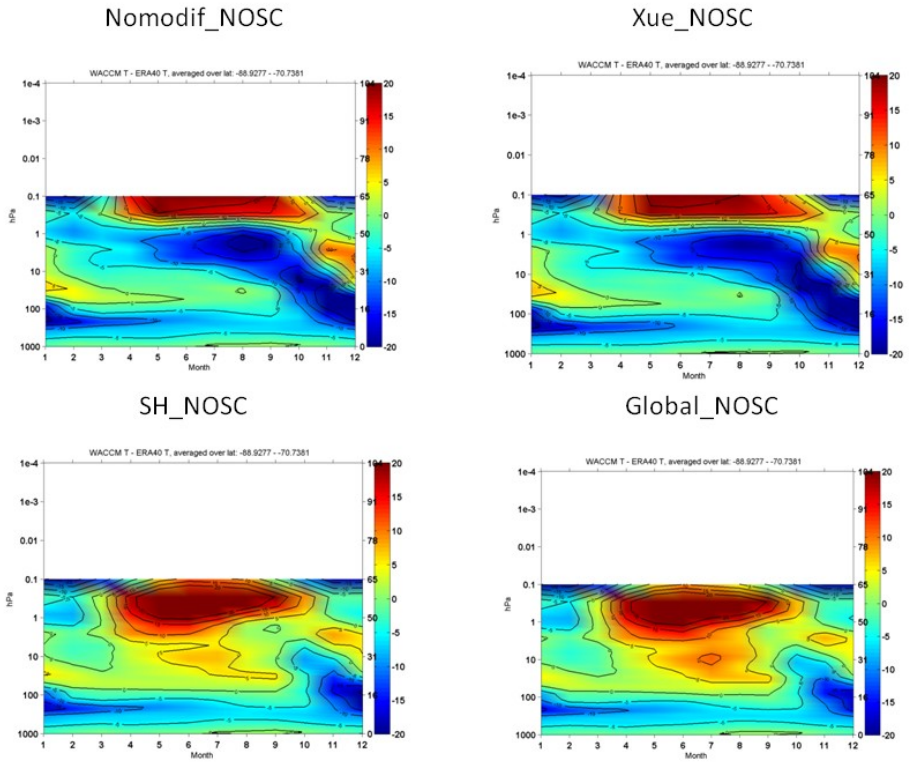

Figure 4.5: Similar to Figure 4.1, but the interactive chemistry WACCM simulation is used to calculate the difference.

Figure 4.6a–d displays the wind difference between cases 5–8 and ERA-40, respectively. In Figure 4.6a and 4.6b, the wind difference between the interactive chemistry WACCM and ERA-40 from April to October is 20 – 40 m/s, which is similar to the SC-WACCM. Starting from October, the regions of large difference in the interactive chemistry WACCM extend to lower altitude, from 10 hPa to 100 hPa. During November and December, the interactive chemistry WACCM simulated winds are stronger than observations by up to 30 m/s from 100 to 0.1 hPa. The regions of large zonal wind bias correspond to regions of large temperature bias. According to Figure 4.6c and 4.6d, inertial gravity wave scheme is able to reduce the zonal wind bias in simulation throughout the year. Similar to the improvement of temperature bias, the zonal

wind decelerations induced by IGW scheme are much larger during winter from April to October than the spring from November to March.

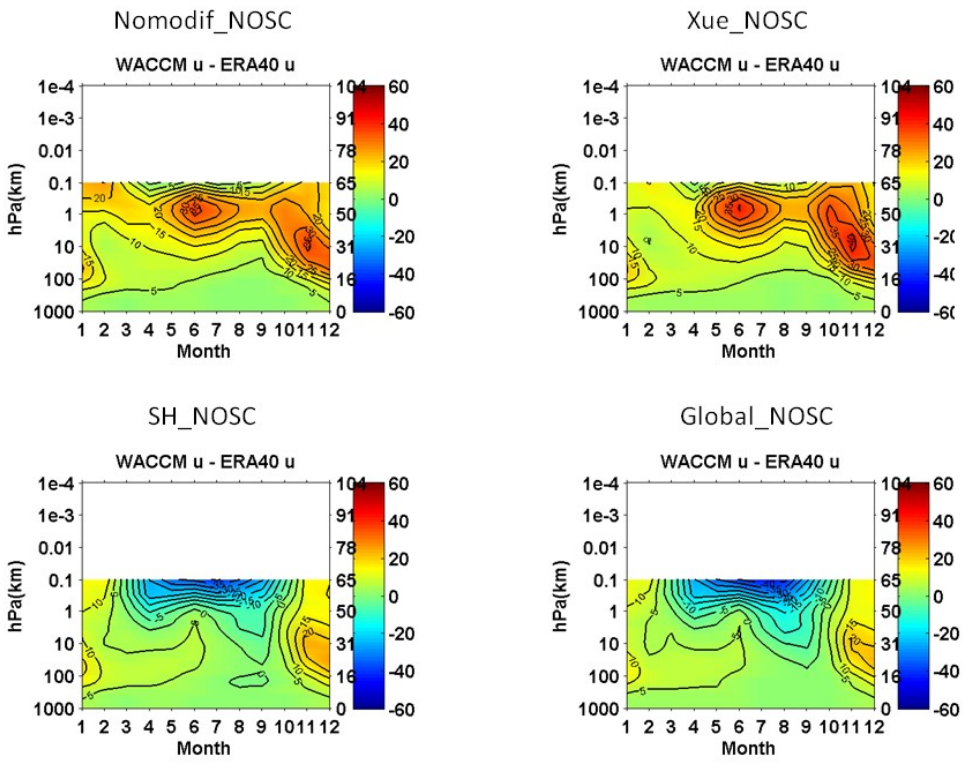

Figure 4.6: Similar to Figure 4.2, but the interactive chemistry WACCM simulation is used to calculate the difference.

Figure 4.7 and Figure 4.8 are similar to Figure 4.3 and Figure 4.4, but the zonal wind climatology displayed is from interactive chemistry WACCM simulation. The maximum simulated zonal wind speed in the southern hemisphere during July using original GW scheme is about 120 m/s (Figure 4.7a), which is 20 m/s higher than ERA-40 (Figure 4.7c). When the IGW scheme is used, the simulated zonal wind speed is decelerated to 80 m/s (Figure 4.7b) which is

20 m/s lower than ERA-40. Under current IGW scheme, the zonal wind bias during winter is overcompensated by 20 m/s. In November, the maximum simulated zonal wind speed with original GW scheme in the southern hemisphere is 60 m/s (Figure 4.8a), which is 40 m/s higher than ERA-40 (Figure 4.8c). When the IGW scheme is used, this wind speed is decelerated to 40 m/s, still higher than ERA-40 but the difference has been reduced. The zonal wind bias during spring is undercompensated by 10 m/s. Moreover, the simulated wind reversal level at the polar region with original GW scheme is about 0.2 hPa. When the IGW scheme is used, the wind reversal is decreased to 0.9 hPa, very close to the 1 hPa wind reversal level observed in ERA-40.

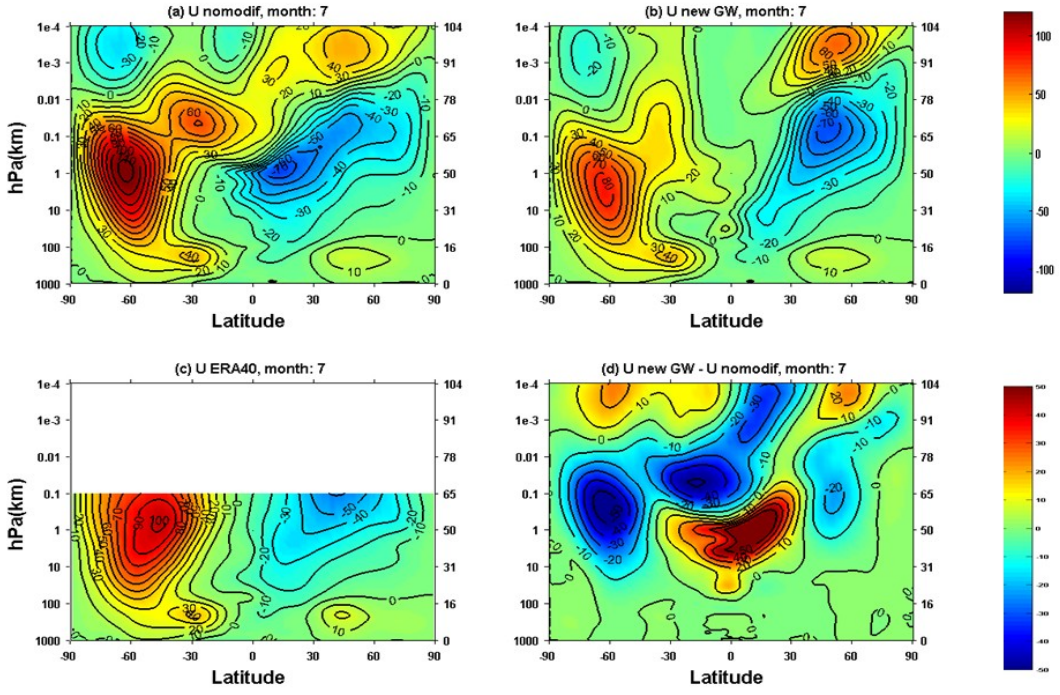

Figure 4.7: Monthly mean zonal wind climatology of July. The interactive chemistry WACCM simulated zonal wind using original gravity wave scheme (a), inertial gravity wave at both hemisphere (b), the zonal wind from ERA-40 (c) and zonal wind from inertial GW scheme minus zonal wind from original GW scheme (d) are displayed.

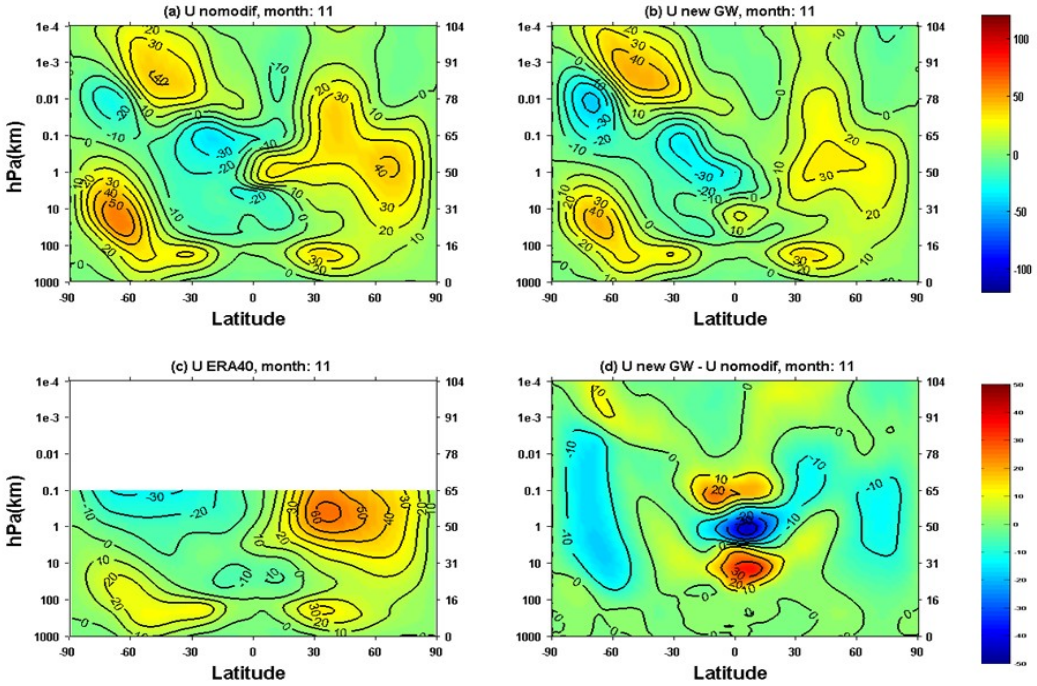

Figure 4.8: Similar to Figure 4.7, but display the monthly mean zonal wind of November.

In WACCM simulations with interactive chemistry, it is found that the efficiency factor needs to be increased to 0.1, to achieve better agreement with ERA-40. This is probably because the ozone hole is weaker and ozone heating is larger in SC-WACCM, as mentioned earlier.

Even though the IGW is launched with the same magnitude for all the months, the IGW induced zonal wind deceleration effects during winter is 30 m/s larger than spring, probably due to differences in background wind and the wave breaking altitudes. In Figure 4.7d and 4.8d, the maximum zonal wind deceleration in the southern hemisphere is about 50 m/s during July and 20 m/s during November. For the amplitude of IGW used in current study, the wind climatology during winter is overcompensated while the wind climatology during spring is undercompensated. In spite of these differences, our numerical model results demonstrate that

IGW is a viable candidate for providing the missing forcing to reduce the cold pole bias.

4.7 Wave Forcing Analysis

When the IGWs are launched in the middle-high latitudes, the zonal wind and meridional circulation are modified. This will change the propagation and filtering condition for atmosphere waves and can affect the breakings of the internal gravity waves in the mesosphere. The change of resolved wave forcing and internal gravity wave forcing may cancel or enhance the effects of IGW forcing we added. In order to thoroughly understand the effects induced by IGWs, the change of resolved wave forcing, internal gravity wave forcing and inertial gravity wave forcing will be analyzed in this section.

The temperature difference, total wave forcing difference, zonal wind difference, GW forcing difference, O3 mixing ratio difference and IGW forcing difference between the simulation with and without the new IGW scheme are displayed in Figure 4.9. The total wave forcing includes internal gravity wave forcing, inertial gravity wave forcing and resolved wave forcing. GW forcing includes both the internal gravity wave forcing and inertial gravity wave forcing.

According to Figure 4.9b and 4.9d, total wave forcing difference is almost the same as the GW forcing difference above 0.1 hPa. Most of the total wave forcing change is induced by the gravity wave. The change of resolved wave forcing above 0.1 hPa is small, probably because the resolved wave forcing is mainly by large-scale planetary waves which dominate in the stratosphere. Figure 4.9f shows the forcing of IGWs launched in the southern hemisphere. The IGWs mainly break around 0.1 hPa, and exert an net westward forcing on the mean flow. The GW forcing change in Figure 4.9d show maximum westward forcing around 0.1 hPa, but the magnitude of GW forcing change is smaller than the IGW forcing we added. Therefore, the IGW

forcing is partially cancelled out by the increase of eastward forcing by internal gravity wave breaking. This is also clear around and above 0.01 hPa in Figure 4.9d: while the IGW forcing is weakly westward the GW forcing difference is eastward and larger than 30 m/s/day. The IGWs launched decelerate the eastward zonal wind in the stratosphere during winter, this change the filter condition of internal GW and more eastward internal GW is able to propagate to the mesosphere. The increases of eastward internal gravity wave forcing is stronger than the increase of westward inertial gravity wave forcing in the mesosphere, so that the net effects of GW forcing change is eastward.

The westward total wave forcing around 0.1 hPa decelerates the eastward zonal wind around 0.1 hPa while the eastward total wave forcing accelerates the eastward zonal wind in the mesosphere and lower thermosphere above 0.01 hPa. The change of zonal wind discussed above is displayed in Figure 4.9c. The westward forcing at 0.1 hPa in turn enhances the poleward meridional circulation, the downwelling, and thus adiabatic heating in the southern winter polar region. For the same reason, the eastward forcing above 0.01 hPa decrease the temperature in the mesosphere and lower thermosphere. As showed in Figure 4.9a, the temperature is increased in the southern stratosphere and is decreased in the southern mesosphere and lower thermosphere during winter.

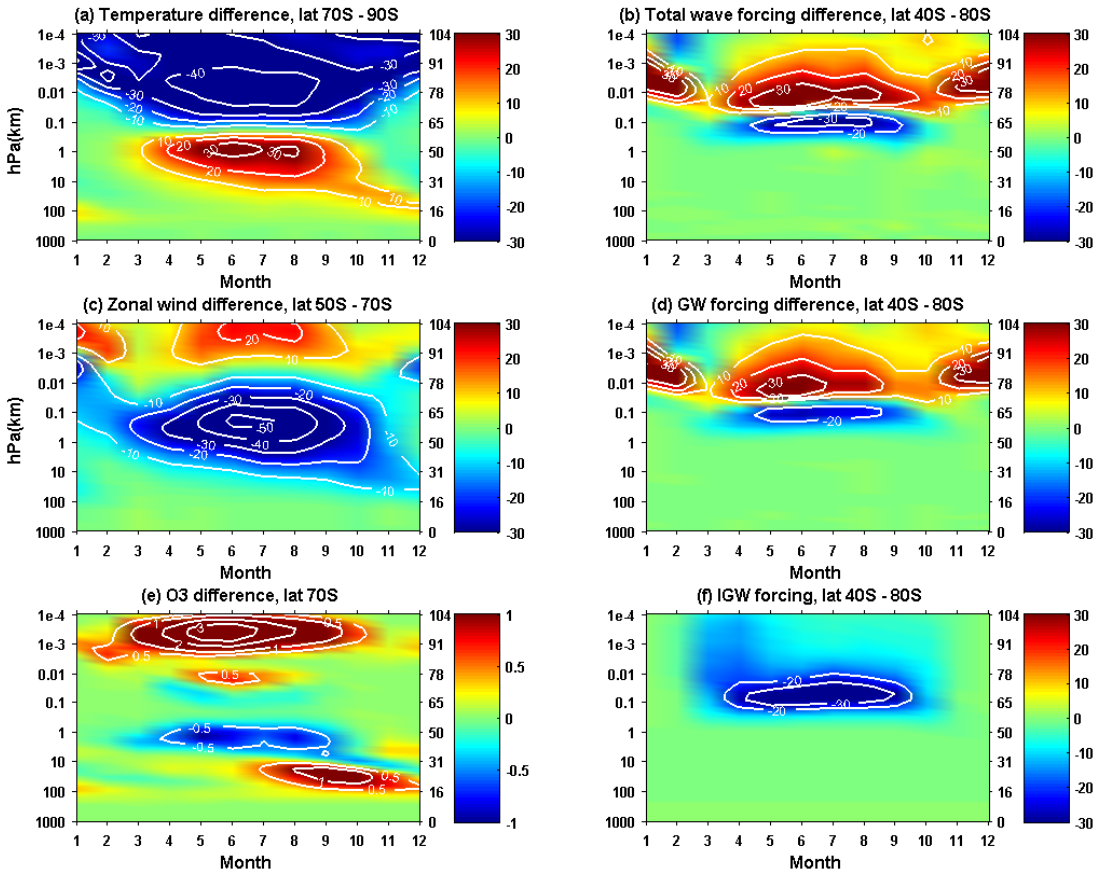

Figure 4.9: The difference of temperature (a), total wave forcing (b), zonal wind (c), GW forcing (d), O3 mixing ratio (e) and IGW forcing (f) with IGW scheme and without IGW scheme are displayed. Simulation with IGW scheme minus simulation without IGW scheme equals the difference. The unit for temperature, wave forcing, zonal wind and O3 are K, m/s/day, m/s and ppmv respectively.

The wave forcing in the mesosphere and lower thermosphere in Figure 4.9 is much stronger than stratosphere because the density of atmosphere at high altitudes is small therefore the deceleration or acceleration effect is much bigger. The wave forcing in the stratosphere in Figure 4.9 is obscured using the color bar -30 to 30 m/s/day. In Figure 4.10 we only display the forcing up to 0.1 hPa and use a much smaller color bar range from -1 m/s/day to 1 m/s/day. Comparing Figure 4.10b and 4.10d, GW wave forcing contributes most of the wave forcing change above 1 hPa. Below 1 hPa, GW forcing has almost no change with and without IGWs

and the resolved wave forcing begins to dominate the total wave forcing change. The cold pole bias is believed to be caused by the missing wave forcing in the stratosphere. With addition IGWs launched in middle to high latitudes, and using the wave parameters mentioned earlier, the IGW forcing is found in the upper stratosphere (and higher). The temperature increase, however, extends over the whole stratosphere from 100 hPa to 0.1 hPa as displayed in Figure 4.10a. This is likely because the westward gravity wave forcing enhances the adiabatic warming below, even though the direct forcing at lower altitude is weak or none. This is the 'downward' control' principle which is discussed in *Garcia and Boville* [1994].

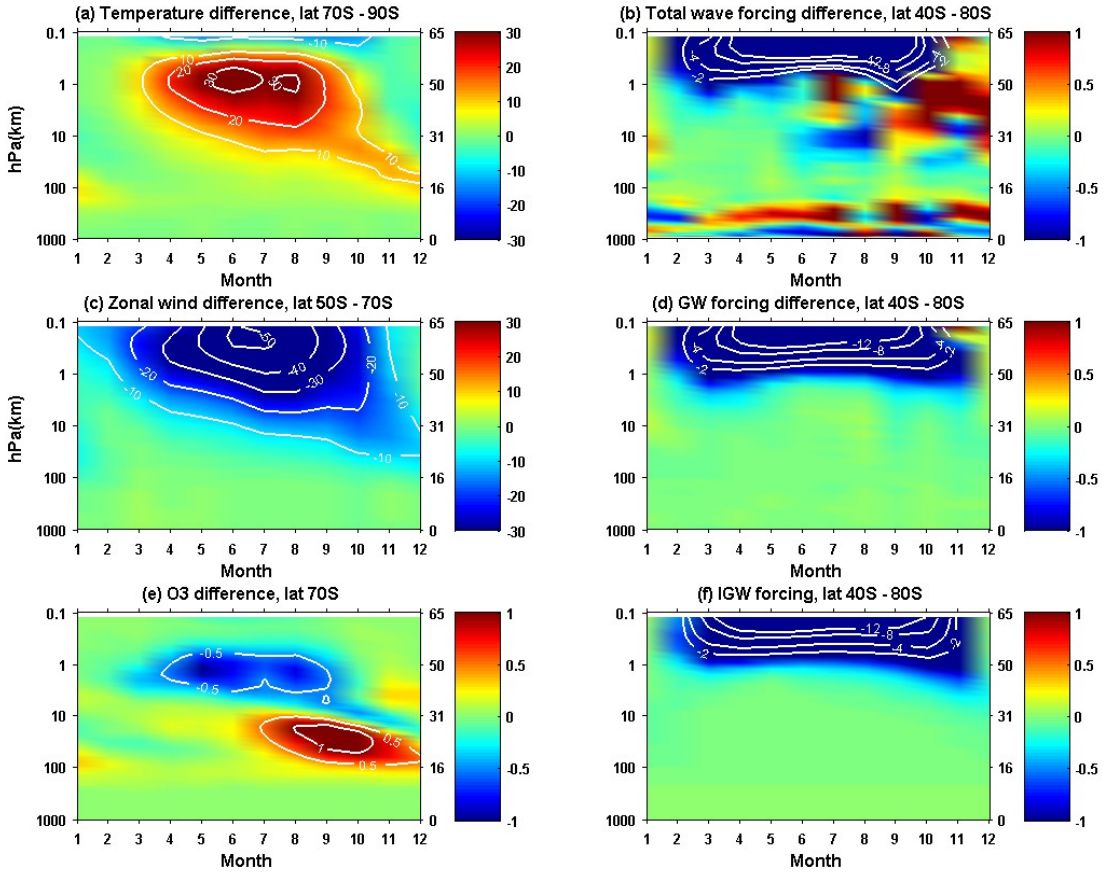

Figure 4.10: Similar to Figure 4.9, but only the differences below 0.1 hPa are displayed.

The latitudinal structures of the wave forcing for July and November are shown in Figure 4.11 to Figure 4.14. The monthly mean wave forcing of all other months can be found in the appendix at the end of this thesis.

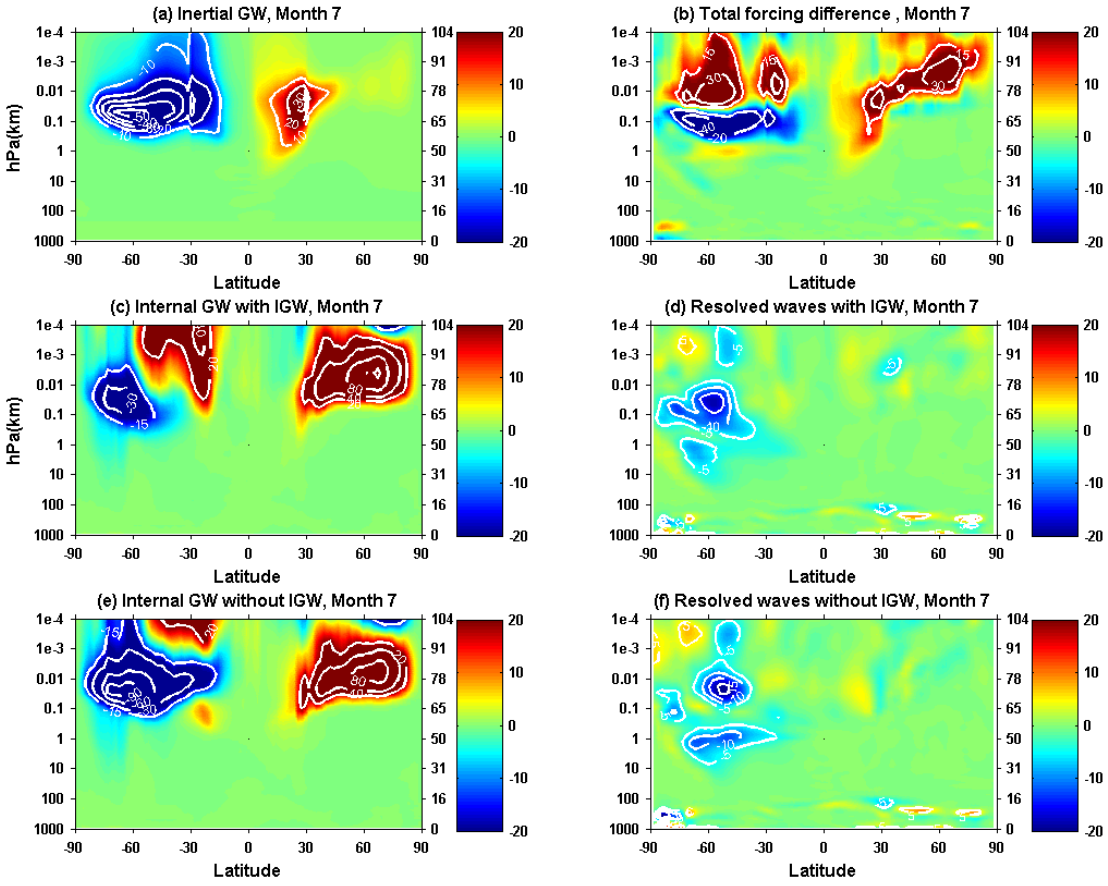

Figure 4.11: The inertial GW forcing (a), total wave forcing difference with and without IGW scheme (b), internal GW forcing with IGW (c), resolved wave forcing with IGW (d), internal GW forcing without IGW (e) and resolved wave forcing without IGW (f) are displayed. The units for forcing are m/s/day.

In Figure 4.11, the forcing by mesoscale GW and resolved waves with and without IGW scheme are showed to study the difference of wave forcing climatology induced by the new IGW scheme. Without IGW, the parameterized mesoscale gravity wave mainly breaks above 0.1 hPa. When the IGWs are parameterized, the westward internal gravity wave around 0.01 hPa is reduced, this partially cancels out the increase of westward wave forcing induced by IGWs. Above 0.01 hPa from 30^{o} S to 60^{o} S, the eastward internal wave forcing increases and cancels out the westward inertial gravity wave forcing. The additional IGWs thus causes an increase of eastward wave forcing in this region even though the IGWs forcing there is westward. The magnitude of the resolved wave forcing and the change of the resolved wave forcing are much smaller than the GW in the mesosphere. This confirms that GW is the main contributor in the change of total wave forcing above 0.1 hPa. The wave forcing differences are displayed in Figure 4.12. Comparing Figure 4.12b – c, it is clear that GW dominate the wave forcing difference above 1 hPa.

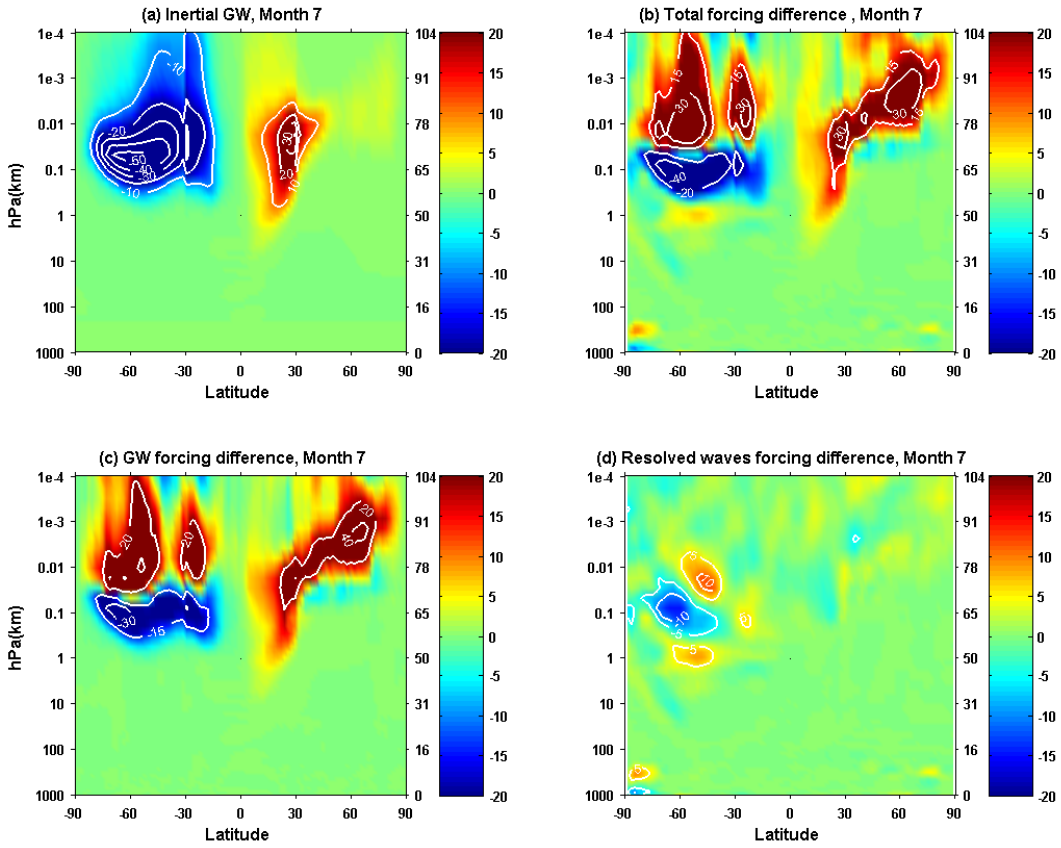

Figure 4.12: Wave forcing with IGW minus wave forcing without IGW equals the difference of wave forcing. The difference of IGW forcing (a), total wave forcing (b), GW forcing (c) and resolved waves forcing (d) are displayed. The unit is m/s/day.

The deceleration or acceleration rates due to wave forcing are one order smaller in the stratosphere comparing to mesosphere. In Figure 4.11 and Figure 4.12, the effects of wave forcing in the stratosphere are obscured with the color bar -20 to 20 m/s/day. To display the wave forcing clearly, the wave forcing in the stratosphere are plotted in Figure 4.13 and Figure 4.14 using a much smaller color bar -1 to 1 m/s/day. In Figure 4.13e, when the original GW parameterization is used in WACCM, the GW wave forcing has a gap around 60^{o} S, which is consistent with the GW forcing in CMAM [*McLandress et al,* 2011]. In *McLandress et al* [2011], they proposed to reduce the cold pole bias by using addition orographic gravity wave forcing at

60° S to fill this gap. Their GW scheme produces positive results and the cold pole bias is reduced. The IGW scheme we used in this study is different with their orographic gravity scheme at 60° S in *McLandress et al* [2011]. In Figure 4.13c, when the IGW scheme is implemented, there is still a wave forcing gap around 60° S. The IGW scheme used in this study didn't fill the wave forcing gap at 60° S. The IGWs we launched mainly breaks above 1 hPa and the maximum is around 0.1 hPa, which is higher than the 1 hPa GW breaking level of *McLandress et al* [2011]. The wave forcing differences are displayed in Figure 4.14. Below 0.1 hPa, the changes of total wave forcing induced by IGWs are dominated by changes of the resolved wave forcing. The gravity wave forcing is almost unchanged with or without the IGWs below 0.1 hPa according to Figure 4.14c. This is different with the GW scheme of *McLandress et al* [2011] because in their study, the change of GW forcing dominates the change of total wave forcing in the stratosphere, and the change of resolved wave forcing can be ignored. Regardless of these differences with the forcing in *McLandress et al* [2011], the cold pole bias is reduced in this study, and the temperature climatology, zonal wind climatology, wind reversal level and ozone mixing ratio show signs of improvement using the IGW scheme.

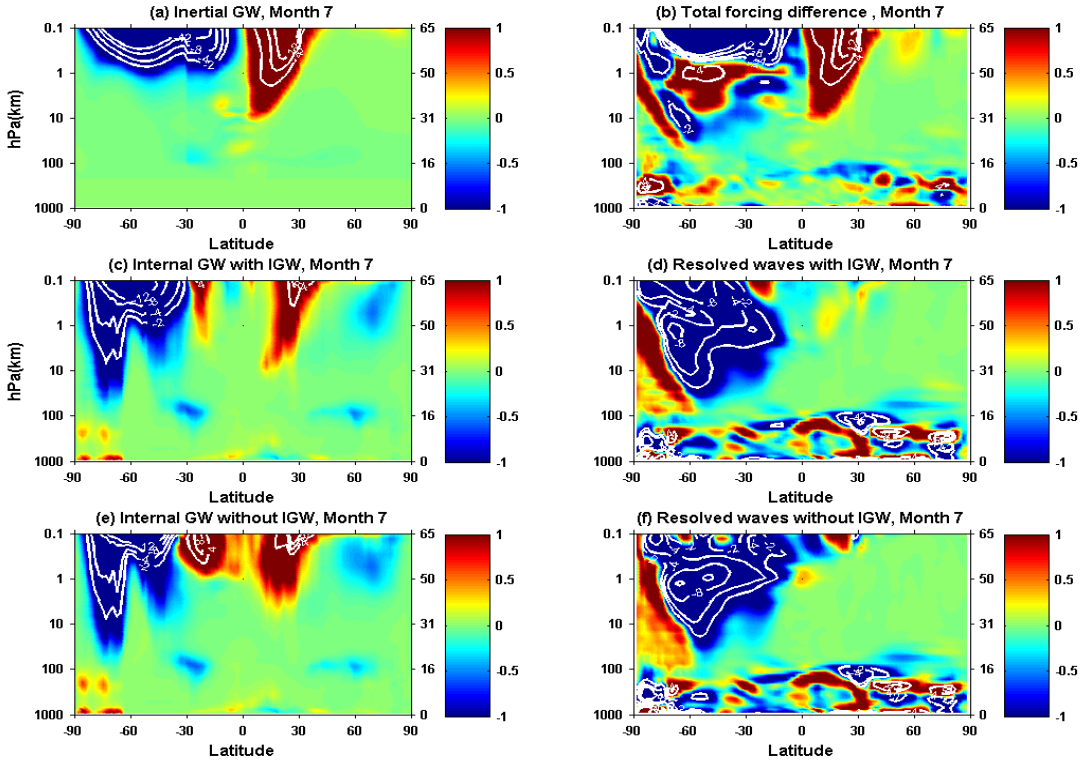

Figure 4.13: Similar to Figure 4.11, but only the wave forcing below 0.1 hPa is displayed. The unit is m/s/day

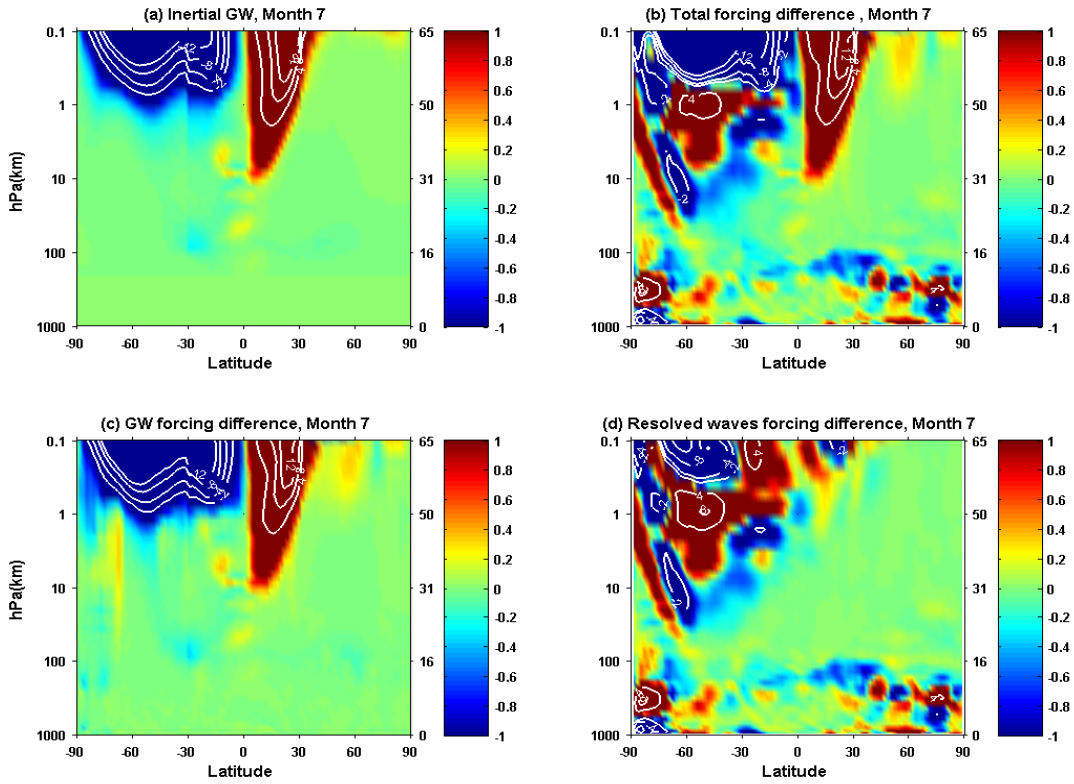

Figure 4.14: Similar to Figure 4.12, but only the wave forcing difference below 0.1 hPa is displayed. The unit is m/s/day.

Figure 4.15 and Figure 4.16 display the wave forcing and wave forcing difference of November. According to Figure 4.15a, the IGWs mainly break in the northern hemisphere during November. In the southern hemisphere, the magnitude of IGW forcing is an order of magnitude smaller than the northern hemisphere. But the mesoscale wave forcing in the southern hemisphere is still modified and the GW wave forcing differences in the southern hemisphere in Figure 4.16c are comparable to the northern hemisphere.

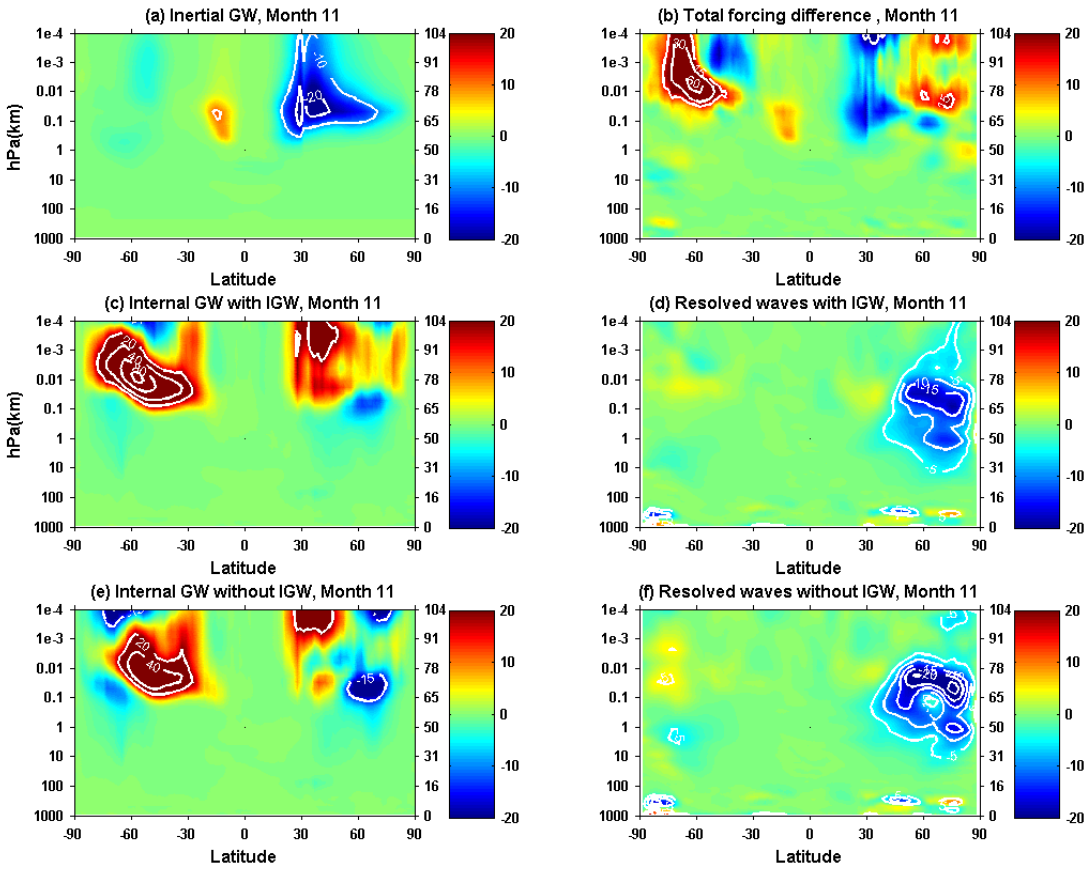

Figure 4.15: Similar to Figure 4.11, but for November

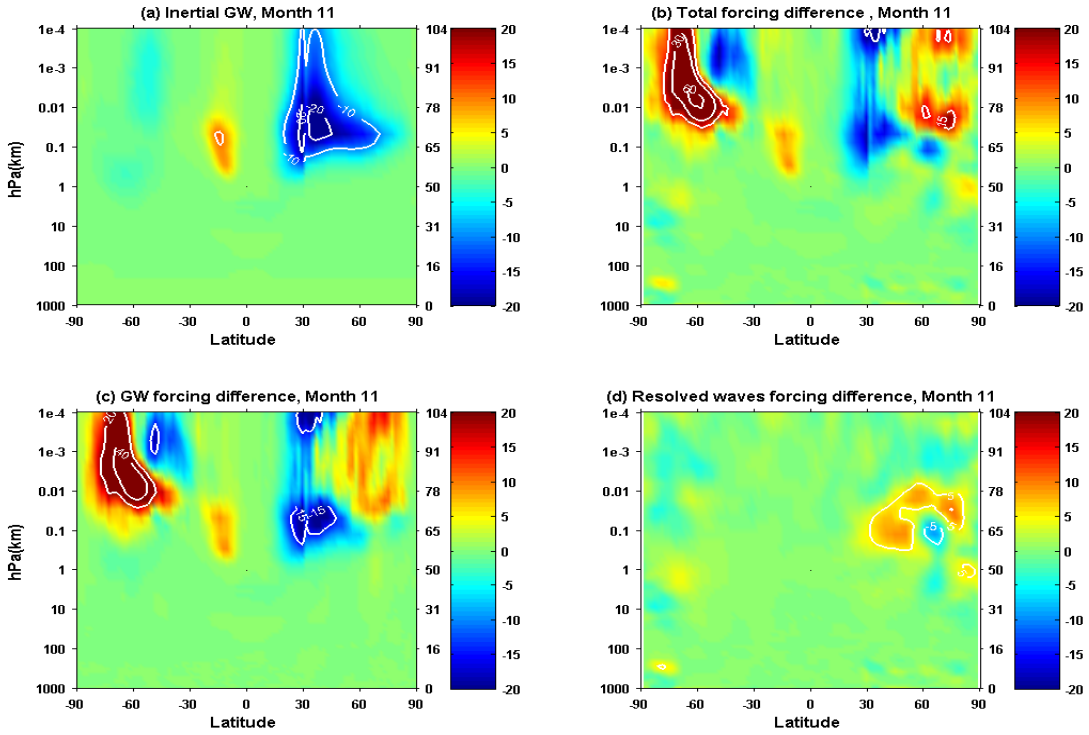

Figure 4.16: Similar to Figure 4.12, but for November

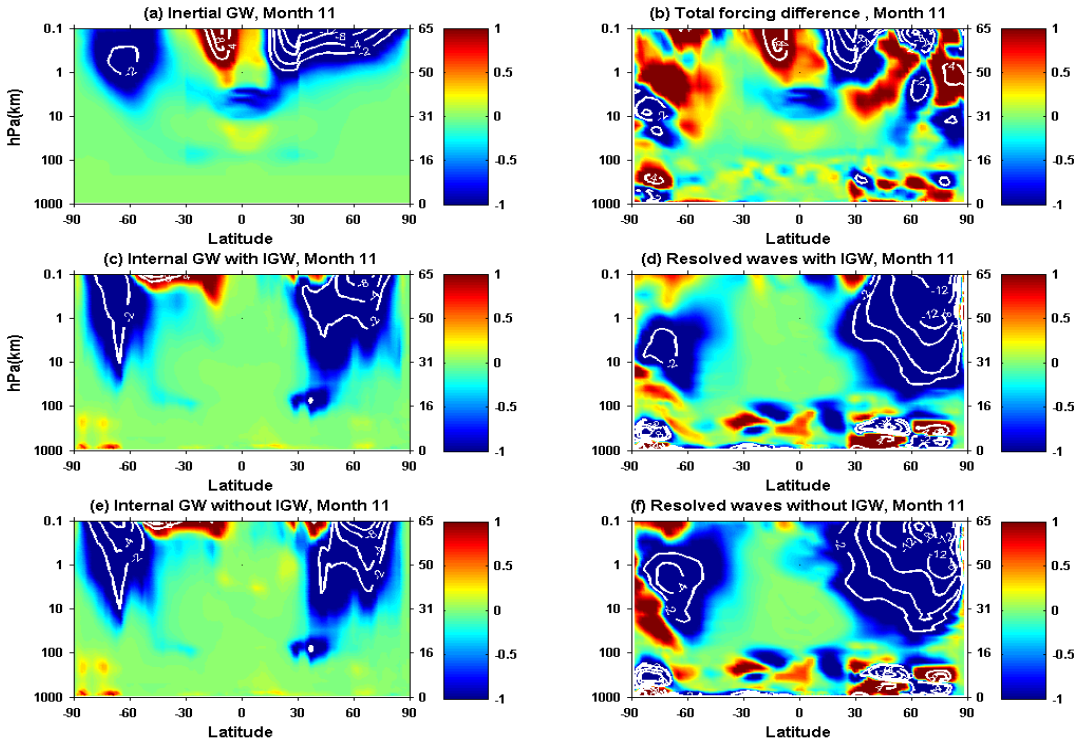

Figure 4.17: Similar to Figure 4.13, but for November

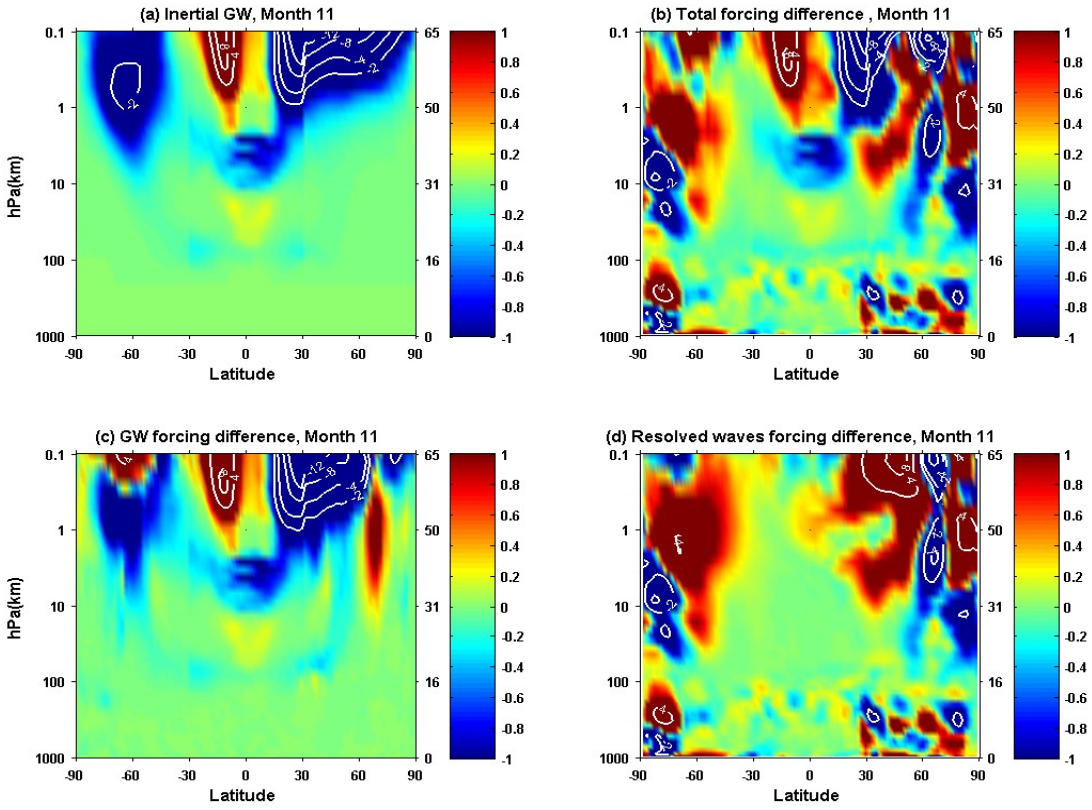

Figure 4.18: Similar to Figure 4.14, but for November

Figure 4.17 and Figure 4.18 display the wave forcing and wave forcing difference in the stratosphere. In November, both the IGWs and internal gravity waves break at lower altitudes than July in the southern hemisphere. In July, both the IGWs and internal gravity waves break above 1 hPa while in November the lowest breaking level of IGWs and internal gravity waves can reach 10 hPa and 50 hPa respectively. In November, the difference of GW forcing extends to 10 hPa from 1 hPa in July. This may explain why the temperature increases and zonal wind decelerations descend to around 50 hPa during spring.

4.8 Conclusions and Discussion

According to the simulation results shown in this sections, we conclude that the new IGW scheme used in this study is able to reduce the cold pole bias in the southern hemisphere. It

is not practical to include latitude dependence of IGW's horizontal wavelength in the WACCM simulation. Instead, a simplified spectrum with a single wavelength (1000km) is used. The parameterized IGWs break in the upper stratosphere and lower mesosphere. The forcing from IGW breaking compensates the missing wave forcing and decelerates the zonal wind in the southern stratosphere thus modifying the residual circulation. Originally the jet in the southern polar region during winter is about 20-30 m/s stronger than ERA-40 and the simulated temperature in the southern polar region between 10 hPa and 1 hPa during winter is 20 K colder than ERA-40. By choosing an appropriate efficiency factor for the IGWs, the jet speed can be reduced by 20-30 m/s, making the model results more consistent with ERA-40. At the same time, the simulated temperature between 10 hPa and 1 hPa in the southern polar region during winter is increased by 10 to 20 K, also in better agreement with ERA-40. The temperature changes are caused by the change of mean meridional circulation, and thus adiabatic heating, induced by the IGW wave forcing. Downward control, discussed in *Garcia and Boville* [1994], may also play an important role, especially at lower altitudes (below 1 hPa) where the direct wave forcing becomes weak.

The new IGW scheme is able to reduce the cold pole bias in both the specified chemistry WACCM simulation and interactive chemistry WACCM simulation. It is found that when the chemistry is included interactively in the simulation, the cold pole bias is reduced mainly through dynamics effects. This could be caused by the very weak prescribe ozone hole in the SC-WACCM simulations.

Based on the simulation results of this study, we conclude that the forcing from IGWs in the southern hemisphere from 30^{o} S to 90^{o} S is a viable candidate in reducing the cold pole bias. Parameterized IGWs in the equatorial region and in the northern hemisphere have very small

effects on the cold pole bias in the southern hemisphere. When the inertial gravity waves has been implemented only in the equatorial region from 30° S to 30° N, the cold pole bias are almost unaffected. When the inertial gravity waves are implemented from 30° S to 90° S and in the equatorial region, the cold pole bias are reduced significantly from 20 K to 5 K. When the inertial gravity waves scheme are implemented in both hemispheres from 30° S to 90° S and 30° N to 90° N, the simulated wind climatology and temperature climatology are almost the same as the cases in which the inertial gravity waves are only implemented in the southern hemisphere.

The zonal wind change induced by the IGWs in the northern hemisphere is much smaller than the southern hemisphere both in speed and area. One possible reason is that the zonal wind speed in the southern hemisphere is larger than the northern hemisphere because in the southern hemisphere most of the areas are oceans and the orographic gravity wave deceleration effect is small. The acceleration (or deceleration) of the zonal wind induced by IGWs is proportional to $(\bar{u} - c)^3$, c is the phase speed and u is the zonal wind [*Lindzen* 1981]. Therefore IGWs have the advantage to make relative large improvement to the climatology in the southern hemisphere while not significantly change or even improve the climatology in the northern hemisphere. This makes IGW a good candidate to reduce the cold pole bias, which is particularly acute in the southern hemisphere.

The IGW scheme used in this study is different with the orographic gravity wave scheme used to reduce the cold pole bias in *McLandress et al* [2011]. In *McLandress et al* [2011], the gravity wave scheme in CMAM has a gap at 60° S and they used additional orographic gravity waves to fill this gap. The orographic gravity waves used mainly breaks below 1 hPa. The IGW in our scheme mainly breaks above 1 hPa and the induced wave forcing peaks at around 0.1 hPa. Even though the original gravity wave forcing in WACCM has a gap around 60° S below 1 hPa,

which is similar to the wave forcing gap in CMAM, the IGW scheme we used does not enhance the forcing in this gap. Nevertheless, we have shown, however, that the IGW scheme used in this study is able to significantly reduce the cold pole bias, and improve temperature, zonal wind, wind reversal level and ozone mixing ratio. Observationally, *Wang et al.*, [2005] and *Alexander et al.,* [2008] showed evidence that inertial gravity existed globally at both hemispheres. Therefore the IGW scheme in this study is also physically plausible. As found in previous studies, the missing wave forcing is likely a cause of cold pole bias in CCMs. Both our study and *McLandress et al* [2011] support this conclusion. Our study demonstrates that the IGWs are a potential candidate for the source of the forcing.

Chapter 5 Conclusions and Outlooks

5.1 Conclusions

Lidar observations are critical in building a temperature benchmark in the southern polar region due to its high resolution and long-duration observation capability. The temperature morphology is formed using lidar observations at South Pole from November 1999 to October 2001 and at Rothera (67.5 S, 68.0 W) from January 2003 to March 2005. Annual, semi-annual, 4-, 3- and 2.4-month oscillations are decomposed and analysed respectively. This temperature morphology is compared to SABER for the purpose of mutual validation. The bias in WACCM simulation is identified and the cold pole bias in the southern polar region is quantified, which inspired us to study the mechanism of cold pole bias and to reduce the cold pole bias using inertial gravity waves.

Even with high resolution and long duration lidar observation, it is still a very challenging task to establish the benchmark because temperatures are affected by so many factors and the variations in the polar region are not fully understood yet. Teleconnection is one critical variation need to be understood before any temperature benchmark can be established because it significantly affects the temperature variations in the polar region. Through the research in this dissertation we further the knowledge of temperature variations induced by teleconnection. Teleconnection in the thermosphere is discovered, along with the inter- and intra-annual variations. The connections between residual circulation and temperature are formed. A stable teleconnection pattern is established globally.

After the cold pole bias in WACCM being quantified using lidar observation as reference,

we continue to study the mechanism of the cold pole bias and to reduce the bias in WACCM using inertial gravity wave parameterizations. This study advances our knowledge of how the gravity waves affect temperature in the polar region. Originally in WACCM the inertial gravity wave is not parameterized at all. The gravity wave parameterization we proposed is to launch inertial gravity waves with horizontal wavelength 1000 km uniformly from 30 S to 90 S and from 30 N to 90 N. Inertial gravity waves have longer wavelength than the mesoscale gravity waves already parameterized in WACCM and thus break at lower altitudes. Therefore this new inertial gravity wave is able to compensate the missing wave forcing in the southern stratosphere and reduce the cold pole bias. This new gravity wave scheme is tested in WACCM simulations. In our experiments, with additional inertial gravity waves, the zonal wind is slowed by 20-30 m/s and the temperature is increased by about 20 K at stratosphere in the southern polar region, making the simulation results of WACCM consistent with ERA-40 better. In addition, the wind reversal level between October and December is decreased by 10 km, making it similar to ERA-40. The zonal wind climatology in WACCM simulation is improved and the cold pole bias is reduced to almost 0 when the new inertial gravity wave parameterization is used. The wave forcing of inertial gravity wave, internal gravity wave and resolved wave are analysed which further our understanding of the dynamics and temperature variances in the southern polar region.

The results in this thesis help advance our understanding of the polar region thermal structure and how dynamics affect the temperature variations. This thesis helps to understand better how gravity waves affect temperature in the polar region. It lays the foundation to establish the temperature benchmark for future studies of climate change.

Base on the study in this thesis, we have raised many interesting science questions which can further advance our knowledge of the temperature and dynamics in the southern polar region. These topics will be discussed below.

5.2 Future Work

The Fe/Rayleigh lidar is upgraded and deployed at McMurdo (77.8ºS, 166.7ºE) in 2010. The upgraded lidar is capable of measuring atmospheric temperature profiles from sea level to 110 km with year-round (0-110 km) and full-diurnal (30-110 km) coverage for both day and night. This lidar has accumulated a lot of valuable data and will continue be operated for several years. Those new data will fill an important gap in the latitudinal coverage of ground-based range-resolved measurements in Antarctica and help forming a more complete morphology in the southern polar region.

The new gravity wave scheme with addition inertial gravity wave is able to reduce the cold pole bias in WACCM. But all other parameterizations of WACCM such as ozone were determined according to the original gravity wave scheme. To include inertial gravity wave forcing, the parameters of atmosphere chemistry and other wave forcing need to be adjusted according to the new gravity wave scheme. More work need to be done in the future to completely solve this cold pole bias.

In current dissertation, the teleconnection is derived using WACCM 3.5 simulation and the new gravity wave scheme is not included. New gravity scheme will change both the simulated residual circulation and simulated temperature and thus affecting the derived teleconnection. When the cold pole bias is solved in WACCM, the teleconnection can be derived using the simulation from upgraded WACCM and the effects of new gravity scheme on teleconnection can be studied.

Bibliography

Alexander, M. J., S. D. Eckermann, D. Broutman, and J. Ma (2009), Momentum flux estimates for South Georgia Island mountain waves in the stratosphere observed via satellite, Geophys. Res. Lett., 36, L12816, doi:10.1029/2009GL038587.

Alexander, M. J., et al. (2008), Global estimates of gravity wave momentum flux from High Resolution Dynamics Limb Sounder observations, J. Geophys. Res., 113(D15), D15S18.

Andrews, D. G., J. R. Holton, and C. B. Leovy (1987), Middle atmosphere dynamics, Academic Press, ISBN-10: 9780120585762.

Austin, J., et al. (2003), Uncertainties and assessments of chemistry-climate models of the stratosphere, Atmos. Chem. Phys., 3, 1-27.

Balachandran, N., and D. Rind (1995), Modeling the Effects of UV Variability and the QBO on the Troposphere–Stratosphere System. Part I:. The Middle Atmosphere. J. Climate, 8, 2058–2079.

Becker, E., and G. Schmitz (2003), Climatological effects of orography and land-sea heating contrasts on the gravity wave-driven circulation of the mesosphere, J. Atmos. Sci., 60(1), 103-118.

Becker, E., A. Müllemann, F.-J. Lübken, H. Körnich, P. Hoffmann, and M. Rapp (2004), High Rossby-wave activity in austral winter 2002: Modulation of the general circulation of the MLT during the MaCWAVE/MIDAS northern summer program, Geophys. Res. Lett., 31, L24S03, doi:10.1029/2004GL019615.

Becker, E., and D. C. Fritts (2006), Enhanced gravity-wave activity and interhemispheric coupling during the MaCWAVE/MIDAS northern summer program 2002, Ann. Geophys., 24(4), 1175-1188.

Chandran, A., R. L. Collins, R. R. Garcia, and D. R. Marsh (2011), A case study of an elevated stratopause generated in the Whole Atmosphere Community Climate Model, Geophys. Res. Lett., 38, L08804, doi:10.1029/2010GL046566.

Chu, X., W. Pan, G. C. Papen, C. S. Gardner, and J. A. Gelbwachs (2002), Fe Boltzmann temperature lidar: Design, error analysis, and initial results at the North and South Poles, Appl. Opt., 41, 4400– 4410.

Chu, X. Z., C. S. Gardner, and R. G. Roble (2003), Lidar studies of interannual, seasonal, and diurnal variations of polar mesospheric clouds at the South Pole, J. Geophys. Res.-Atmos., 108(D8).

Chu, X. Z., G. J. Nott, P. J. Espy, C. S. Gardner, J. C. Diettrich, M. A. Clilverd, and M. J. Jarvis (2004), Lidar observations of polar mesospheric clouds at Rothera, Antarctica (67.5 degrees S, 68.0 degrees W), Geophysical Research Letters, 31(2).

Chu, X. Z., C. S. Gardner, and S. J. Franke (2005), Nocturnal thermal structure of the mesosphere and lower thermosphere region at Maui, Hawaii (20.7 degrees N), and Starfire Optical Range, New Mexico (35 degrees N), J. Geophys. Res.-Atmos., 110(D9).

Chu, X., and G. C. Papen (2005), Resonance Fluorescence Lidar for Measurements of the Middle and Upper Atmosphere, in the book of *Laser Remote Sensing*, edited by T. Fujii and T. Fukuchi, published by CRC Press, Taylor & Francis Group, ISBN: 0-8247-4256-7, page 179-432.

Chu, X. Z., P. J. Espy, G. J. Nott, J. C. Diettrich, and C. S. Gardner (2006), Polar mesospheric clouds observed by an iron Boltzmann lidar at Rothera (67.5 degrees S, 68.0 degrees W), Antarctica from 2002 to 2005: Properties and implications, J. Geophys. Res.-Atmos., 111(D20).

Espy, P. J., S. Ochoa Fernández, P. Forkman, D. Murtagh, and J. Stegman (2011), The role of the QBO in the inter-hemispheric coupling of summer mesospheric temperatures, *Atmos. Chem. Phys*., 11(2), 495-502.

Eyring, V., et al. (2006), Assessment of temperature, trace species, and ozone in chemistry-climate model simulations of the recent past, J. Geophys. Res., 111, D22308, doi:10.1029/2006JD007327

Friedman, J. S., and X. Z. Chu (2007), Nocturnal temperature structure in the mesopause region over the Arecibo Observatory (18.35 degrees N, 66.75 degrees W): Seasonal variations, J. Geophys. Res.-Atmos., 112(D14).

Gardner, C. S. (1989), Sodium resonance fluorescence lidar applications in atmospheric science and astronomy, Proc. IEEE 77, 408–418.

Garcia, R. R., and S. Solomon(1985), The effect of breaking gravity waves on the dynamical and chemical composition of the mesosphere and lower thermosphere, J. Geophys. Res., 90, 3850–3868.

Garcia, R. R., and B. A. Boville (1994), Downward Control of The Mean Meridional Circulation

and Temperature Distribution of The Polar Winter Sstratosphere, J. Atmos. Sci., 51(15), 2238-2245.

Garcia, R. R., D. R. Marsh, D. E. Kinnison, B. A. Boville, and F. Sassi (2007), Simulation of secular trends in the middle atmosphere, 1950-2003, *J. Geophys. Res., 112*, D09301, doi:10.1029/2006JD007485.

Gumbel, J., and B. Karlsson (2011), Intra- and inter-hemispheric coupling effects on the polar summer mesosphere, *Geophys. Res. Lett.*, *38*, L14804, doi:10.1029/2011GL047968.

Haynes, P. H., C. J. Marks, M. E. McIntyre, T. G. Shepherd, and K. P. Shine (1991), On the downward control of extratropical diabatic circulations by eddy-induced mean zonal forces, J. Atmos. Sci., 48(4), 651-679.

Hauchecorne, A. and M. Chanin (1980), Density and temperature profiles obtained by lidar between 35 and 70 km, Geophys. Res. Lett., 7(8), 565–568, doi:10.1029/GL007i008p00565.

Hines, C. O. (1997), Doppler-spread parameterization of gravity-wave momentum deposition in the middle atmosphere. Part 1: Basic formulation, Journal of Atmospheric and Solar-Terrestrial Physics, 59(4), 371-386

Hitchman, M. H., J. C. Gille, C. D. Rodgers, and G. Brasseur (1989), The Separated Polar Winter Stratopause - A Gravity-Wave Driven Climatological Feature, J. Atmos. Sci., 46(3), 410-422.

Holton, J. R.(1982), The role of gravity wave induced drag and diffusion in the momentum budget of the mesosphere, J. Atmos. Sci., 39, 791–799.

Holton, J. R. (1992), An introduction to dynamic meteorology, Academic Press, ISBN 0-12-354355-X.

IPCC – Intergovernmental Panel on Climate Change, Third Assessment Report – Climate Change 2001: The Scientific Basis, J. T. Houghton, Y. Ding, D. J. Griggs, M. Noguer, P. J. van der Linden, X. Dai, K. Maskell, C. A. Johnson (Eds.), Cambridge University Press, Cambridge, UK, 2001.

Karlsson, B., H. Körnich, and J. Gumbel (2007), Evidence for interhemispheric stratosphere-mesosphere coupling derived from noctilucent cloud properties, *Geophys. Res. Lett.*, *34*, L16806, doi:10.1029/2007GL030282.

Karlsson, B., C. McLandress, and T. G. Shepherd (2009a), Inter-hemispheric mesospheric coupling in a comprehensive middle atmosphere model, *J. Atmos. Sol. Terr. Phys.*, *71*, 518-530, doi:10.1016/j.jastp.2008.08.006.

Karlsson, B., C. E. Randall, S. Benze, M. Mills, V. L. Harvey, S. M. Bailey, and J. M. Russell (2009b), Intra-seasonal variability of polar mesospheric clouds due to inter-hemispheric coupling, *Geophys. Res. Lett., 36*, L20802, doi:10.1029/2009GL040348.

Karlsson, B., C. E. Randall, T. G. Shepherd, V. L. Harvey, J. Lumpe, K. Nielsen, S. M. Bailey, M. Hervig, and J. M. Russell III (2011), On the seasonal onset of polar mesospheric clouds and the breakdown of the stratospheric polar vortex in the Southern Hemisphere, *J. Geophys. Res., 116,* D18107, doi:10.1029/2011JD015989.

Körnich, H., and E. Becker (2010), A simple model for the interhemispheric coupling of the middle atmosphere circulation, *Adv. Space Res.*, *45*(5), 661-668.

Kruger, K., B. Naujokat, and K. Labitzke (2005), The unusual midwinter warming in the Southern Hemisphere stratosphere 2002: A comparison to northern hemisphere phenomena, J. Atmos. Sci., 62(3), 603-613.

Langematz, U., and M. Kunze (2008), Dynamical changes in the Arctic and Antarctic stratosphere during spring, Climate Variability and Extremes during the Past 100 Years, edited by S. Brönnimann, J. Luterbacher, T. Ewen, H. F. Diaz, R. S. Stolarski and U. Neu, pp. 293-301, Springer Netherlands.

Lindzen, R. S.(1981), Turbulence and stress due to gravity wave and tidal breakdown, J. Geophys.Res., 86, 9701–9714.

Manzini, E. and N. A. McFarlane (1998), The effect of varying the source spectrum of a gravity wave parameterization in a middle atmosphere general circulation model, J. Geophys. Res., 103(D24), 31,523–31,539, doi:10.1029/98JD02274.

Manney, G. L., M. J. Schwartz, K. Kruger, M. L. Santee, S. Pawson, J. N. Lee, W. H. Daffer, R. A. Fuller, and N. J. Livesey (2009), Aura Microwave Limb Sounder observations of dynamics and transport during the record-breaking 2009 Arctic stratospheric major warming, Geophysical Research Letters, 36.

Matsuno, T., and K. Nakamura (1979), Eulerian-mean and lagrangian-mean meridional circulations in the stratosphere at the time of a sudden warming, *J. Atmos. Sci.*, *36*(4), 640-654.

McFarlane, N. A.(1987), The effect of orographically excited gravity wave drag on the general circulation of the lower stratosphere and troposphere, J. Atmos. Sci., 44, 1775–1800.

McLandress, C., T. G. Shepherd, S. Polavarapu, and S. R. Beagley (2011), Is Missing Orographic Gravity Wave Drag near 60°S the Cause of the Stratospheric Zonal Wind Biases in Chemistry–Climate Models?, J. Atmos. Sci., 69(3), 802-818.

Medvedev, A. S. and G. P. Klaassen (1995), Vertical evolution of gravity wave spectra and the parameterization of associated wave drag, J. Geophys. Res., 100(D12), 25,841–25,853,

doi:10.1029/95JD02533.

Neale, R. B. et al. (2010), Description of the NCAR Community Atmosphere Model (CAM 5.0) NCAR/TN-486+STR, NCAR TECHNICAL NOTE

Pan, W. L., and C. S. Gardner (2003), Seasonal variations of the atmospheric temperature structure at South Pole, J. Geophys. Res.-Atmos., 108(D18).

Plane, J. M. C.(2003), Atmospheric chemistry of meteoric metals, Chem. Rev., 103(12), 4963–4984.

Remsberg, E. E., L. L. Gordley, B. T. Marshall, R. E. Thompson, J. Burton, P. Bhatt, V. L. Harvey, G. Lingenfelser, and M. Natarajan (2004), The Nimbus 7 LIMS version 6 radiance conditioning and temperature retrieval methods and results, *J. Quant. Spectrosc. Radiat. Transf., 86*(4), 395-424.

Richter, J. H., F. Sassi, R. R. Garcia, K. Matthes, and C. A. Fischer (2008), Dynamics of the middle atmosphere as simulated by the Whole Atmosphere Community Climate Model, version 3 (WACCM3), *J. Geophys. Res., 113,* D08101, doi:10.1029/2007JD009269.

Richter, J. H., F. Sassi, and R. R. Garcia (2010), Towards a physically based gravity wave source parameterization in a general circulation model, *J. Atmos. Sci., 67*, 136–156.

Roble, R. G.(1995), Energetics of the mesosphere and thermosphere, The Upper Mesosphere and Lower Thermosphere: A review of experiment and theory, Geophys. Monogr., 87, 1-22.

Russell III, J. M., M. G. Mlynczak, L. L. Gordley, J. J. Tansock, Jr. and R. W. Esplin (1999), Overview of the SABER experiment and preliminary calibration results, *Proc. SPIE 3756*, 277; doi:10.1117/12.366382.

Sato, K., S. Watanabe, Y. Kawatani, Y. Tomikawa, K. Miyazaki, and M. Takahashi (2009), On the origins of mesospheric gravity waves, Geophys. Res. Lett., 36, L19801, doi:10.1029/2009GL039908.

Solomon, S.(1999), Stratospheric ozone depletion: A review of concepts and history, Rev. Geophys., 37, 275- 316.

States, R. J., and C. S. Gardner (2000), Thermal structure of the mesopause region (80-105 km) at 40 degrees N latitude. Part I: Seasonal variations, J. Atmos. Sci., 57(1), 66-77.

Thurairajah, B., R. L. Collins, V. L. Harvey, R. S. Lieberman, and K. Mizutani (2010), Rayleigh lidar observations of reduced gravity wave activity during the formation of an elevated stratopause in 2004 at Chatanika, Alaska (65 degrees N, 147 degrees W), J. Geophys. Res.-Atmos., 115.

Thomas, G. E.(1991), Mesospheric clouds and the physics of the mesopause region, Reviews of Geophysics, 29, 553-575.

Uppala, S. M., et al. (2005), The ERA-40 re-analysis, Q. J. R. Meteorol. Soc., 131, 2961–3012, doi:10.1256/qj.04.176.

Wang, L., M. A. Geller, and M. J. Alexander (2005), Spatial and Temporal Variations of Gravity Wave Parameters. Part I: Intrinsic Frequency, Wavelength, and Vertical Propagation Direction, J. Atmos. Sci., 62(1), 125-142.

Warner, C. D. and M. E. McIntyre (1999), Toward an ultra-simple spectral gravity wave parameterization for general circulation models, Earth Planets Space, 51, 475–484.

Whiteway, J. A., and A. I. Carswell (1994), Rayleigh lidar observations of thermal structure and gravity wave activity in the high Arctic during a stratospheric warming, J. Atmos. Sci., 51, 3122–3136, doi:10.1175/1520-0469(1994)051<3122:RLOOTS>2.0.CO;2.

Xu, X., A. H. Manson, C. E. Meek, T. Chshyolkova, J. R. Drummond, C. M. Hall, D. M. Riggin, and R. E. Hibbins (2009), Vertical and interhemispheric links in the stratosphere-mesosphere as revealed by the day-to-day variability of Aura-MLS temperature data, *Ann. Geophys.*, *27*(9), 3387-3409.

Xue, X.-H., H.-L. Liu, and X.-K. Dou (2012), Parameterization of the inertial gravity waves and generation of the quasi-biennial oscillation, J. Geophys. Res., 117, D06103, doi:10.1029/2011JD016778.

Yuan, T., C. Y. She, D. A. Krueger, F. Sassi, R. Garcia, R. G. Roble, H. L. Liu, and H. Schmidt (2008), Climatology of mesopause region temperature, zonal wind, and meridional wind over Fort Collins, Colorado (41 degrees N, 105 degrees W), and comparison with model simulations, J. Geophys. Res.-Atmos., 113(D3).

Yulaeva, E., J. R. Holton, and J. M. Wallace (1994), On the cause of the annual cycle in tropical lower-stratospheric temperatures, J. Atmos. Sci., 51(2), 169-174.

Appendix A

In this appendix we show the zonal wind climatology simulated by WACCM with and without IGW scheme month by month. The figures are similar to Figure 4.3.

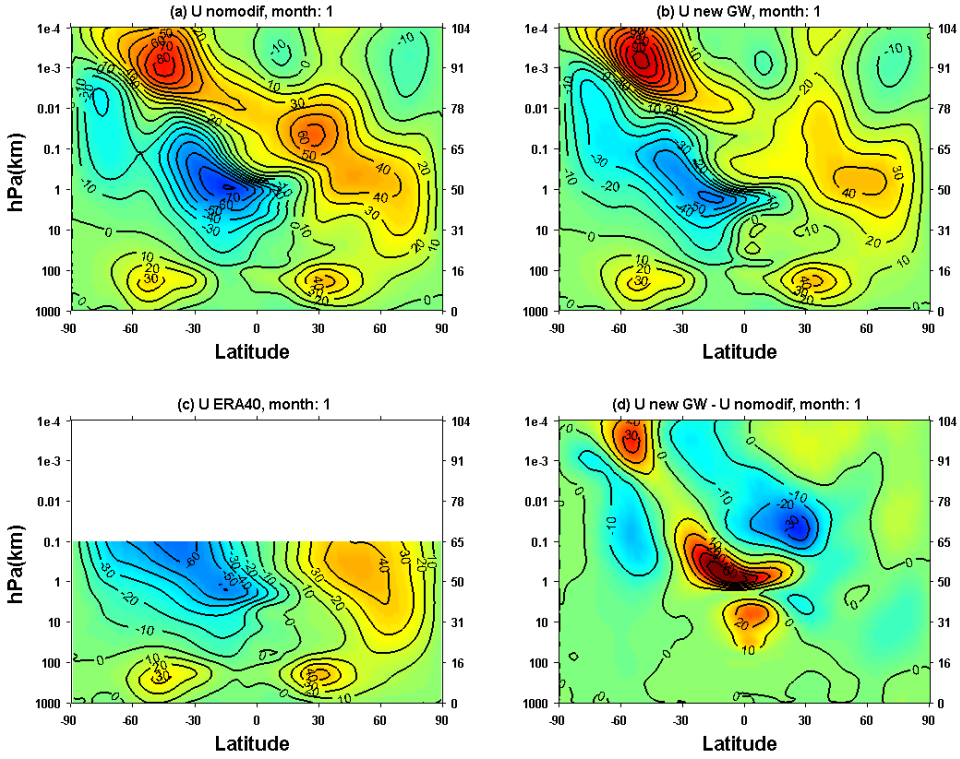

Figure A.1 Zonal wind climatology of January simulated by SC-WACCM

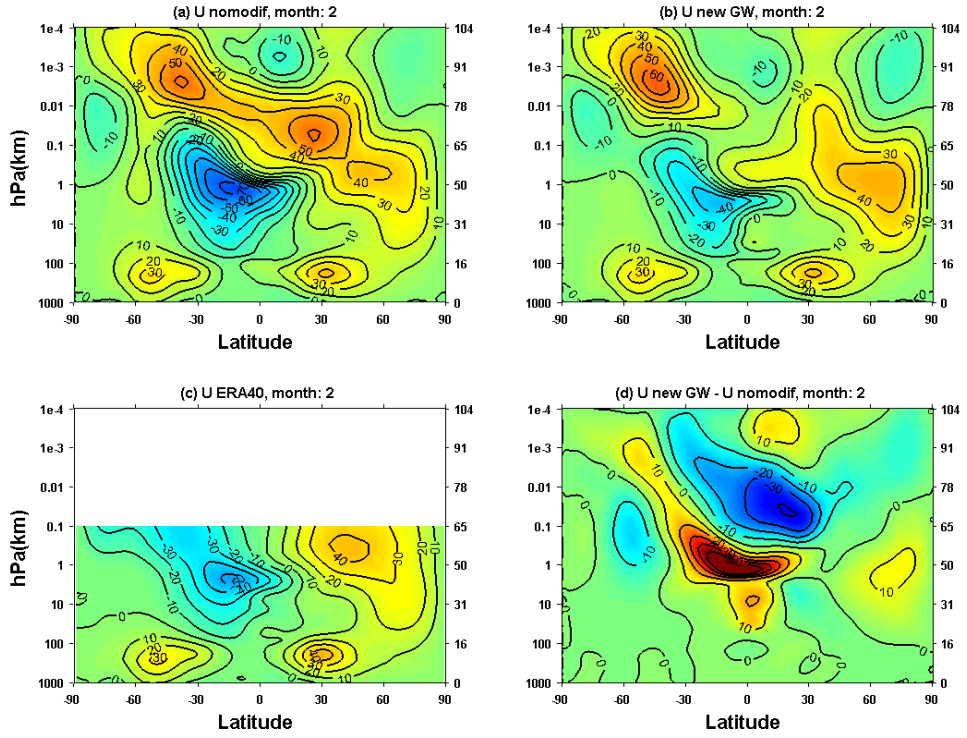

Figure A.2 Zonal wind climatology of February simulated by SC-WACCM

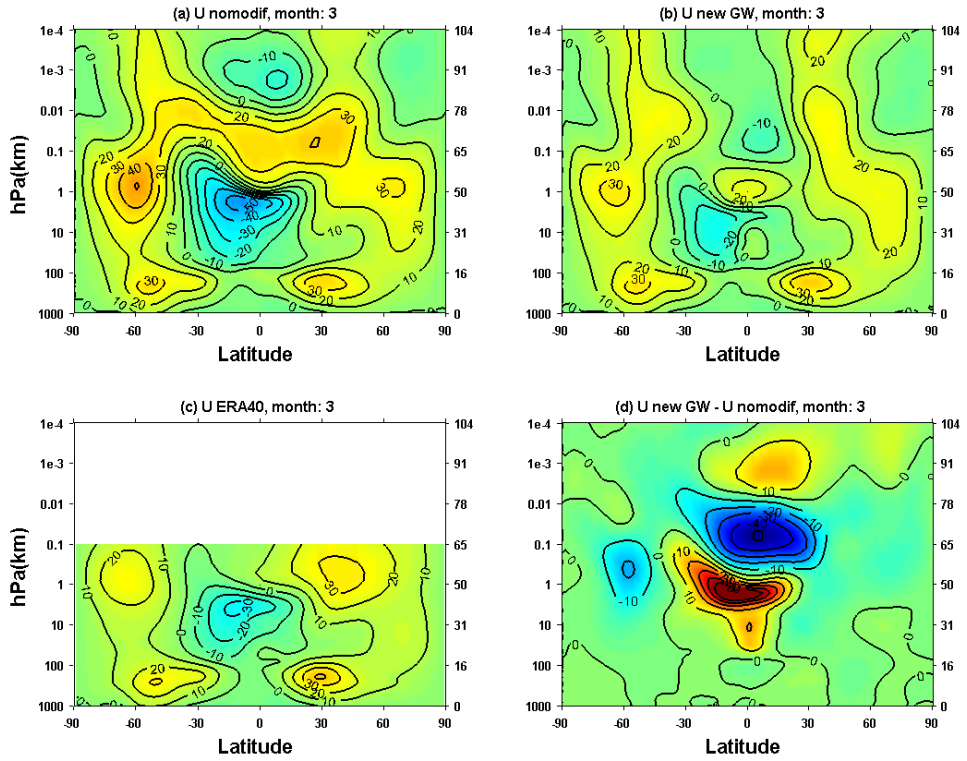

Figure A.3 Zonal wind climatology of March simulated by SC-WACCM

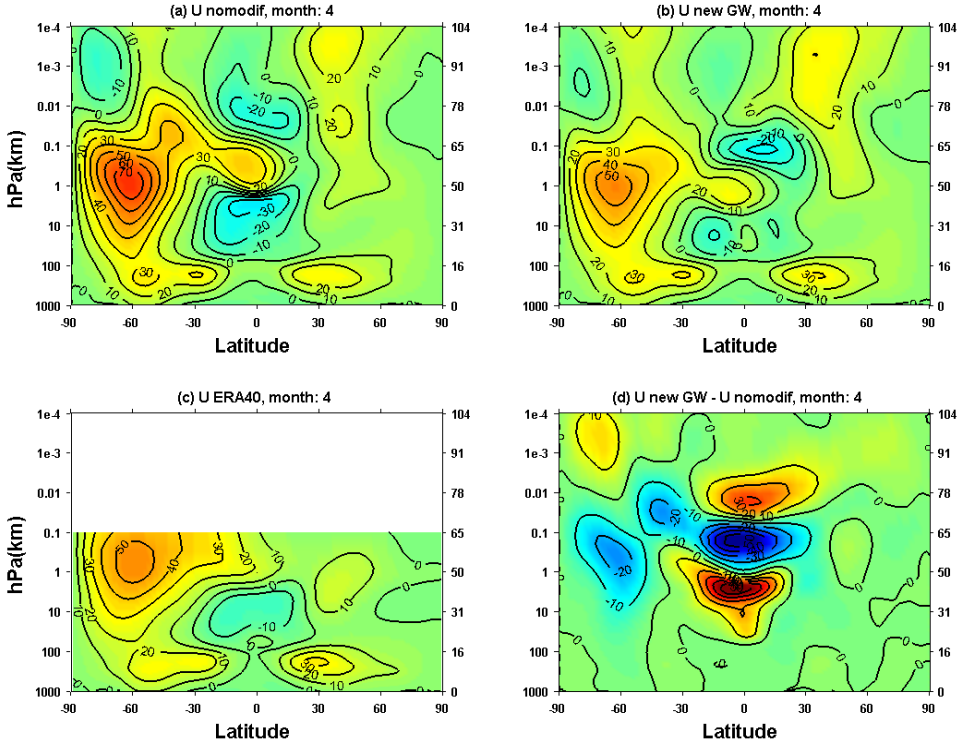

Figure A.4 Zonal wind climatology of April simulated by SC-WACCM

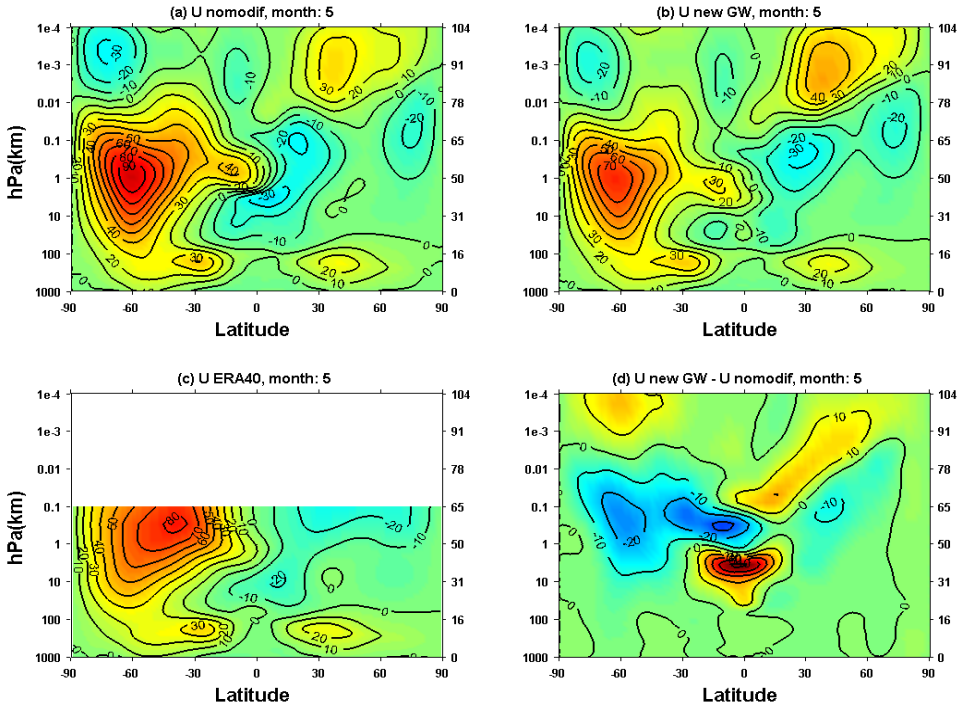

Figure A.5 Zonal wind climatology of May simulated by SC-WACCM

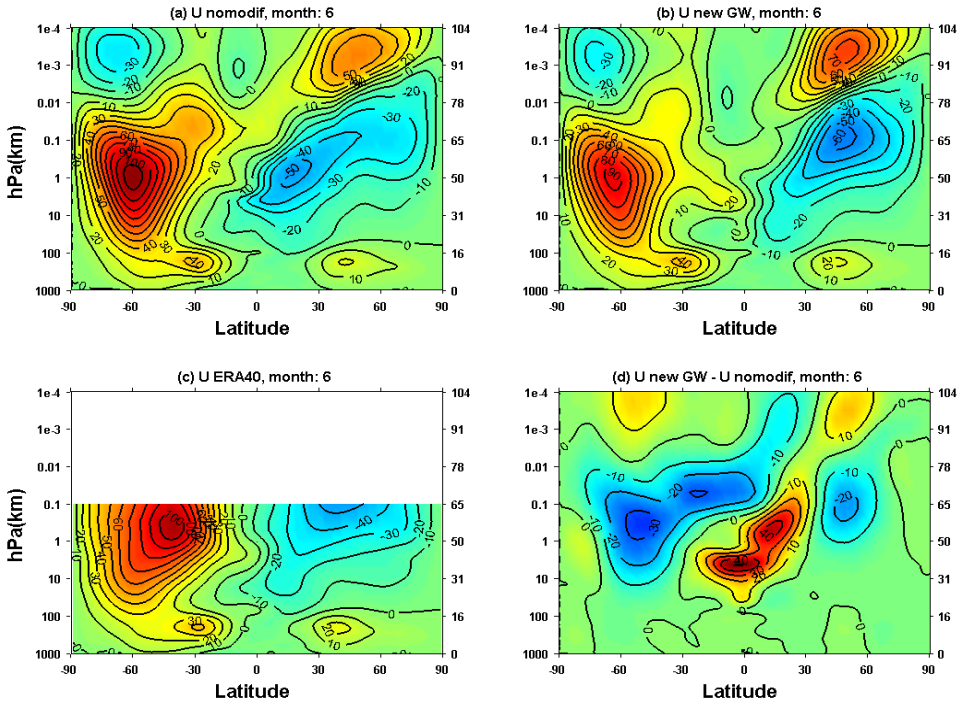

Figure A.6 Zonal wind climatology of June simulated by SC-WACCM

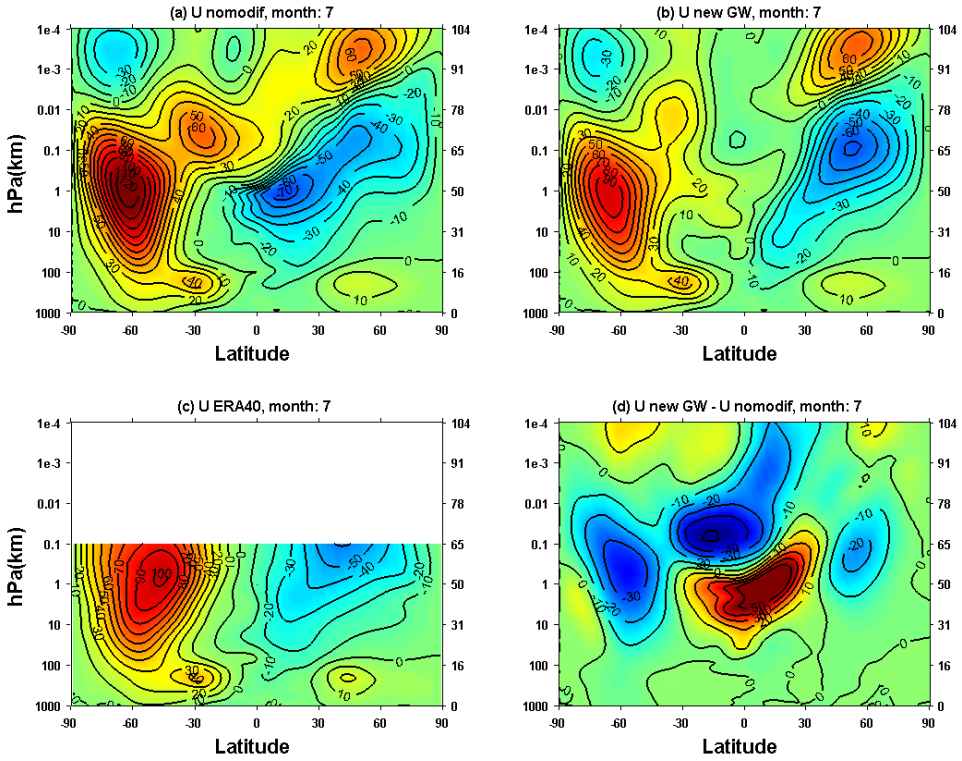

Figure A.7 Zonal wind climatology of July simulated by SC-WACCM

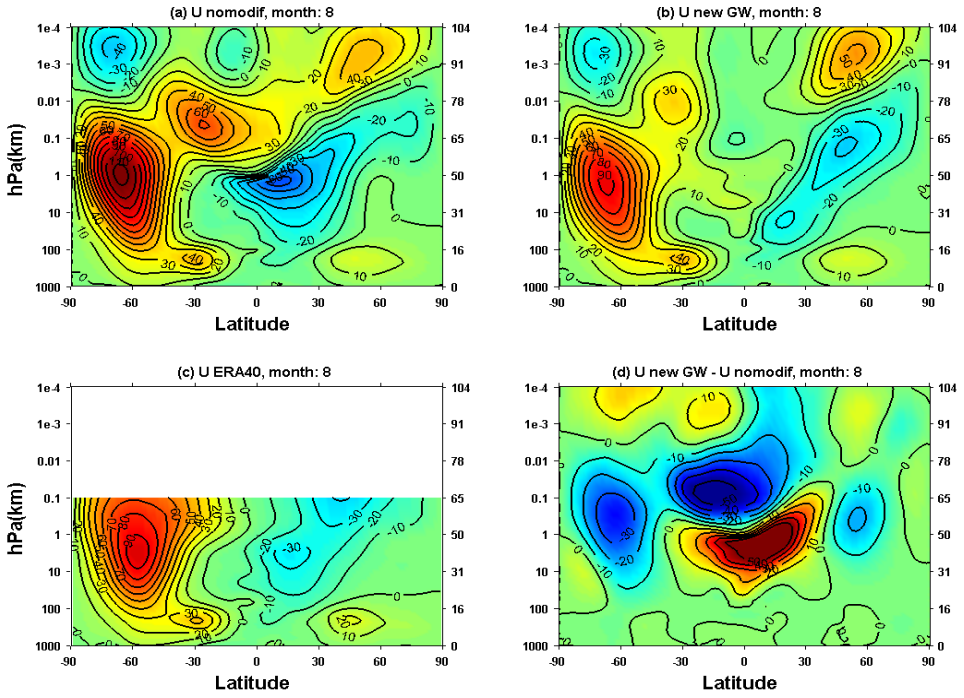

Figure A.8 Zonal wind climatology of August simulated by SC-WACCM

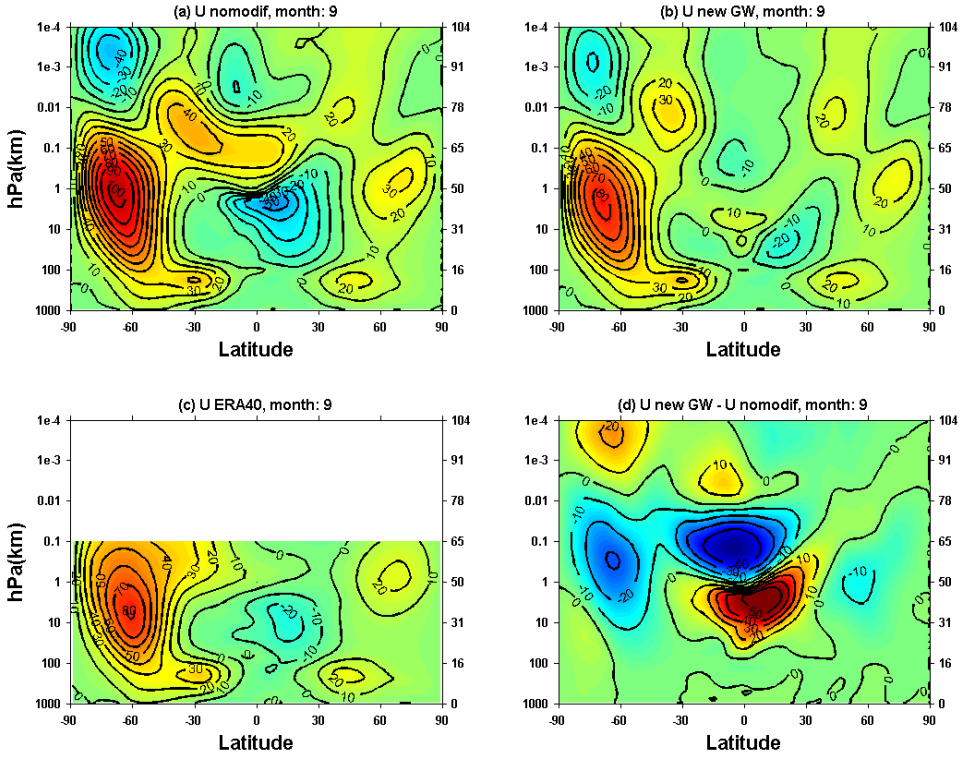

Figure A.9 Zonal wind climatology of September simulated by SC-WACCM

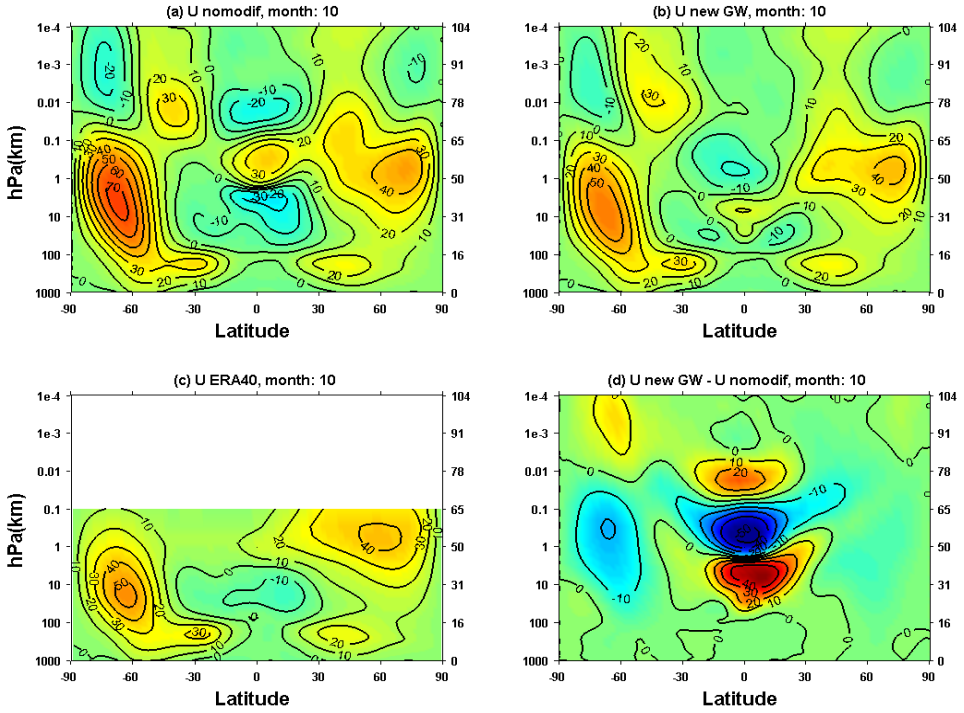

Figure A.10 Zonal wind climatology of October simulated by SC-WACCM

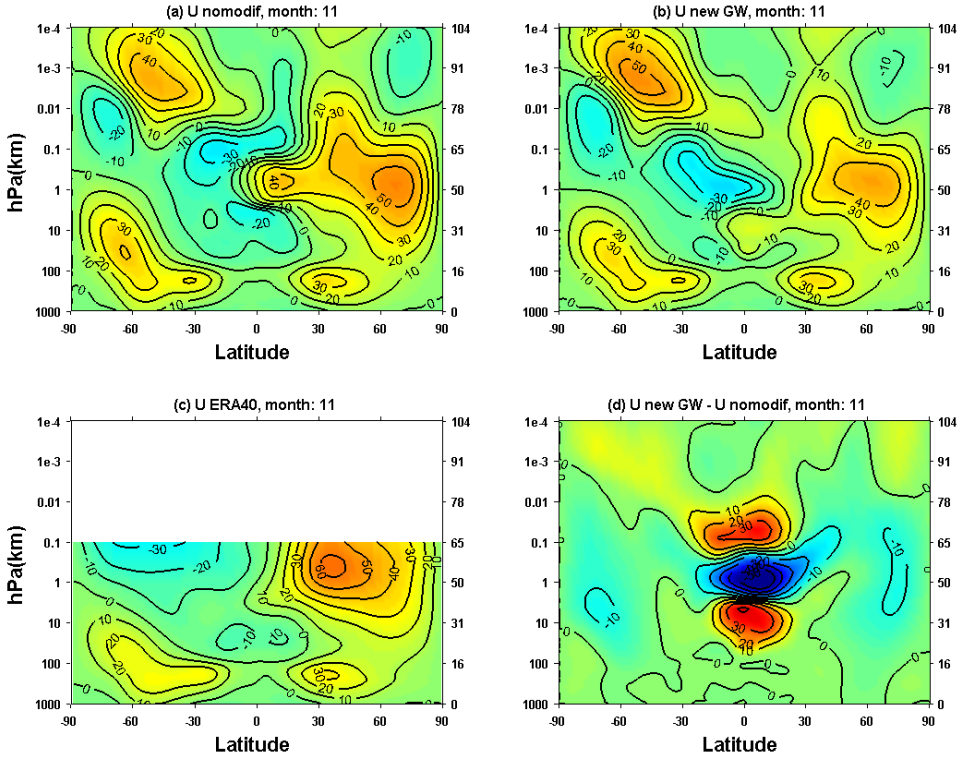

Figure A.11 Zonal wind climatology of November simulated by SC-WACCM

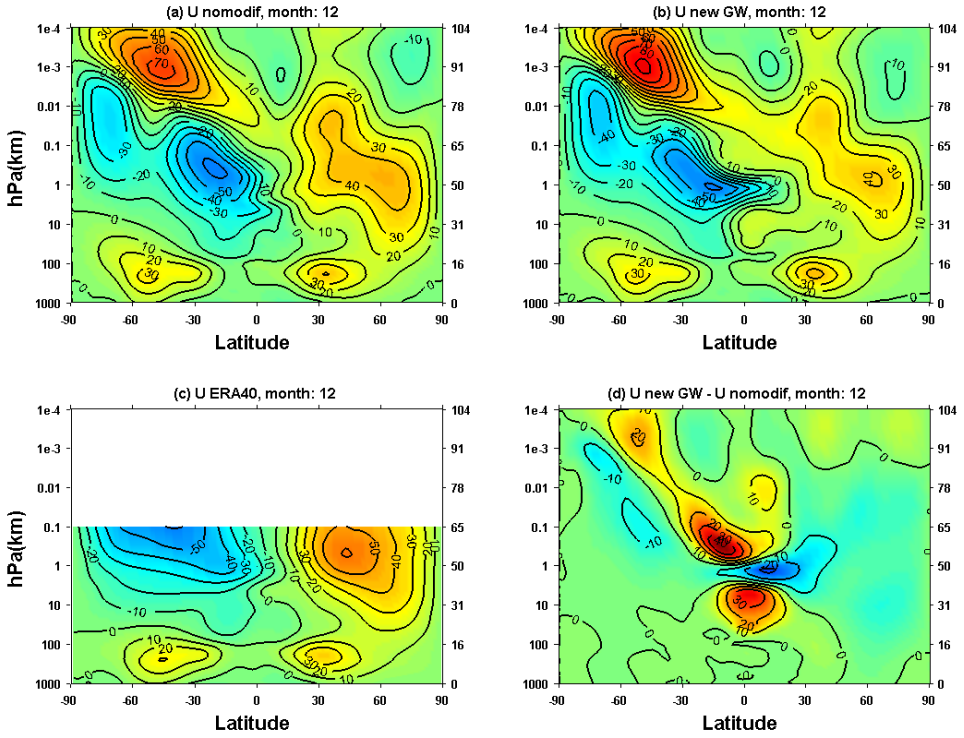

Figure A.12 Zonal wind climatology of December simulated by SC-WACCM

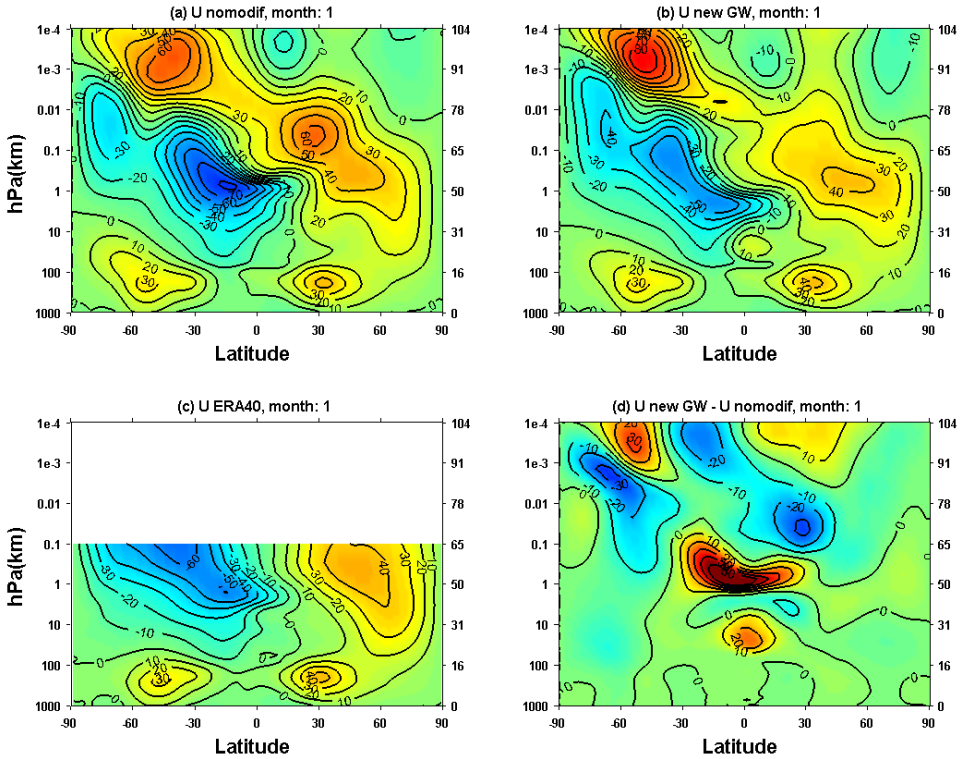

Figure A.13 Zonal wind climatology of January simulated by WACCM

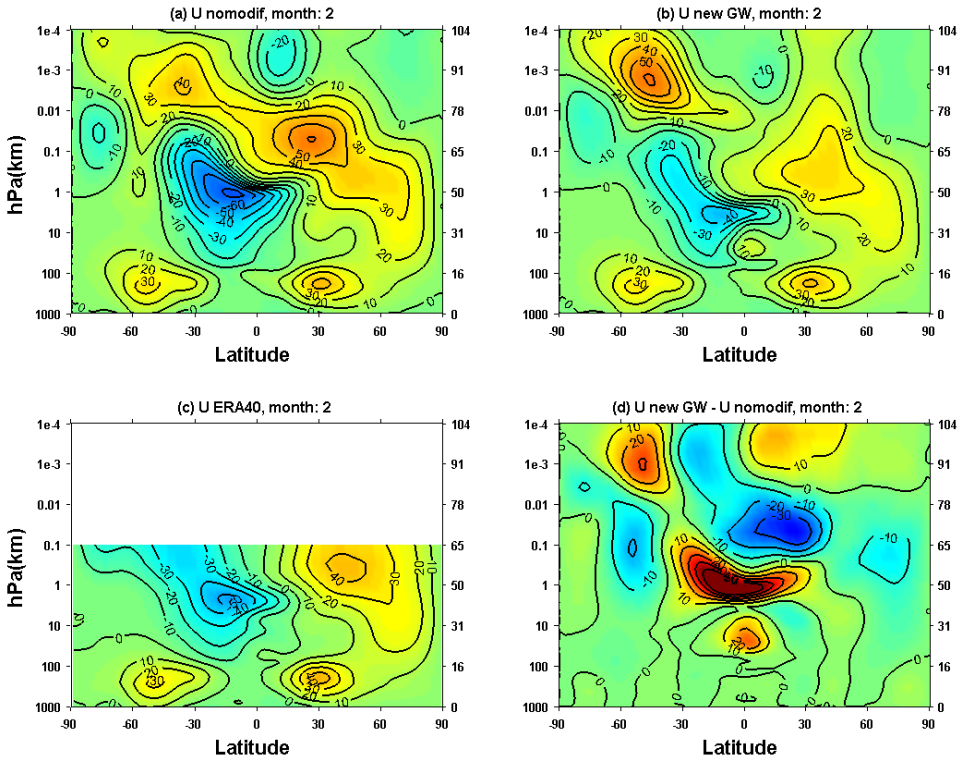

Figure A.14 Zonal wind climatology of February simulated by WACCM

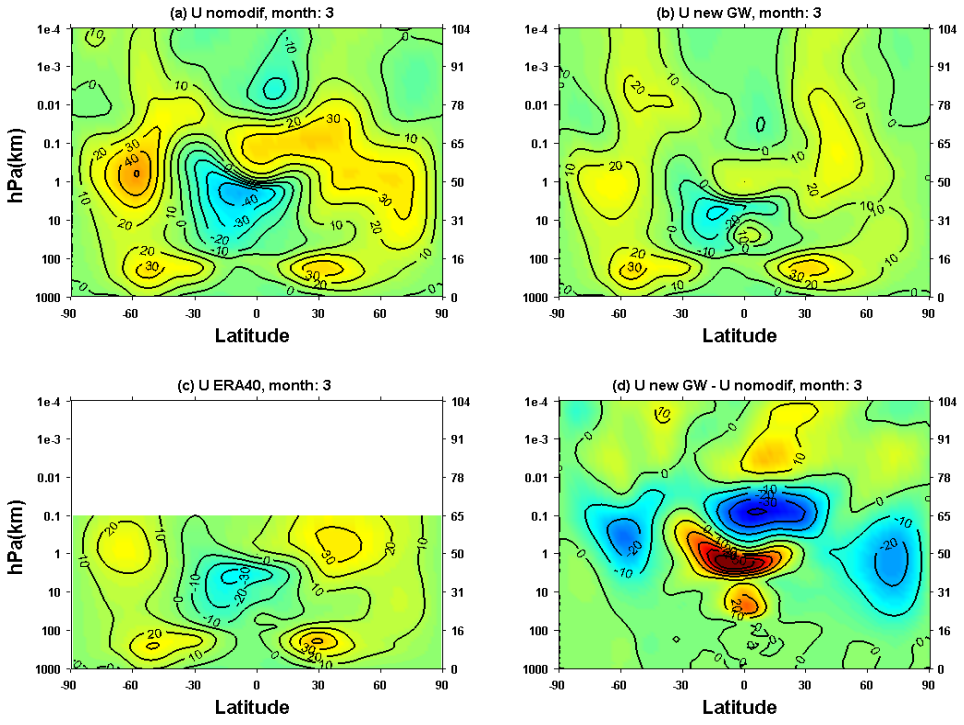

Figure A.15 Zonal wind climatology of March simulated by WACCM

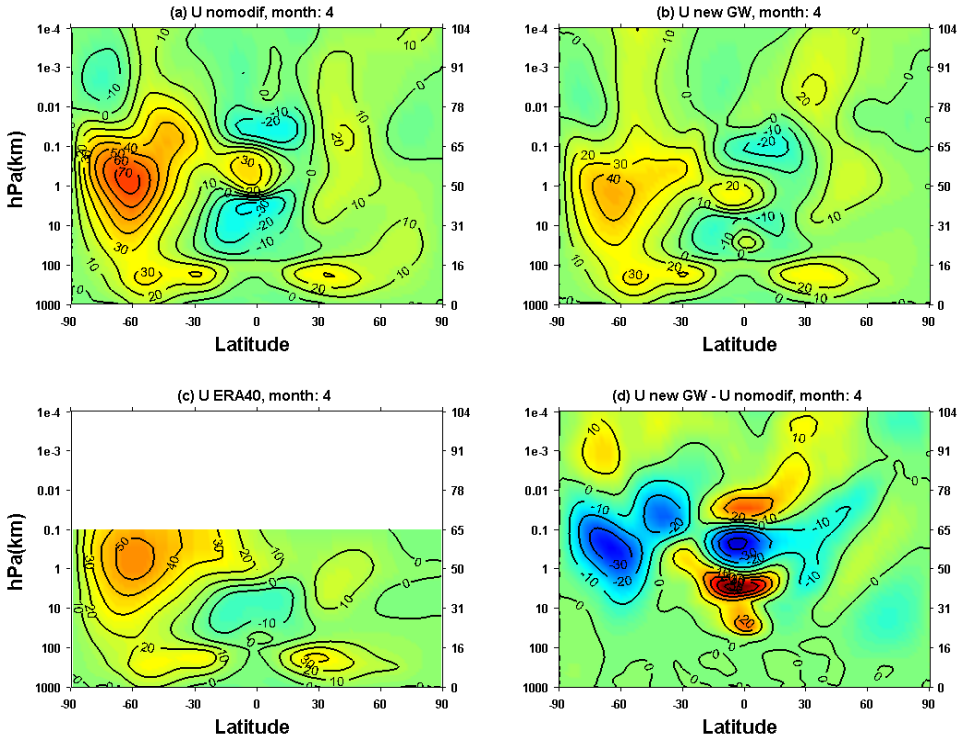

Figure A.16 Zonal wind climatology of April simulated by WACCM

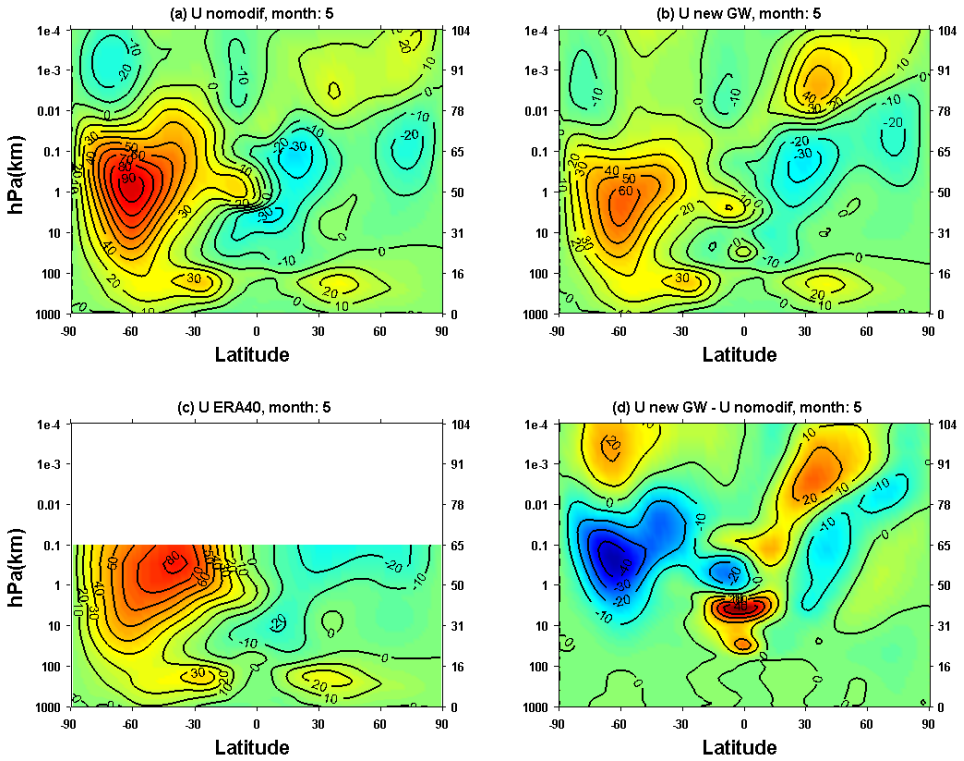

Figure A.17 Zonal wind climatology of May simulated by WACCM

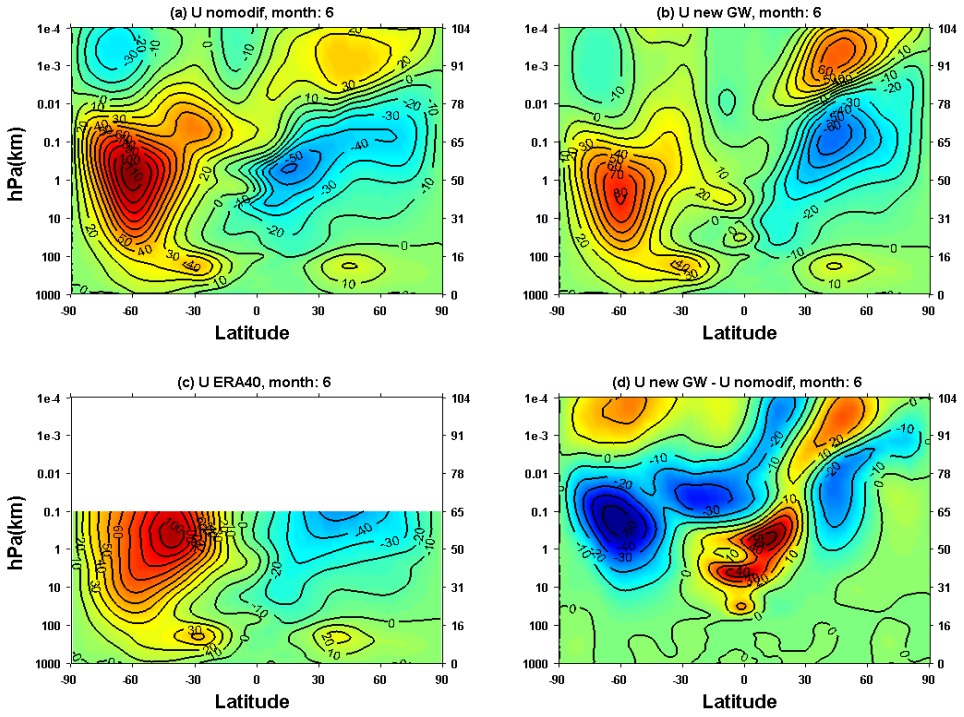

Figure A.18 Zonal wind climatology of June simulated by WACCM

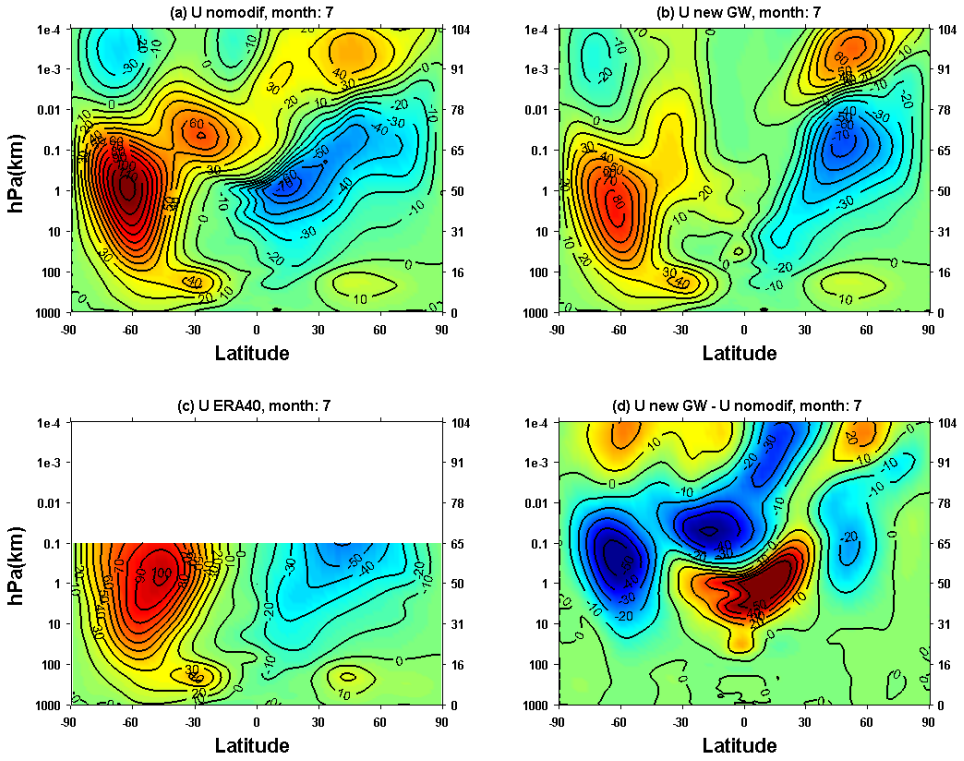

Figure A.19 Zonal wind climatology of July simulated by WACCM

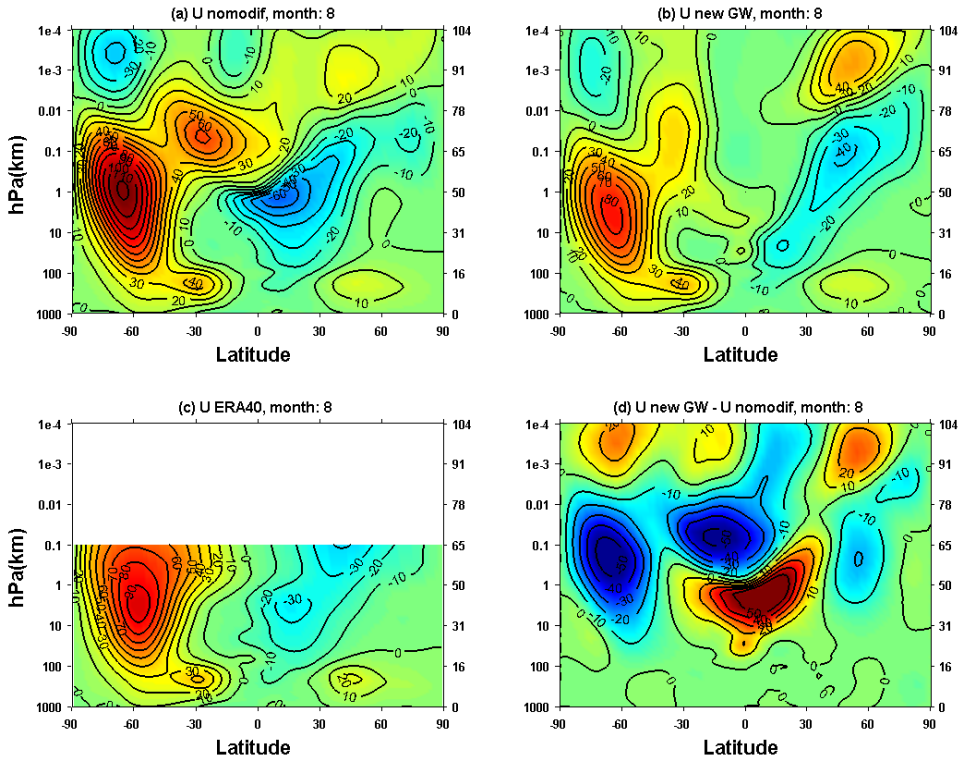

Figure A.20 Zonal wind climatology of August simulated by WACCM

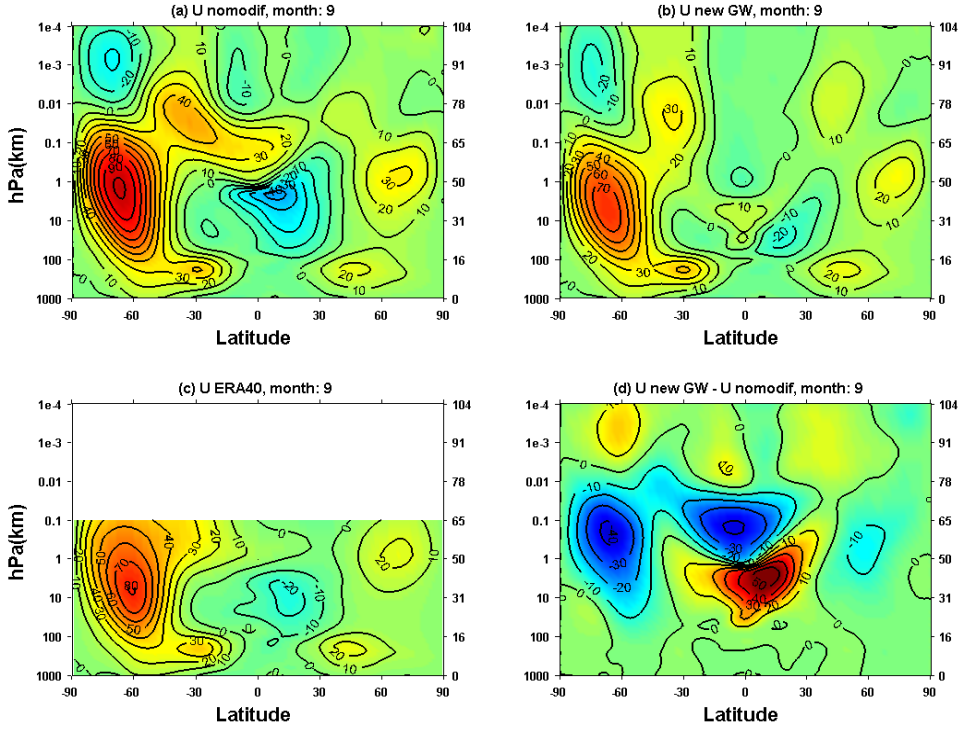

Figure A.21 Zonal wind climatology of September simulated by WACCM

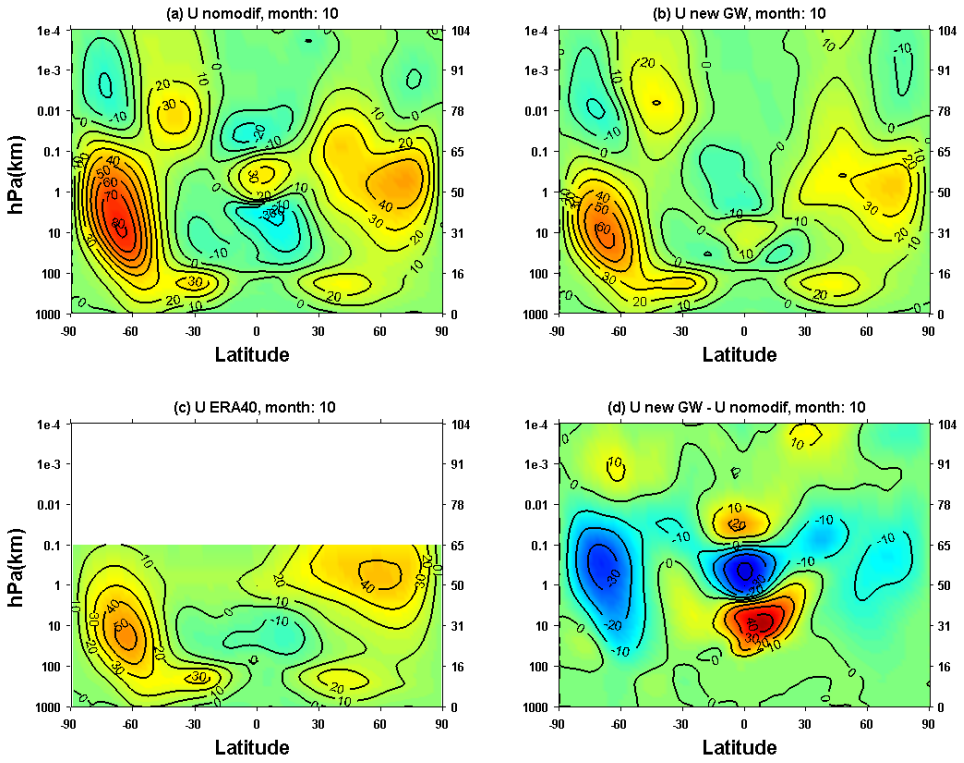

Figure A.22 Zonal wind climatology of October simulated by WACCM

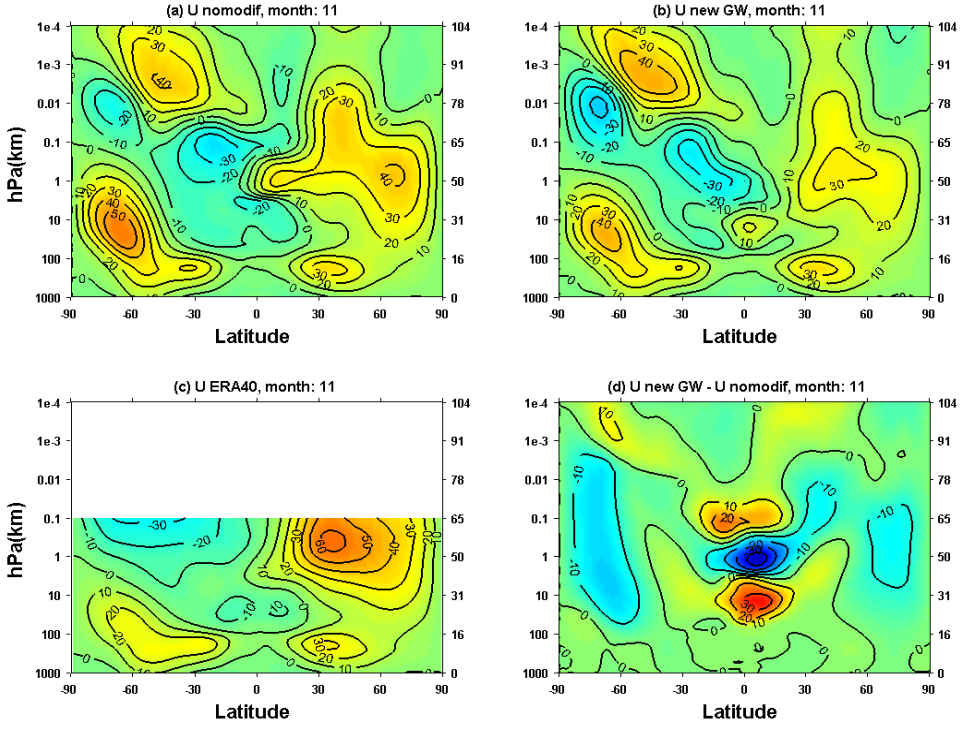

Figure A.23 Zonal wind climatology of November simulated by WACCM

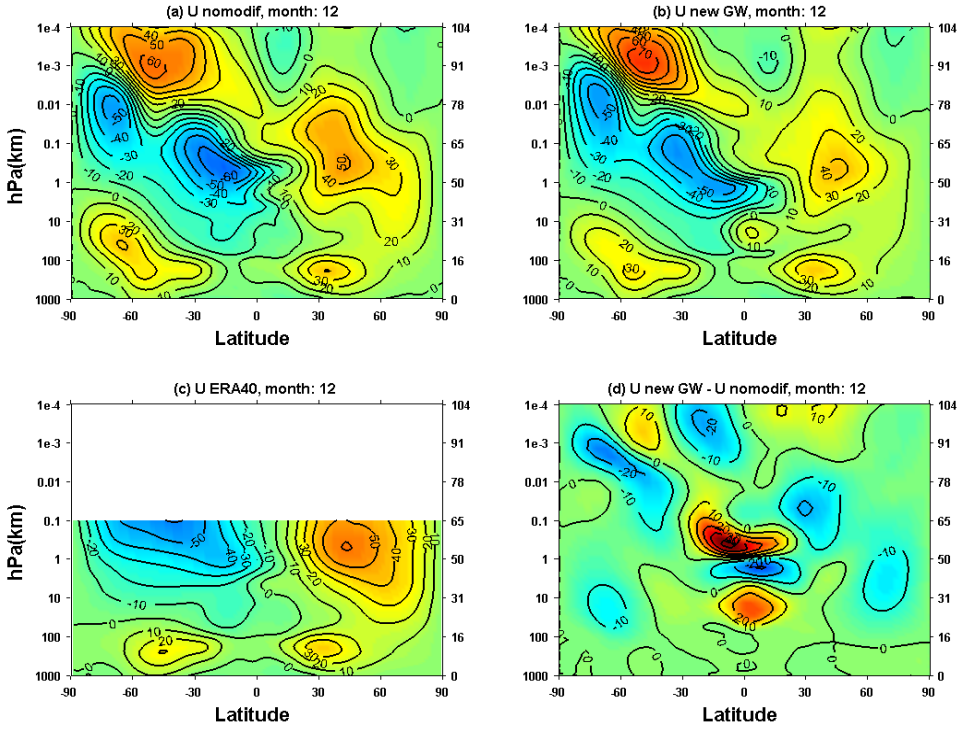

Figure A.24 Zonal wind climatology of December simulated by WACCM

Appendix B

In this appendix we show the wave forcing up to 1e-4 hPa simulated by WACCM with and without IGW scheme month by month.

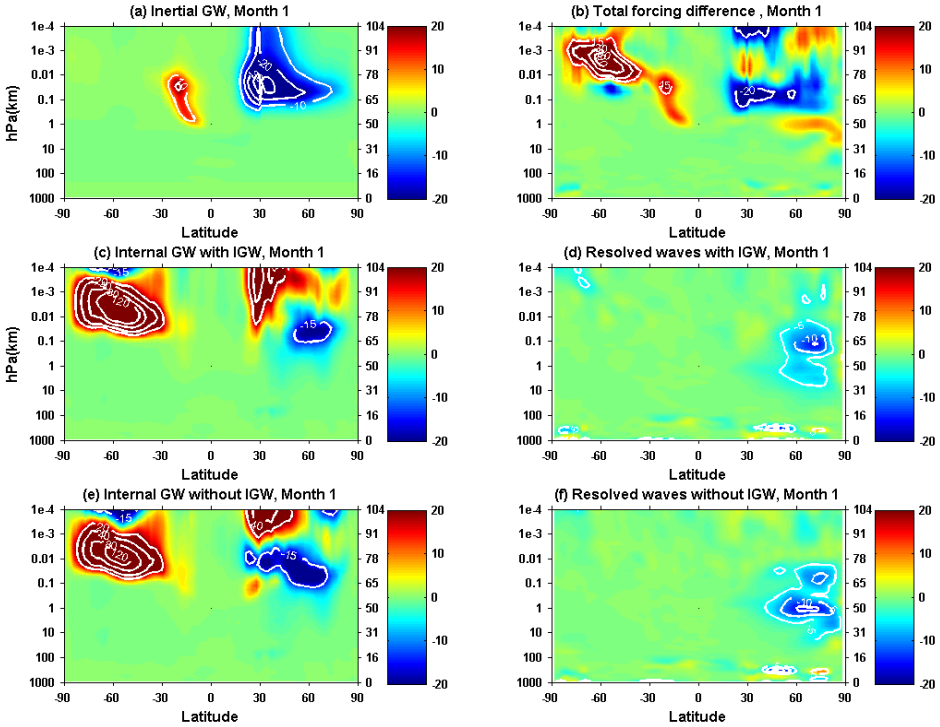

Figure B.1 Similar to Figure 4.11, for January

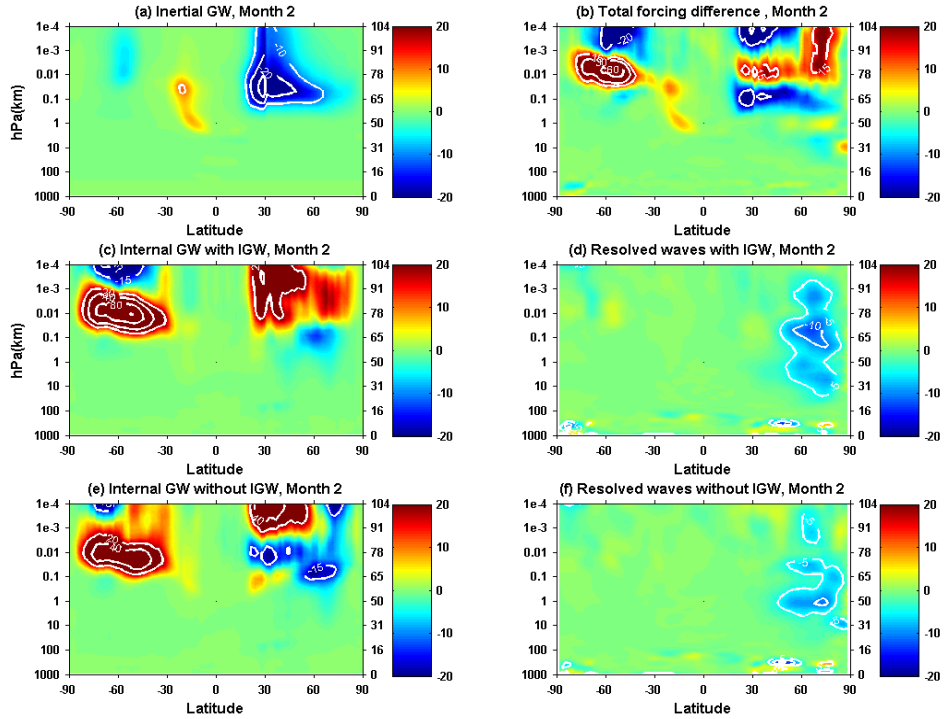

Figure B.2 Similar to Figure 4.11, for February

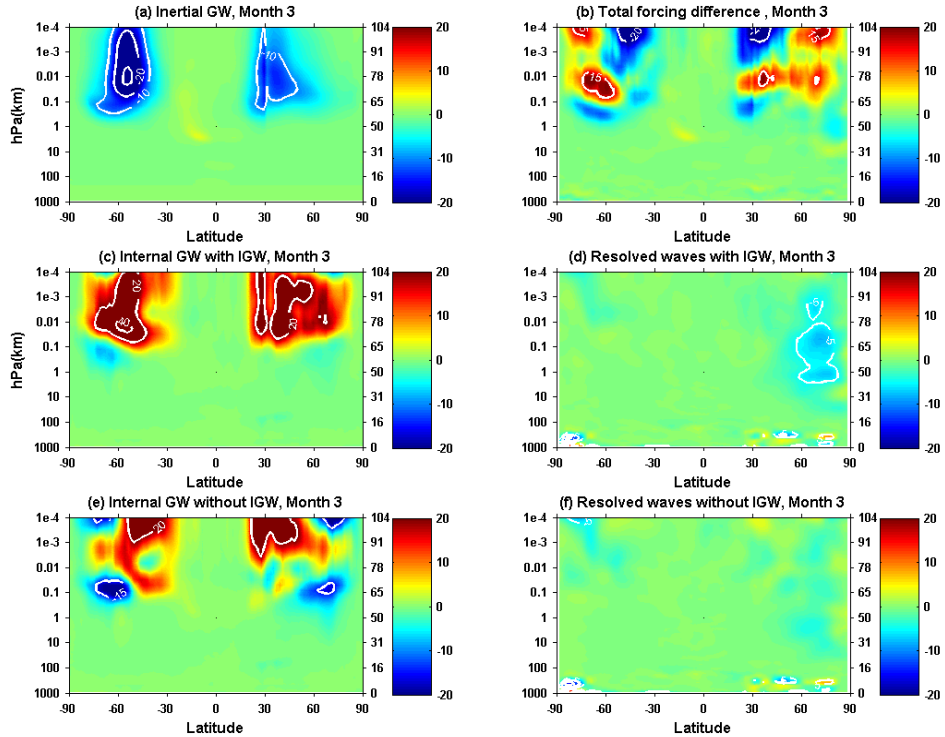

Figure B.3 Similar to Figure 4.11, for March

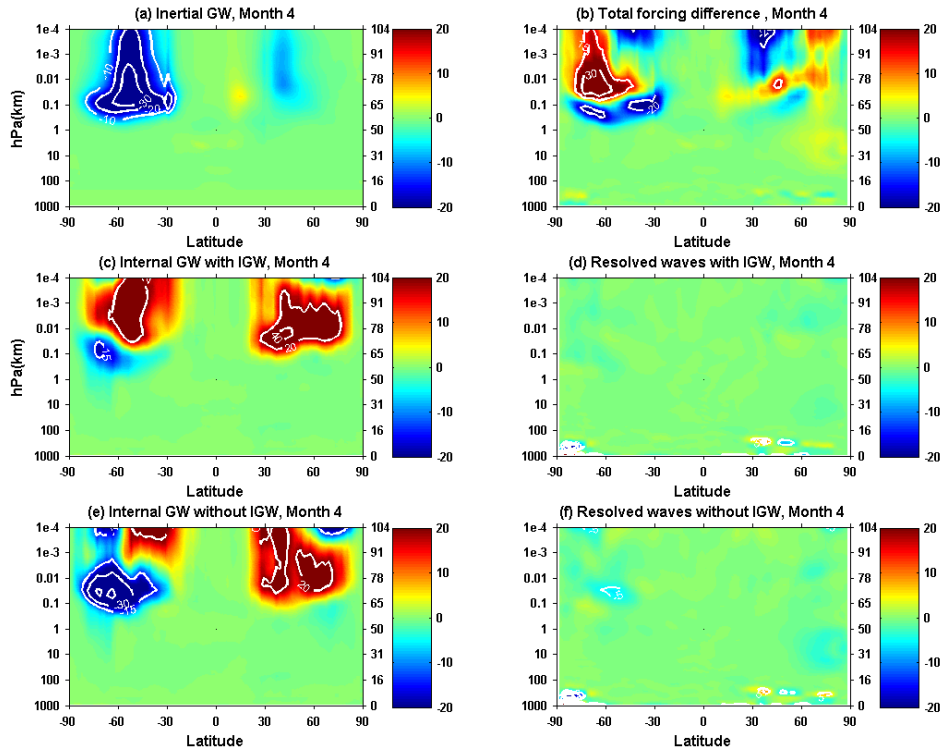

Figure B.4 Similar to Figure 4.11, for April

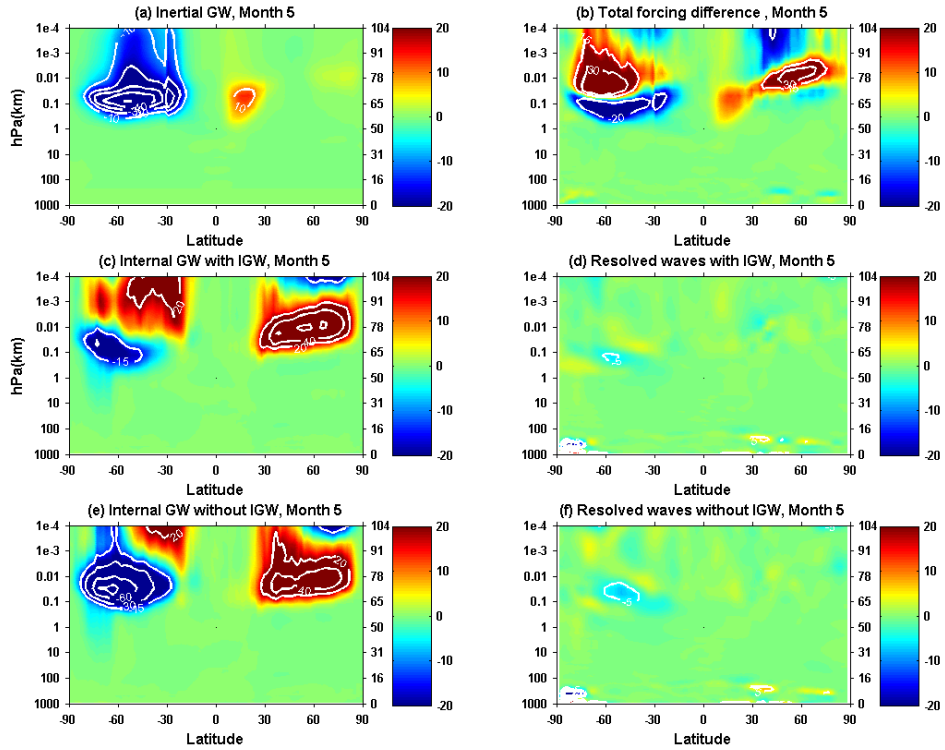

Figure B.5 Similar to Figure 4.11, for May

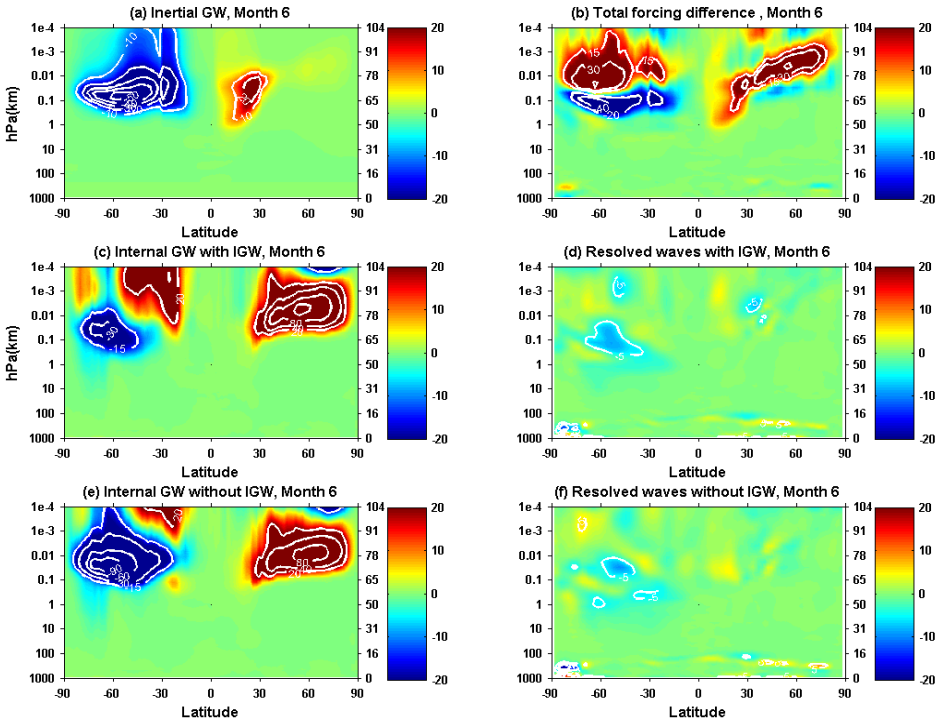

Figure B.6 Similar to Figure 4.11, for June

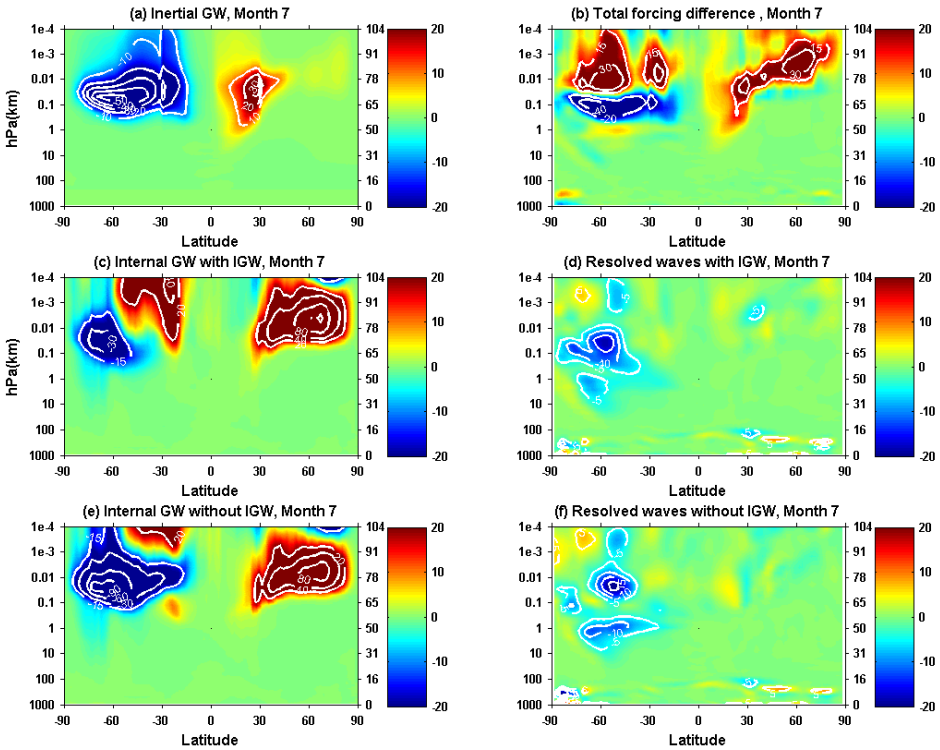

Figure B.7 Similar to Figure 4.11, for July

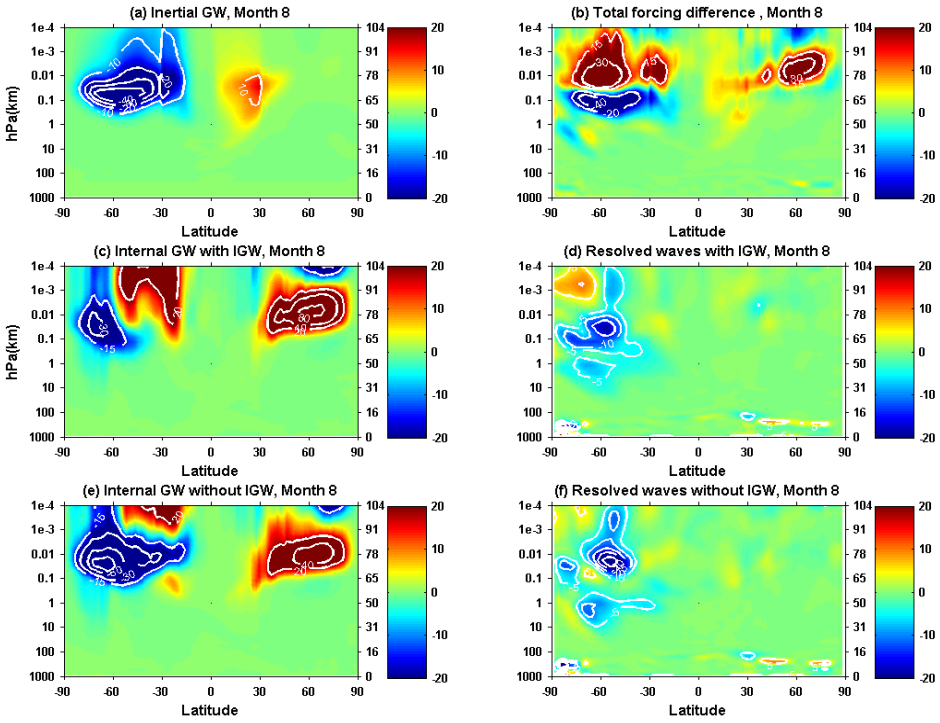

Figure B.8 Similar to Figure 4.11, for August

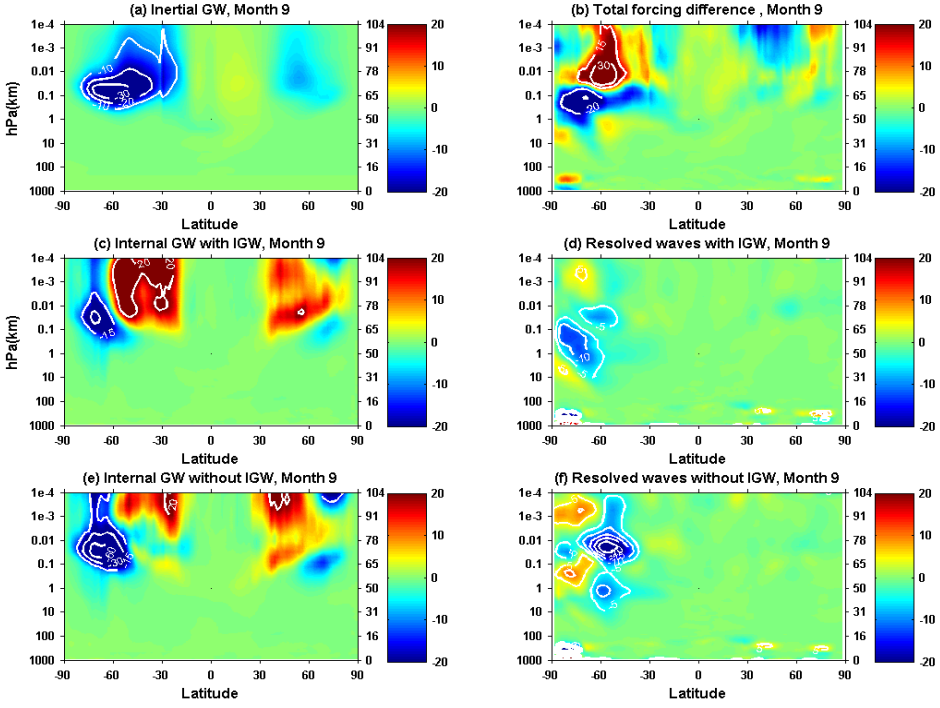

Figure B.9 Similar to Figure 4.11, for September

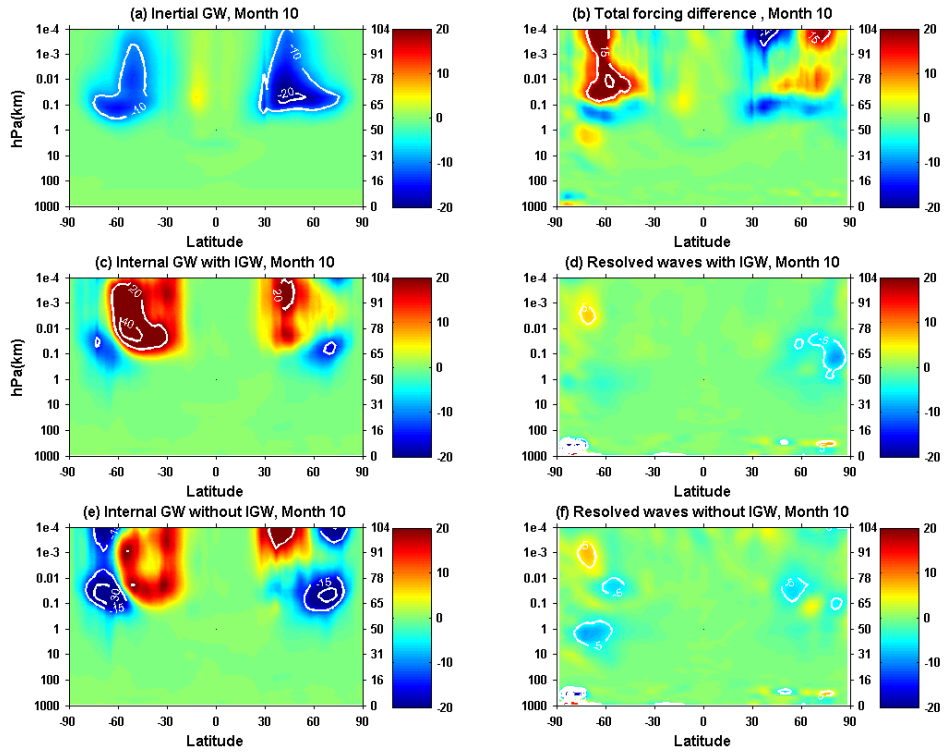

Figure B.10 Similar to Figure 4.11, for October

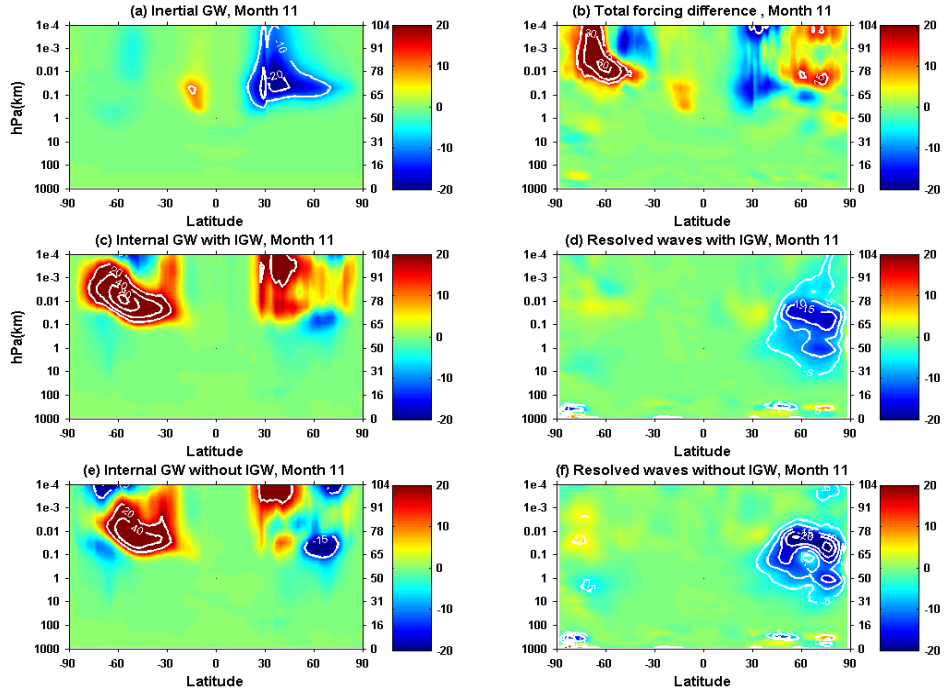

Figure B.11 Similar to Figure 4.11, for November

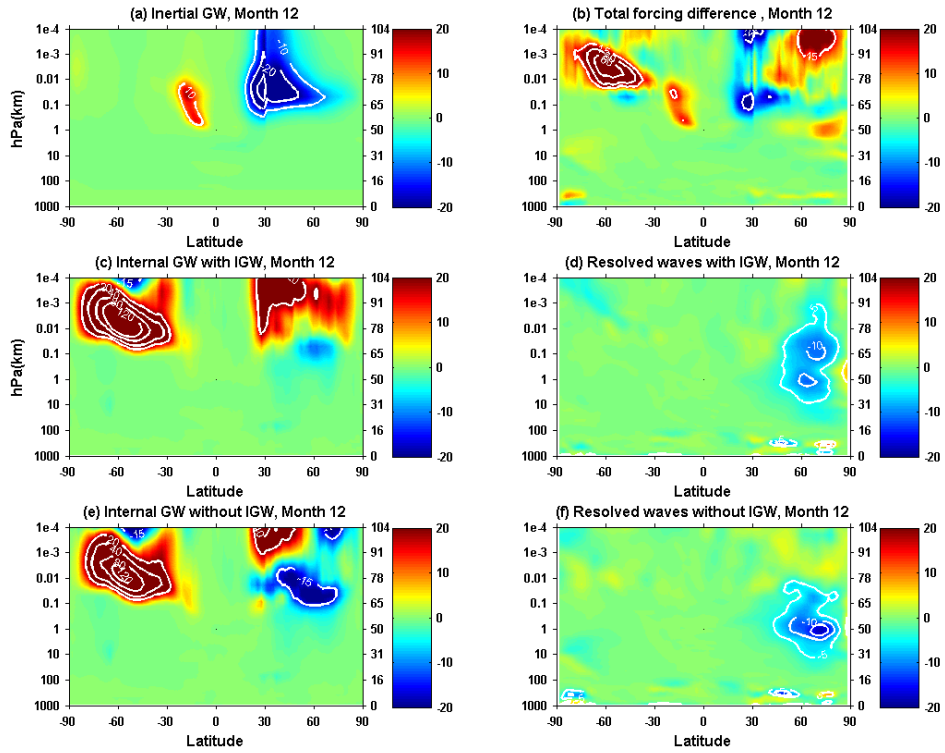

Figure B.12 Similar to Figure 4.11, for December

Appendix C

In this appendix we show the wave forcing difference up to 1e-4 hPa simulated by WACCM with and without IGW scheme month by month.

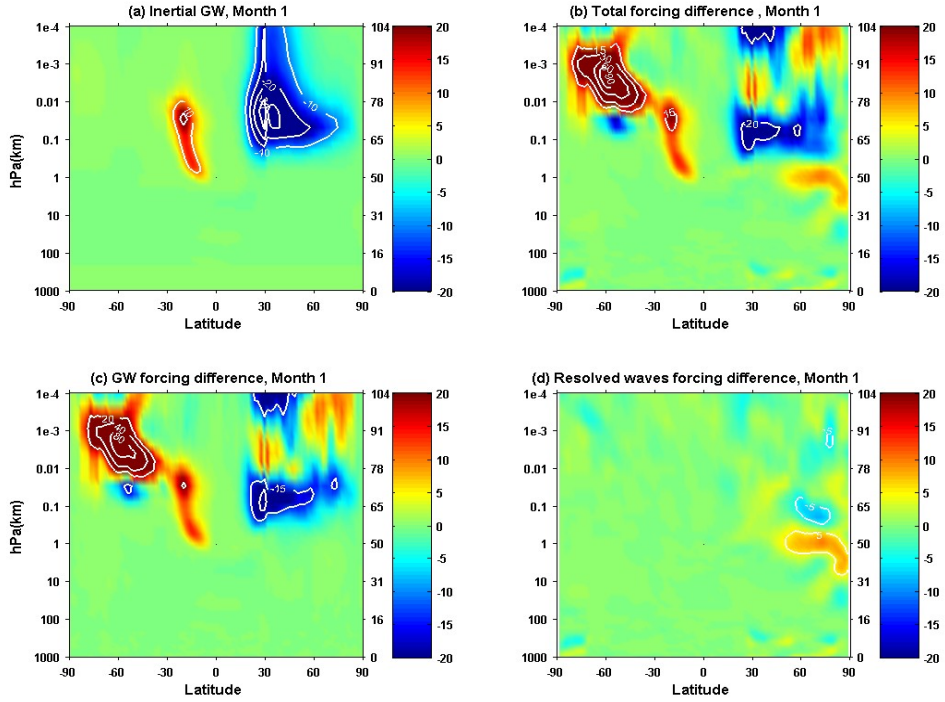

Figure C.1 Similar to Figure 4.12, for January

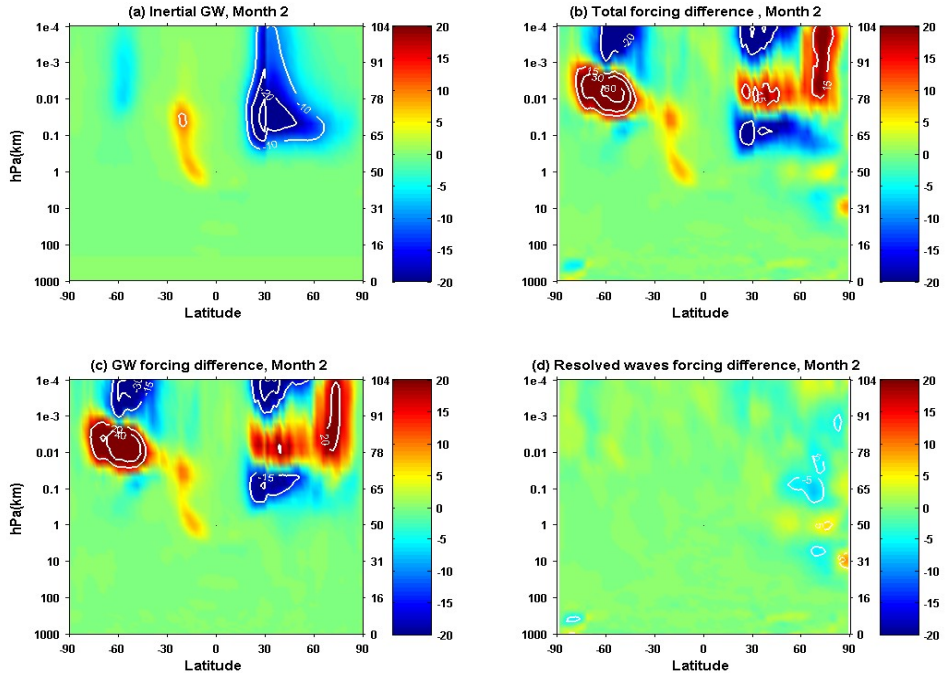

Figure C.2 Similar to Figure 4.12, for February

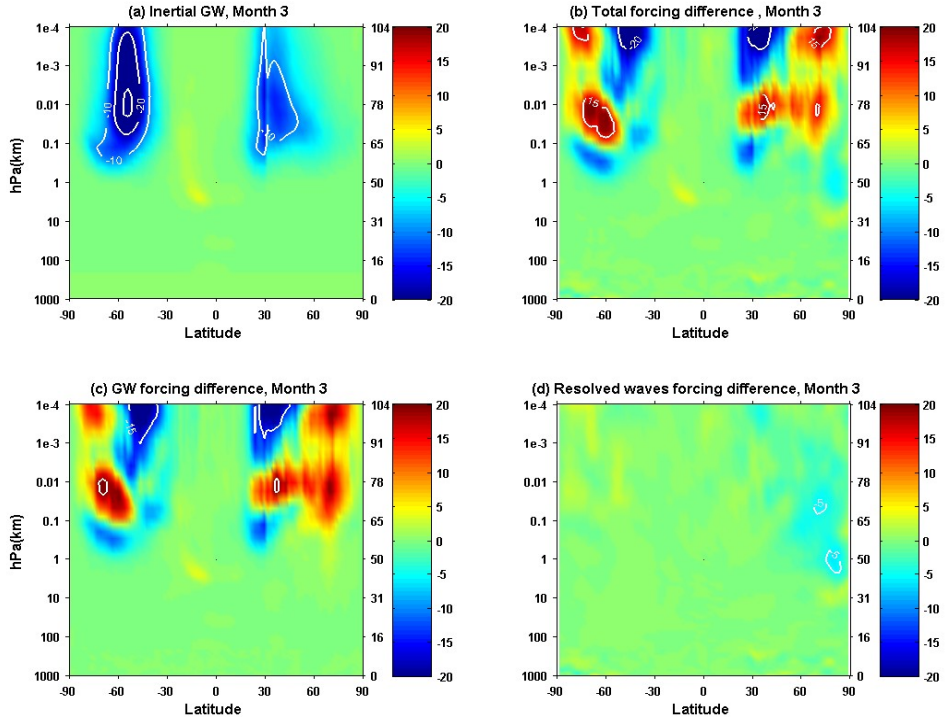

Figure C.3 Similar to Figure 4.12, for March

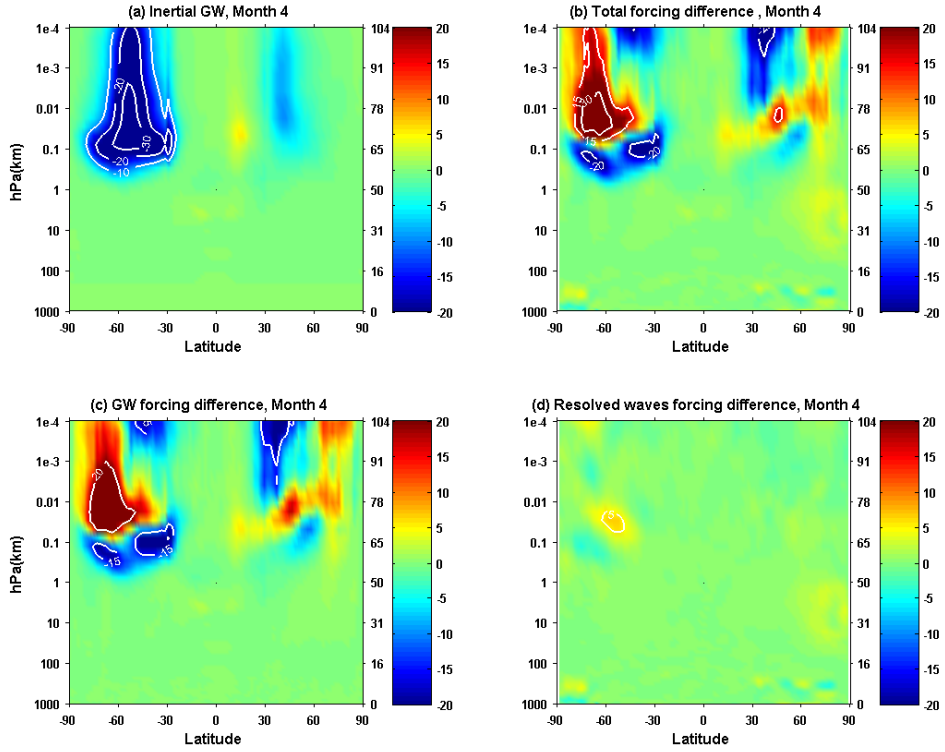

Figure C.4 Similar to Figure 4.12, for April

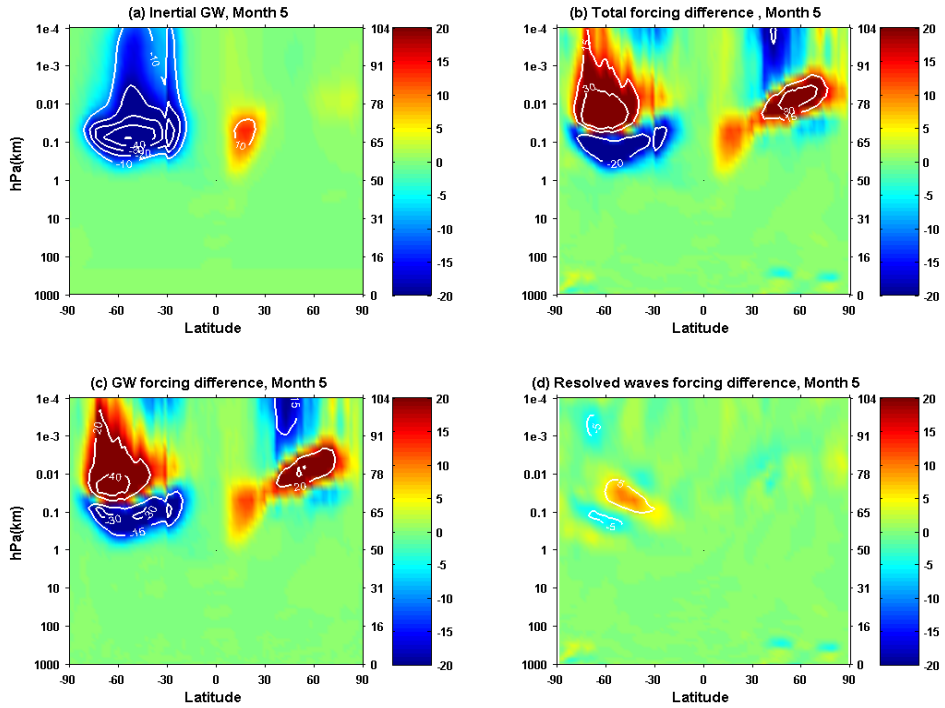

Figure C.5 Similar to Figure 4.12, for May

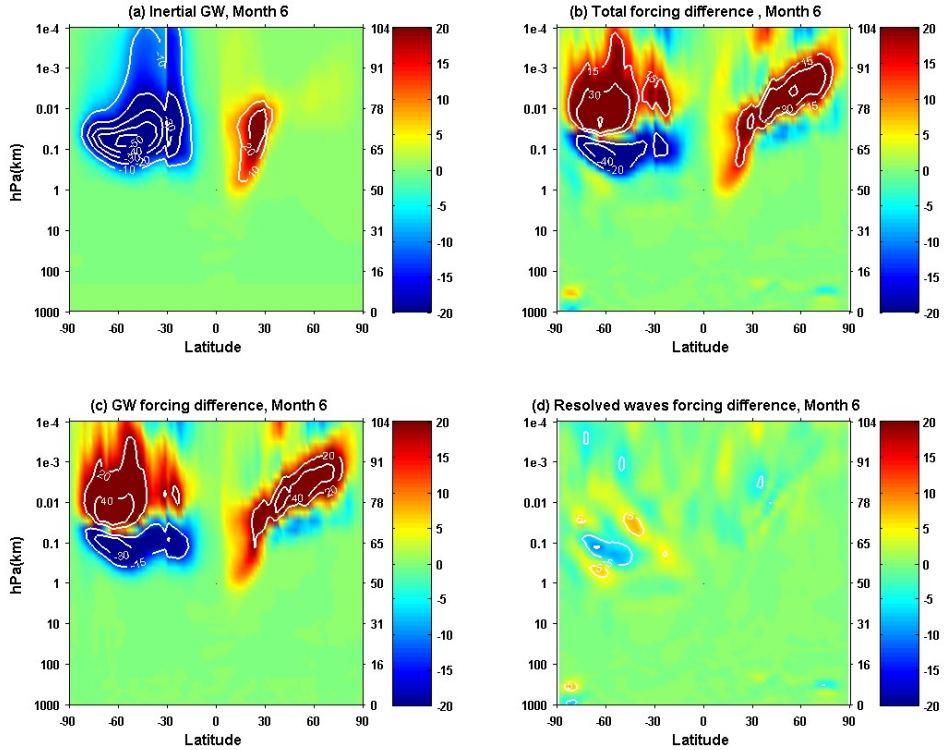

Figure C.6 Similar to Figure 4.12, for June

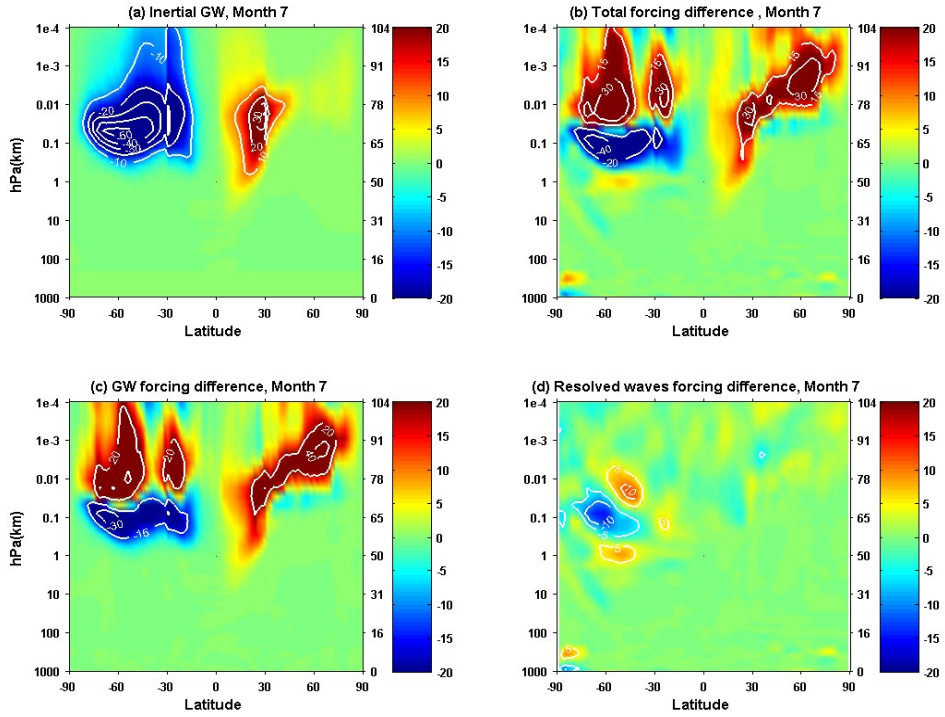

Figure C.7 Similar to Figure 4.12, for July

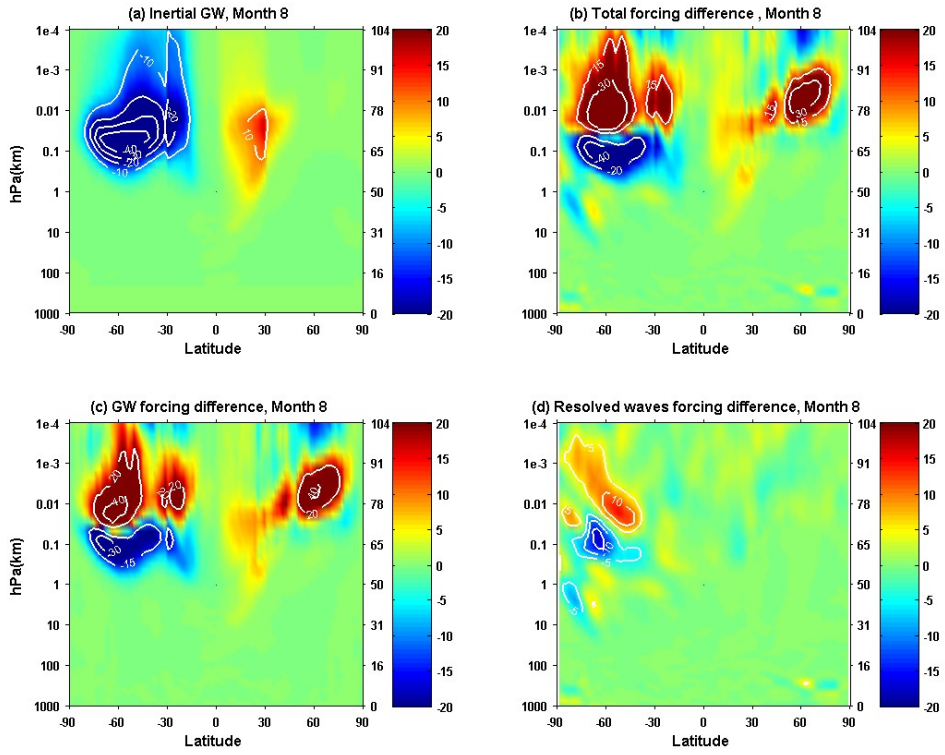

Figure C.8 Similar to Figure 4.12, for August

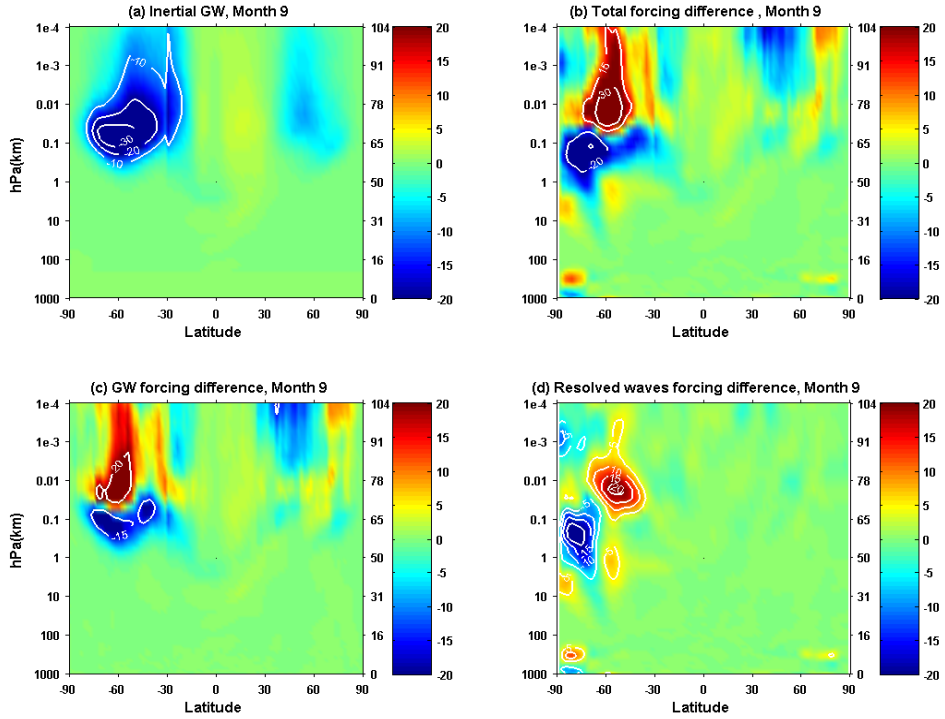

Figure C.9 Similar to Figure 4.12, for September

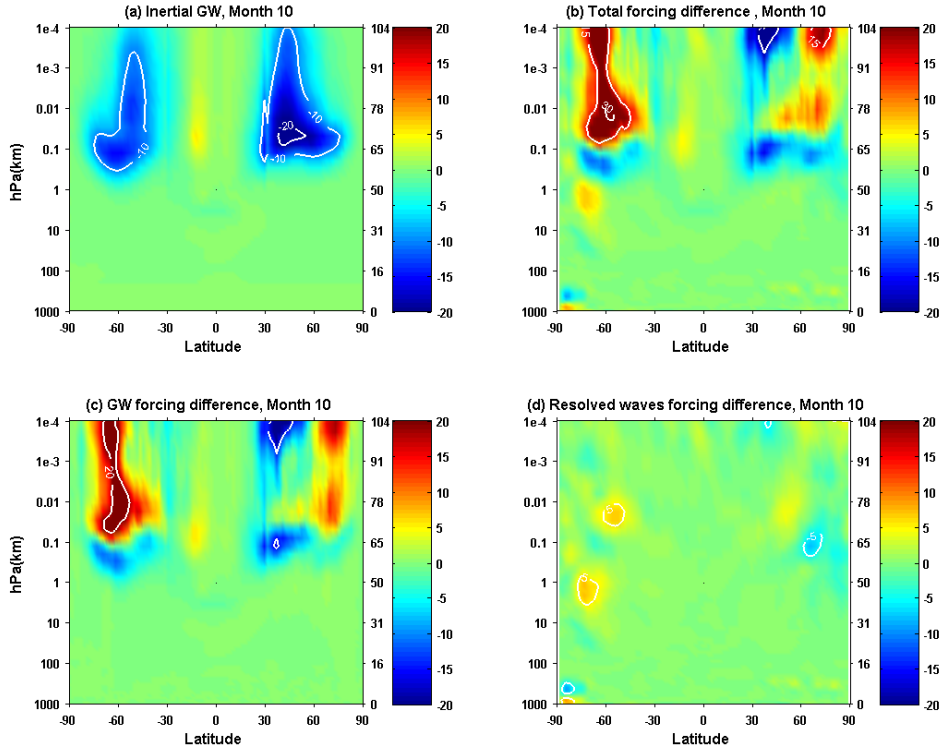

Figure C.10 Similar to Figure 4.12, for October

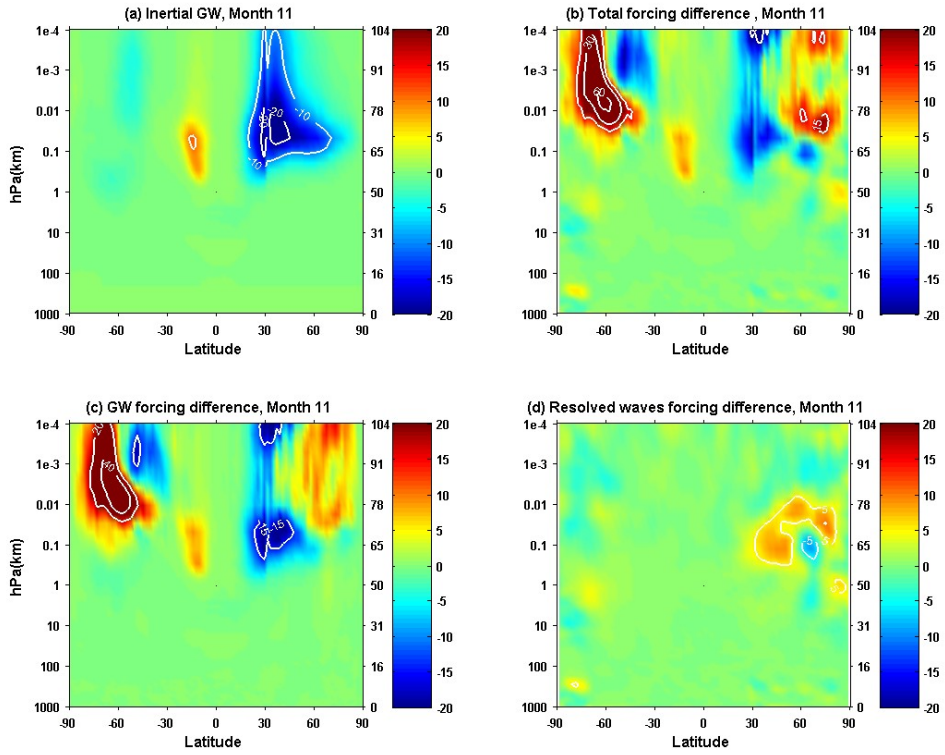

Figure C.11 Similar to Figure 4.12, for November

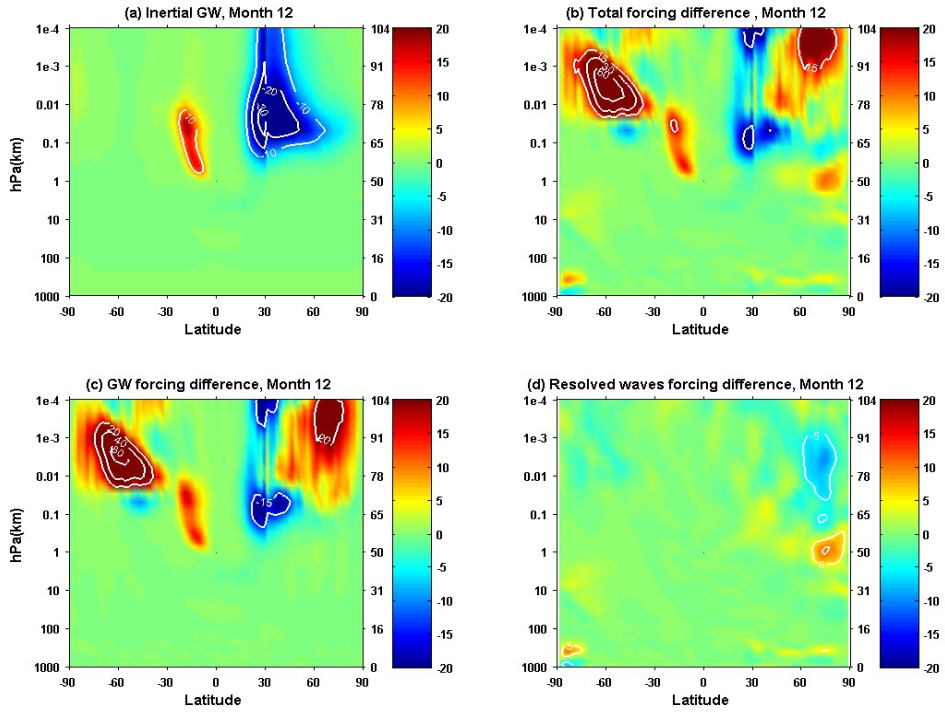

Figure C.12 Similar to Figure 4.12, for December

Appendix D

In this appendix we show the wave forcing up to 0.1 hPa simulated by WACCM with and without IGW scheme month by month.

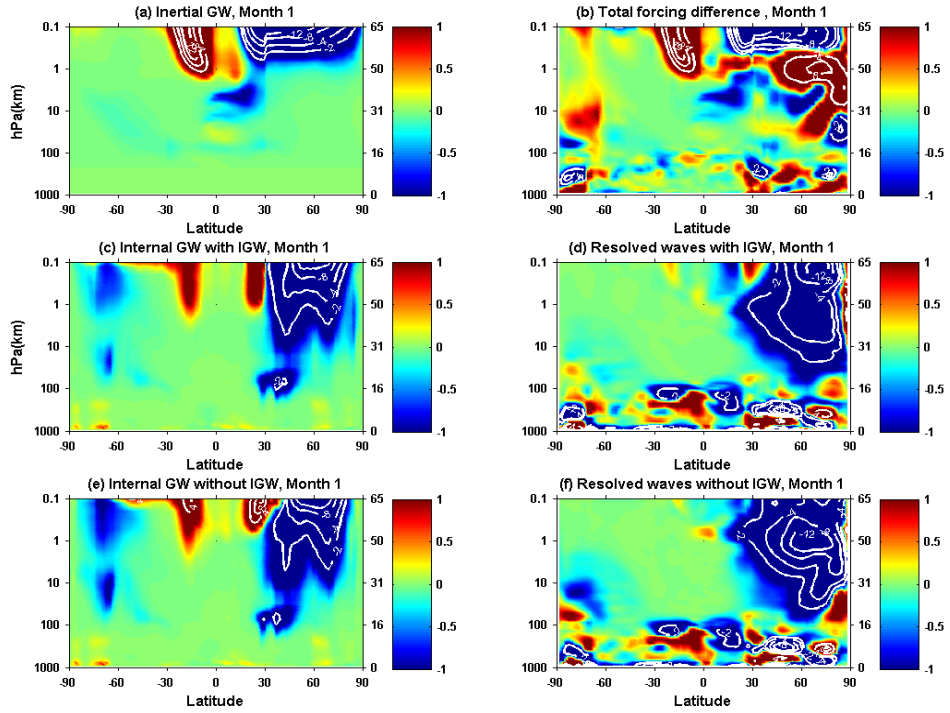

Figure D.1 Similar to Figure 4.13, for January

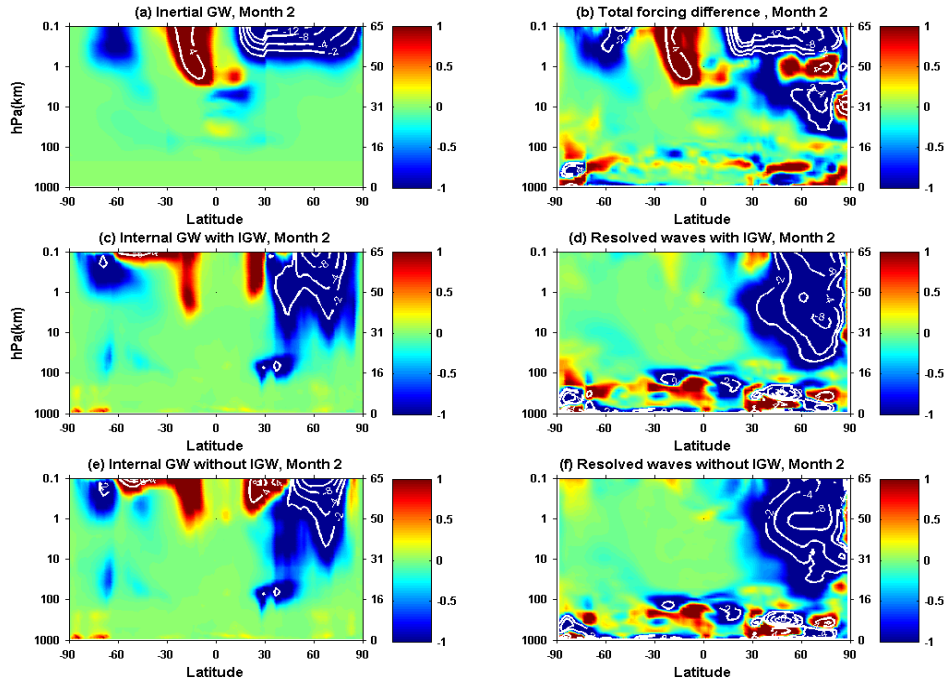

Figure D.2 Similar to Figure 4.13, for February

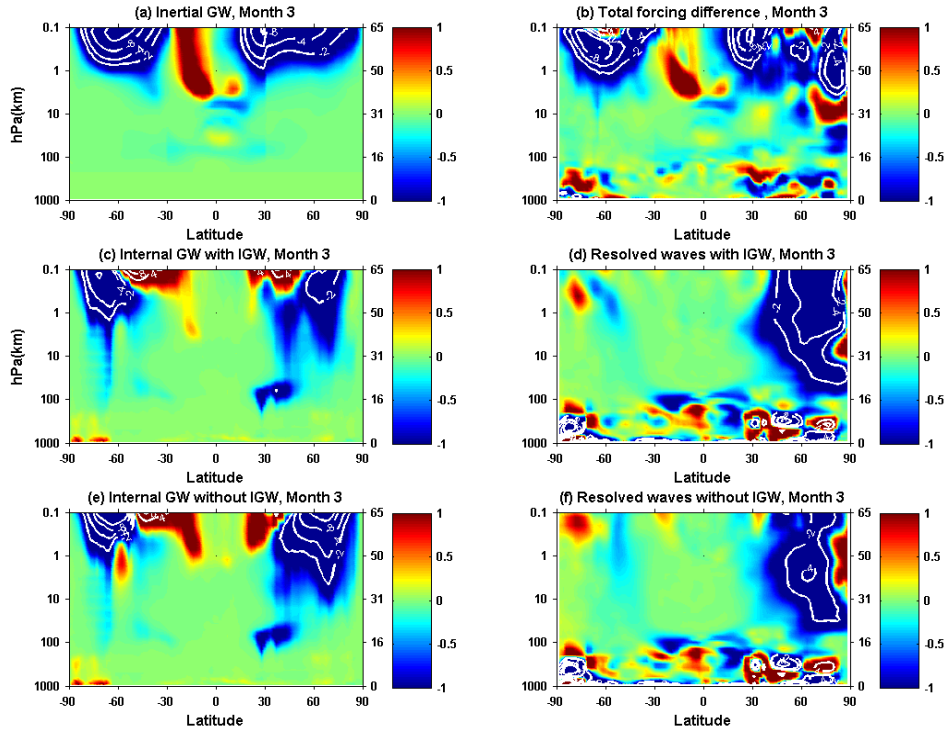

Figure D.3 Similar to Figure 4.13, for March

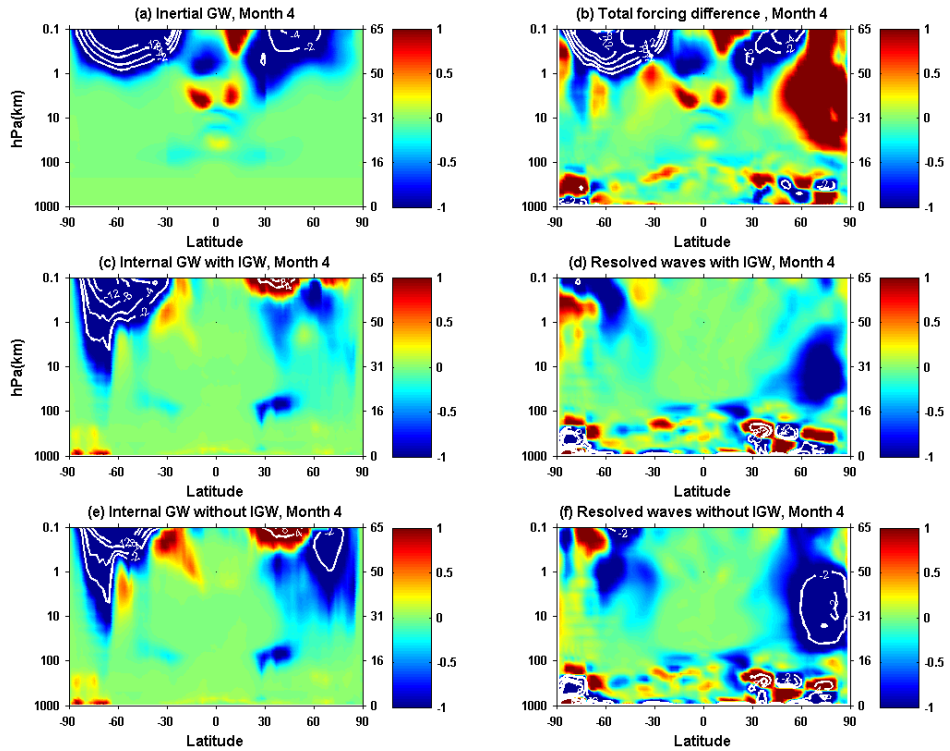

Figure D.4 Similar to Figure 4.13, for April

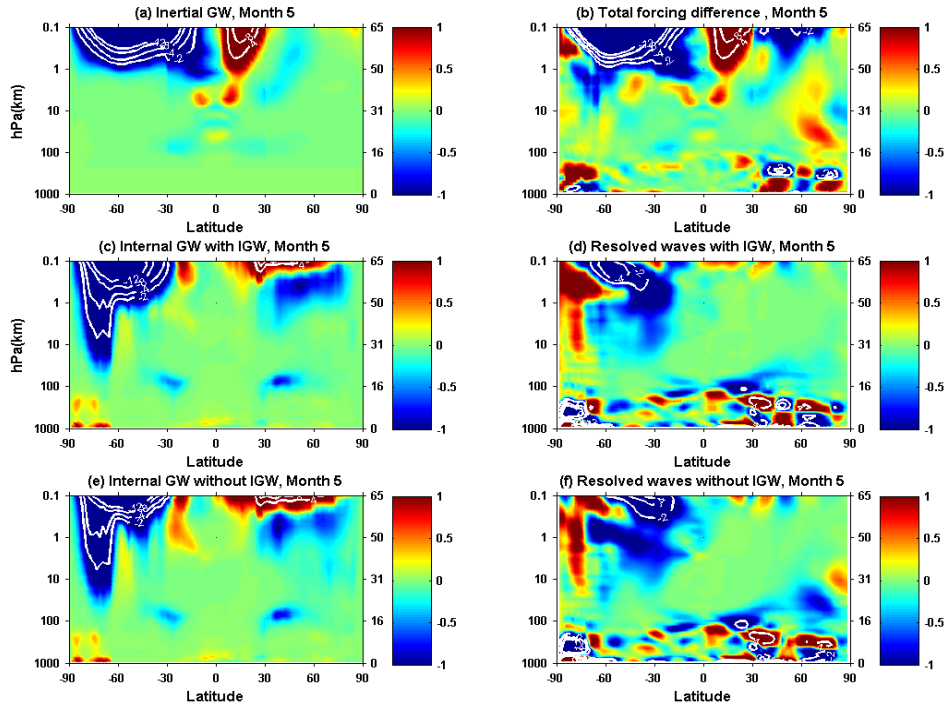

Figure D.5 Similar to Figure 4.13, for May

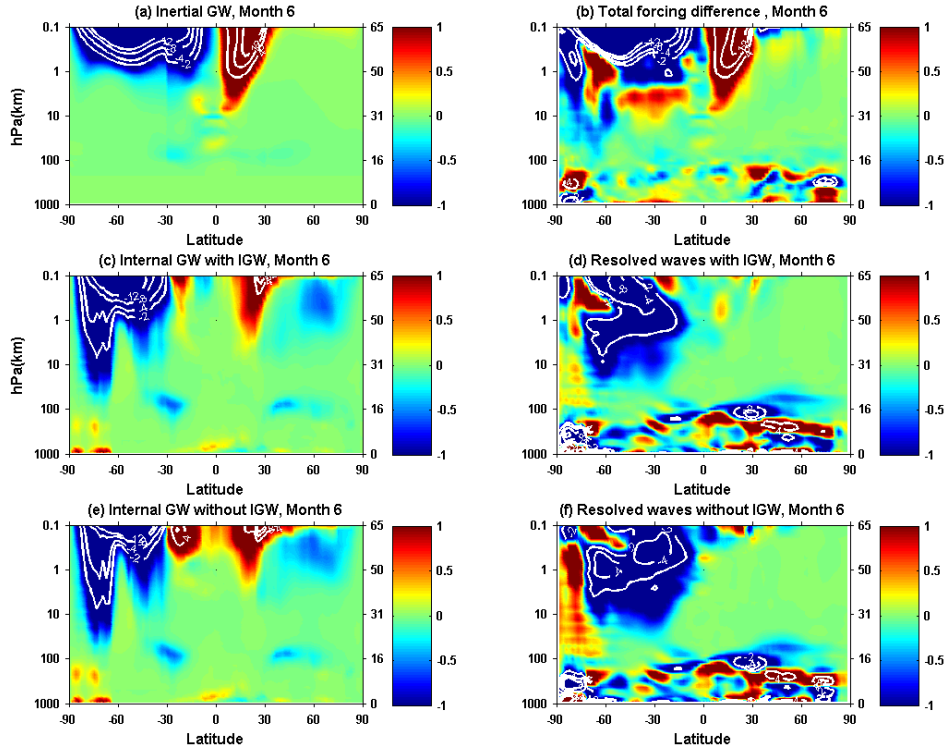

Figure D.6 Similar to Figure 4.13, for June

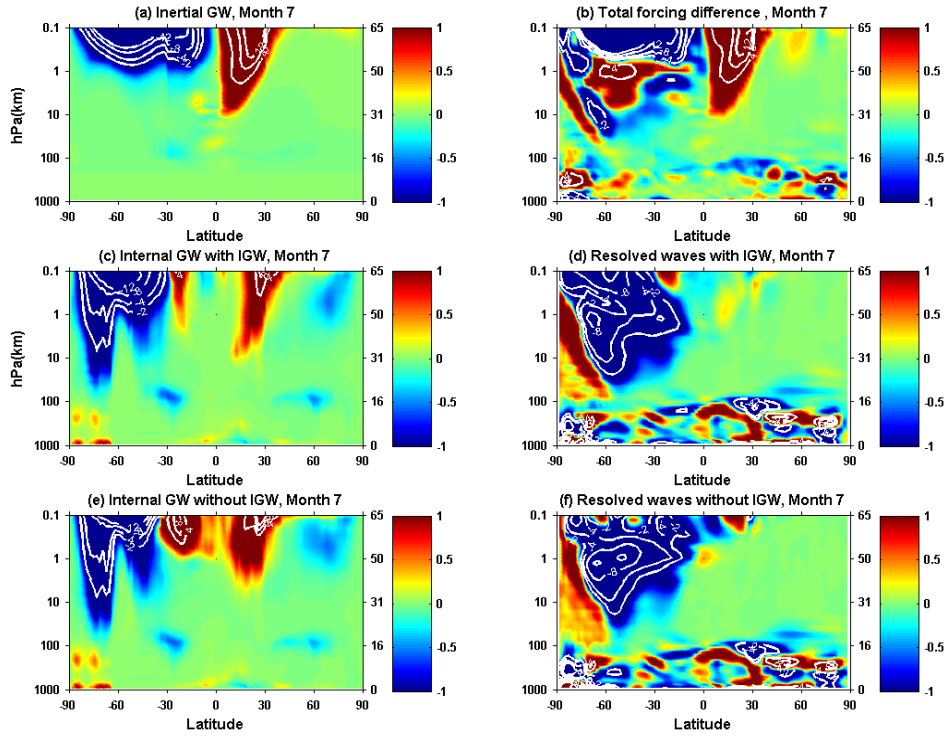

Figure D.7 Similar to Figure 4.13, for July

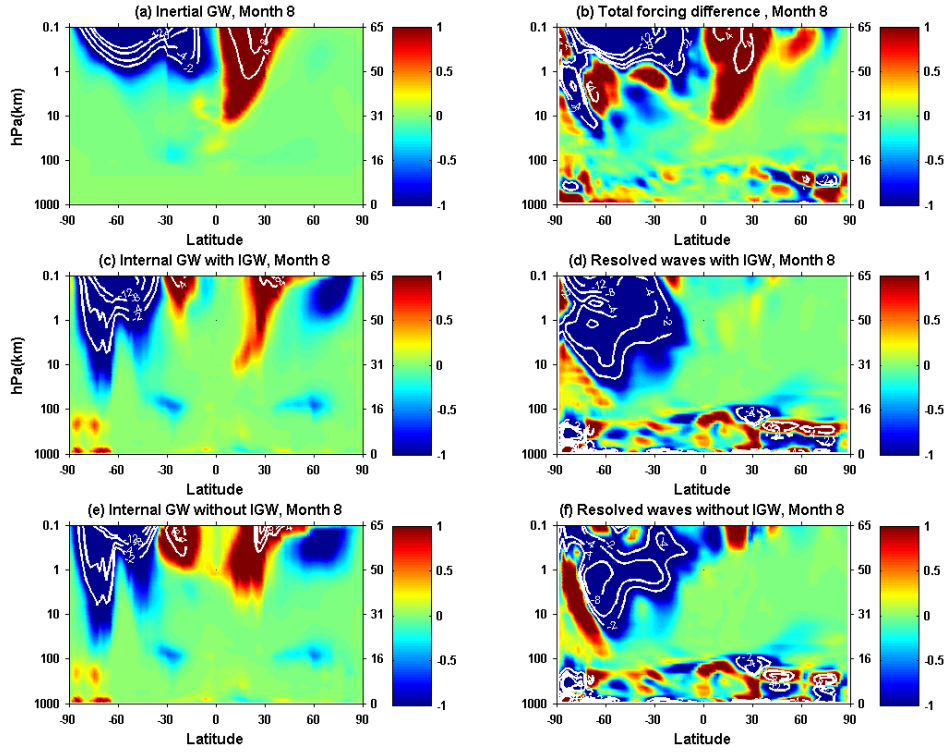

Figure D.8 Similar to Figure 4.13, for August

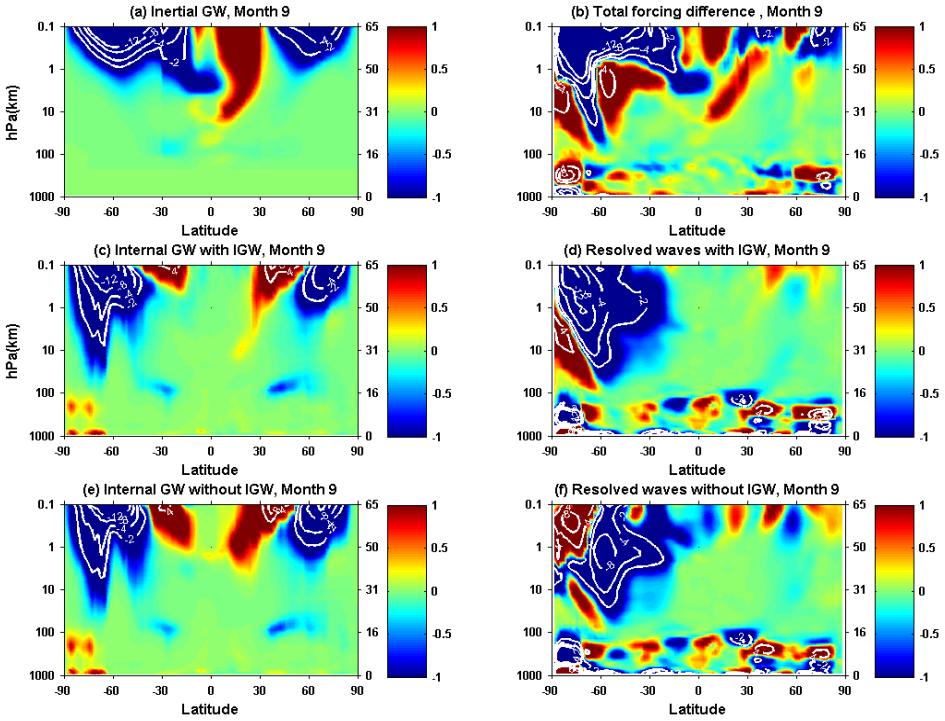

Figure D.9 Similar to Figure 4.13, for September

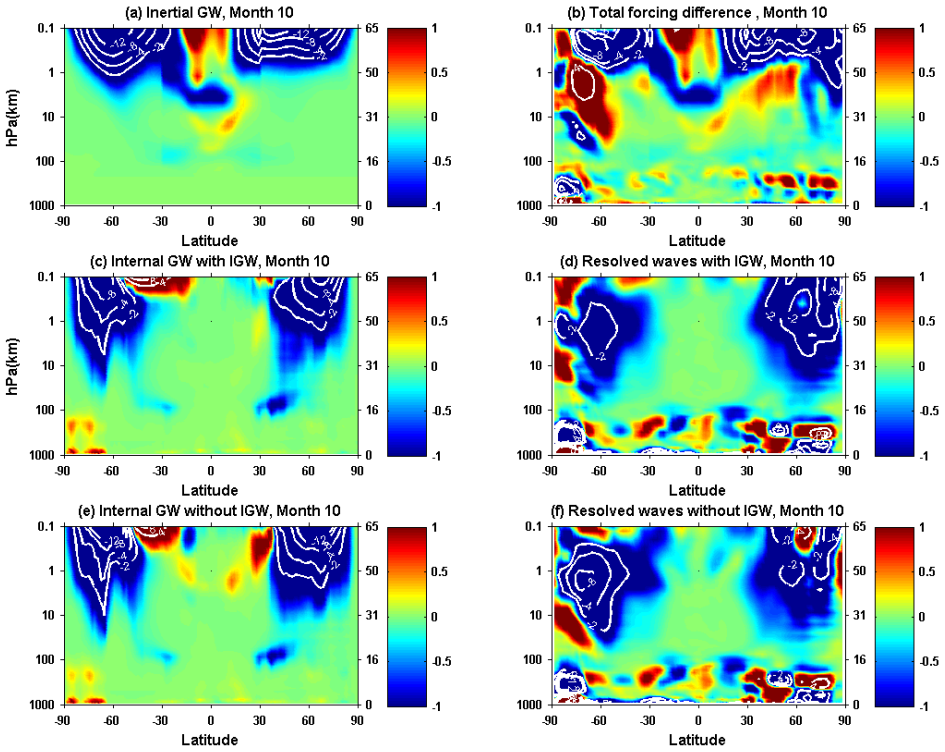

Figure D.10 Similar to Figure 4.13, for October

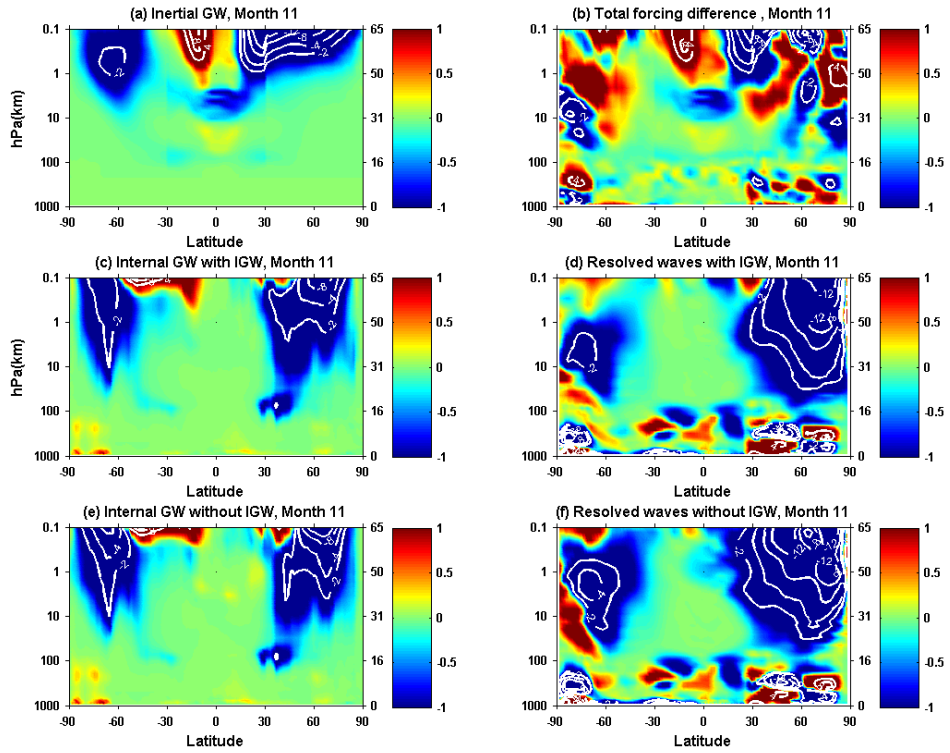

Figure D.11 Similar to Figure 4.13, for November

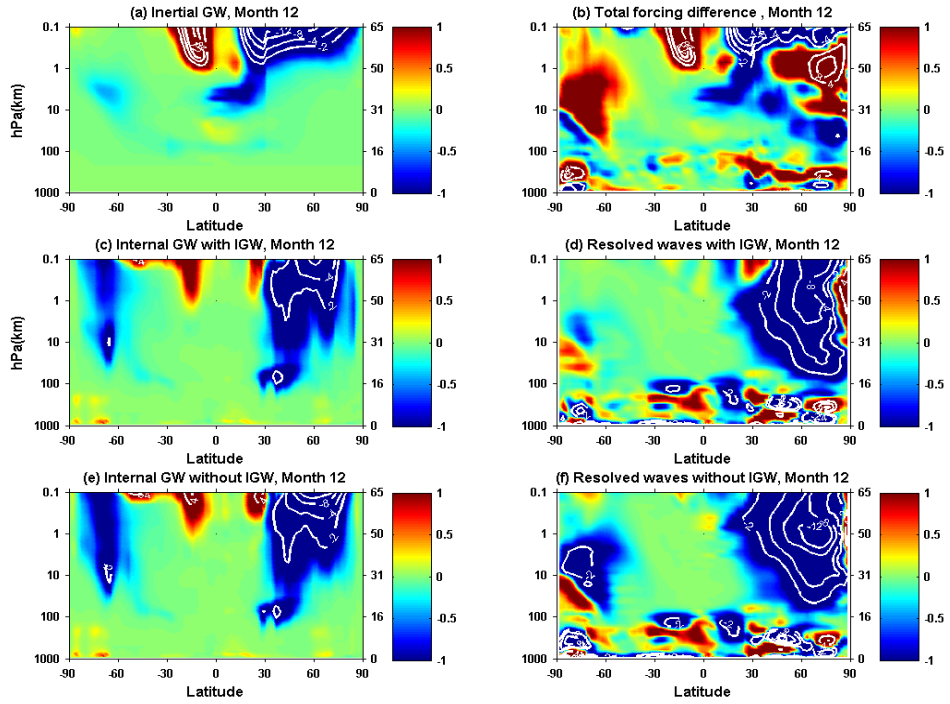

Figure D.12 Similar to Figure 4.13, for December

Appendix E

In this appendix we show the wave forcing difference up to 0.1 hPa simulated by WACCM with and without IGW scheme month by month.

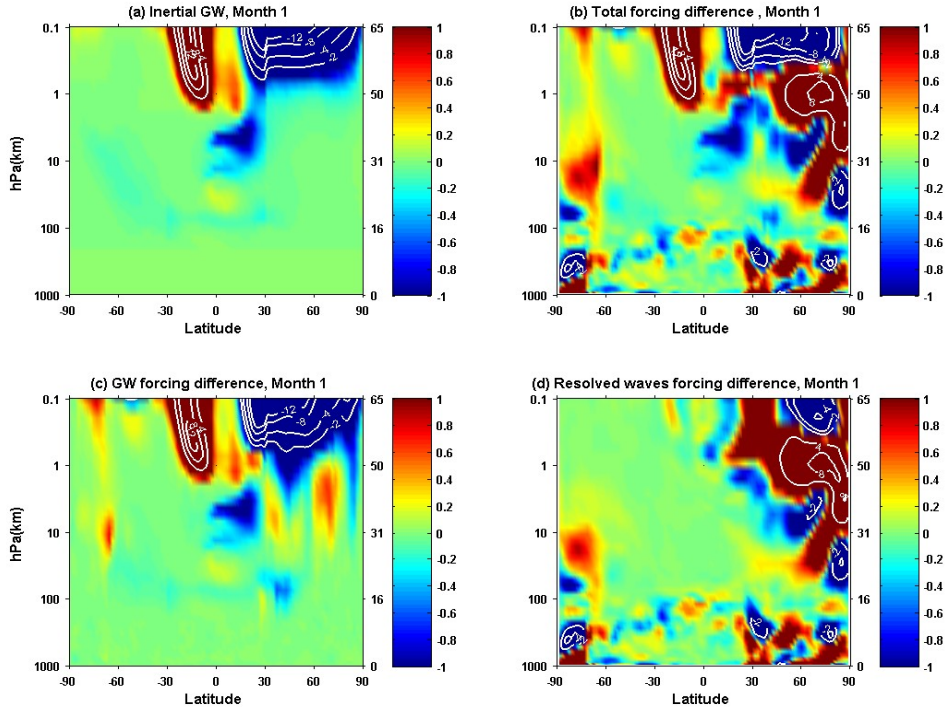

Figure E.1 Similar to Figure 4.14, for January

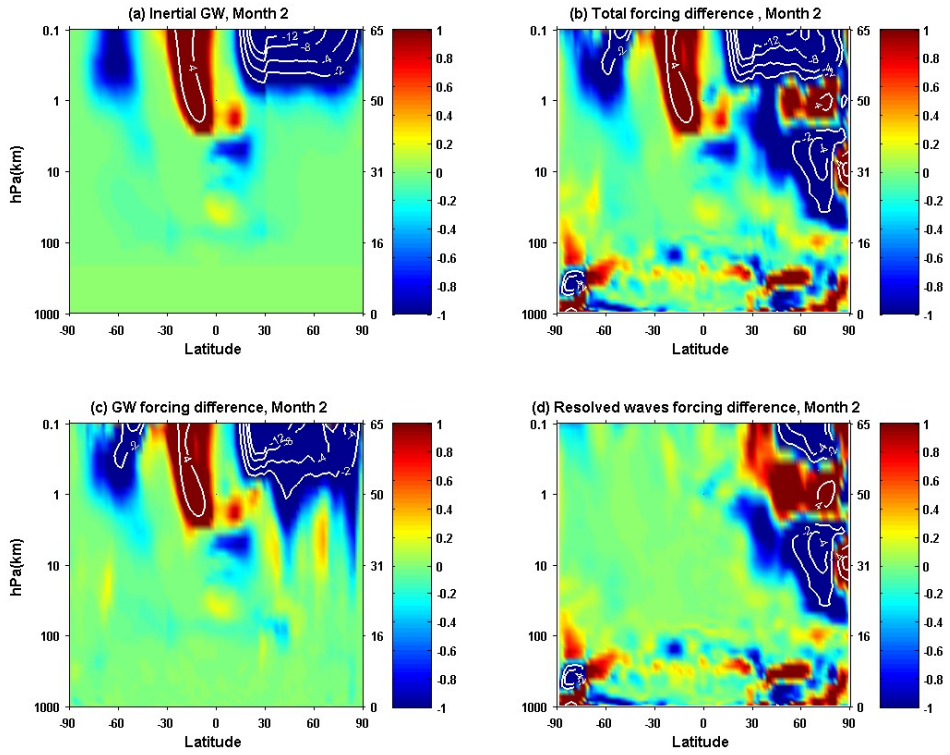

Figure E.2 Similar to Figure 4.14, for February

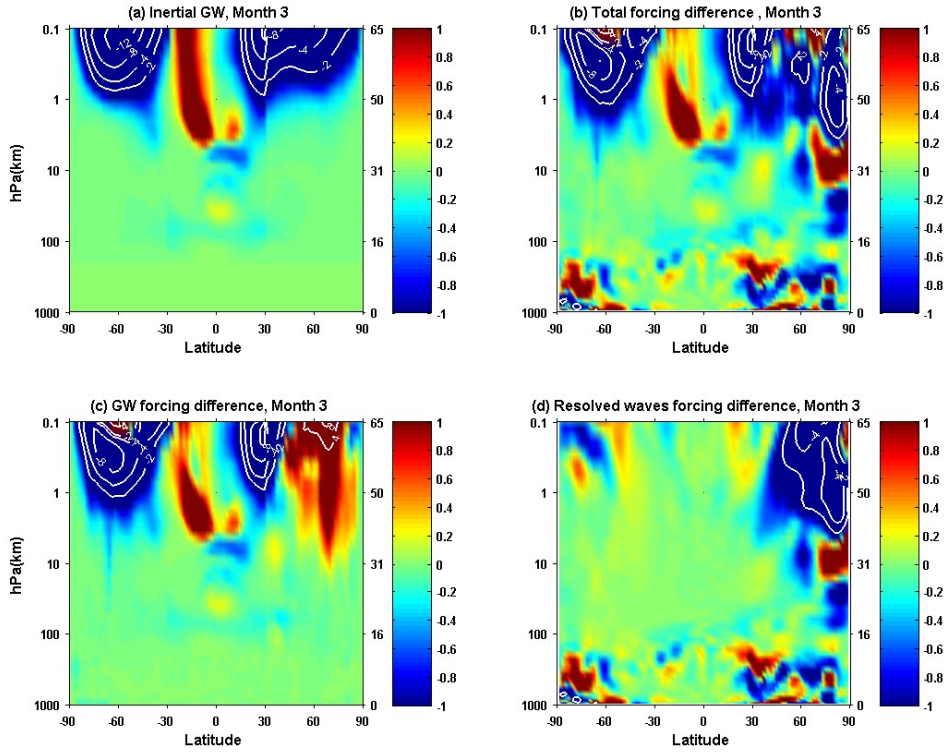

Figure E.3 Similar to Figure 4.14, for March

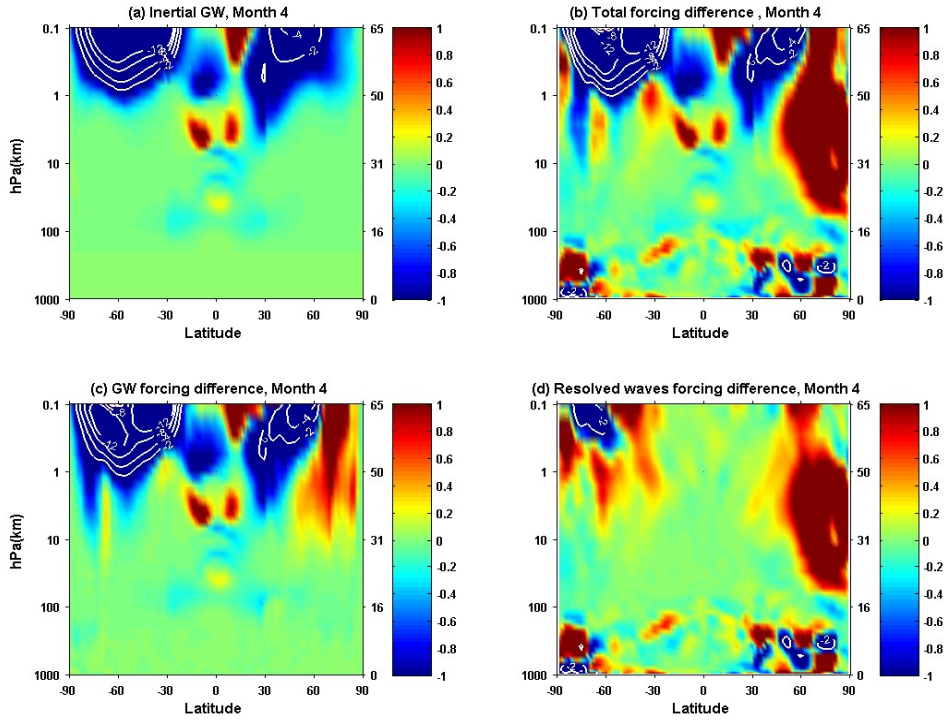

Figure E.4 Similar to Figure 4.14, for April

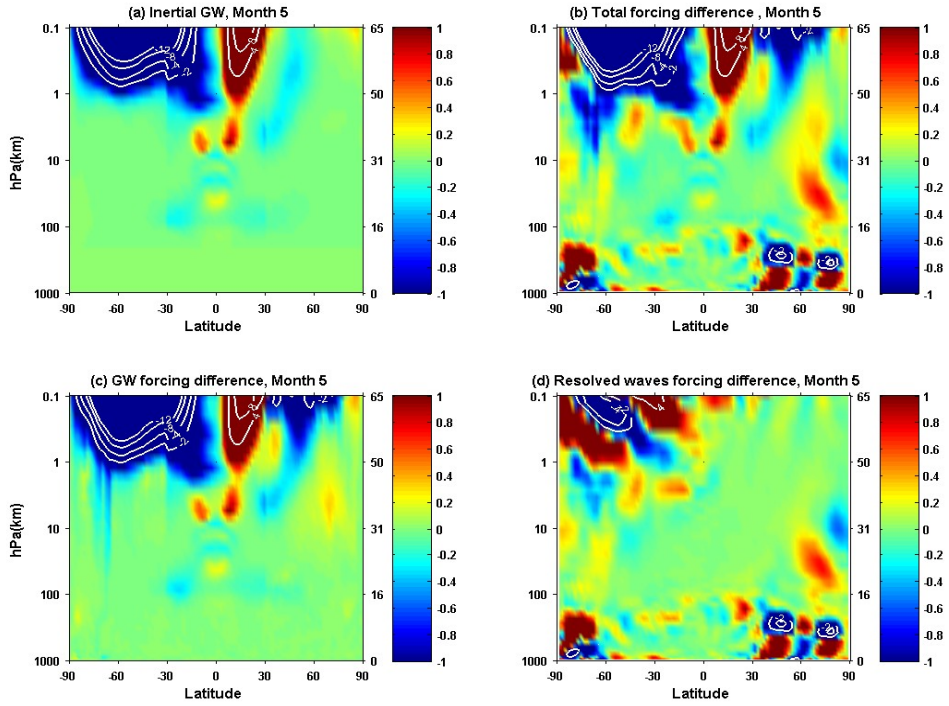

Figure E.5 Similar to Figure 4.14, for May

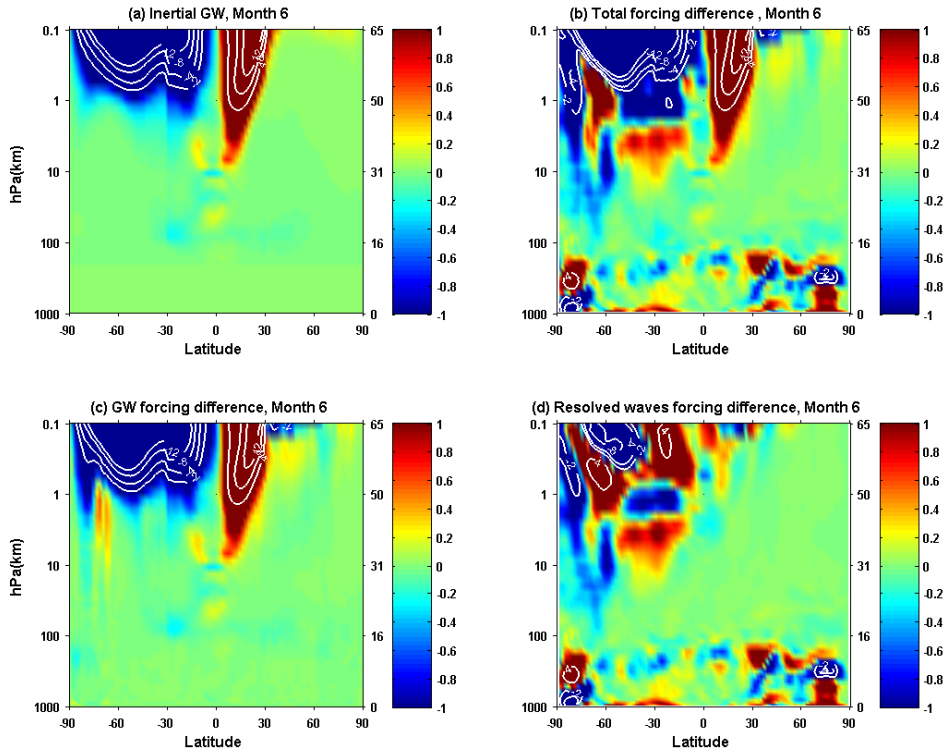

Figure E.6 Similar to Figure 4.14, for June

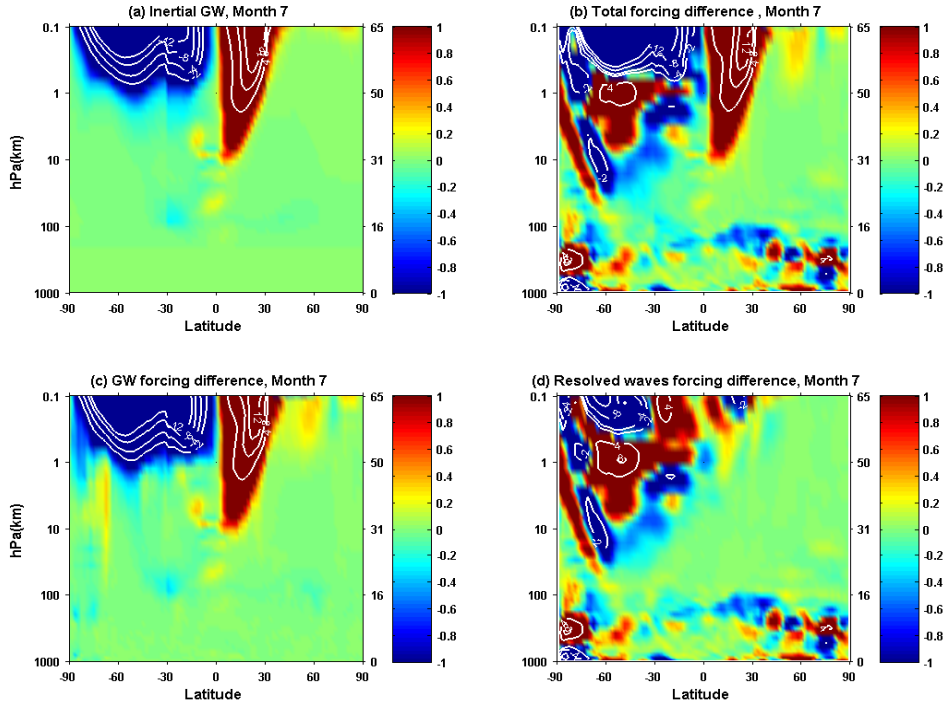

Figure E.7 Similar to Figure 4.14, for July

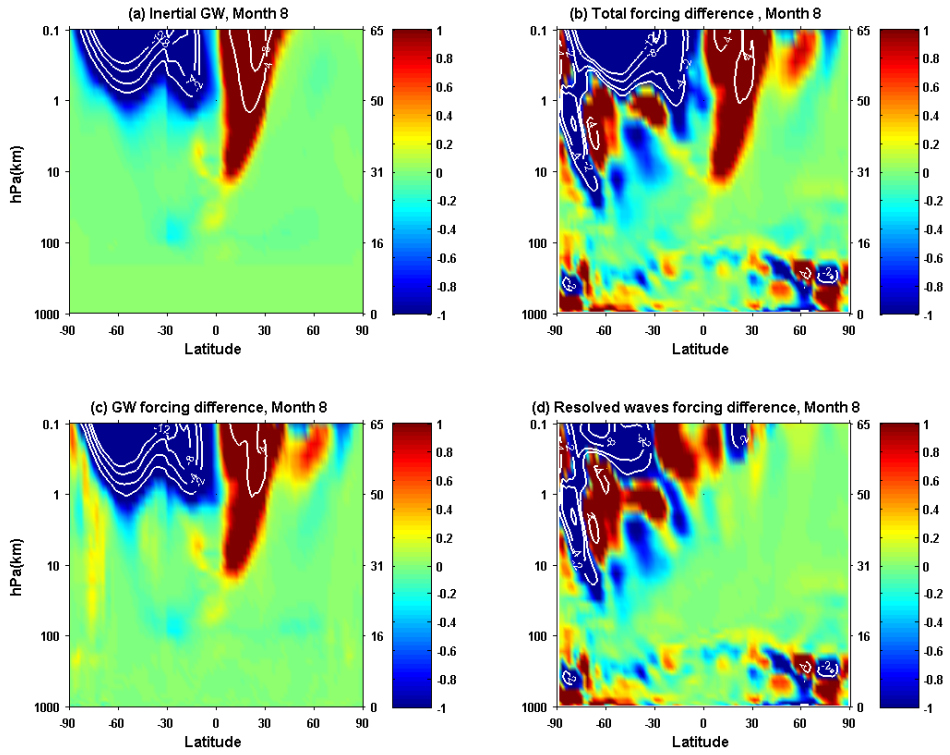

Figure E.8 Similar to Figure 4.14, for August

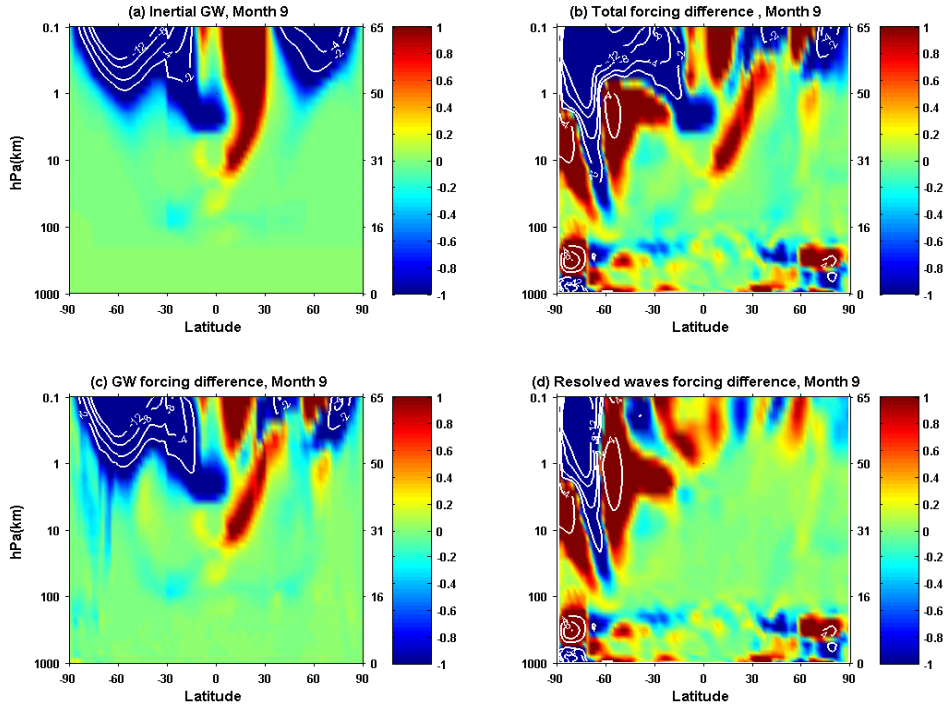

Figure E.9 Similar to Figure 4.14, for September

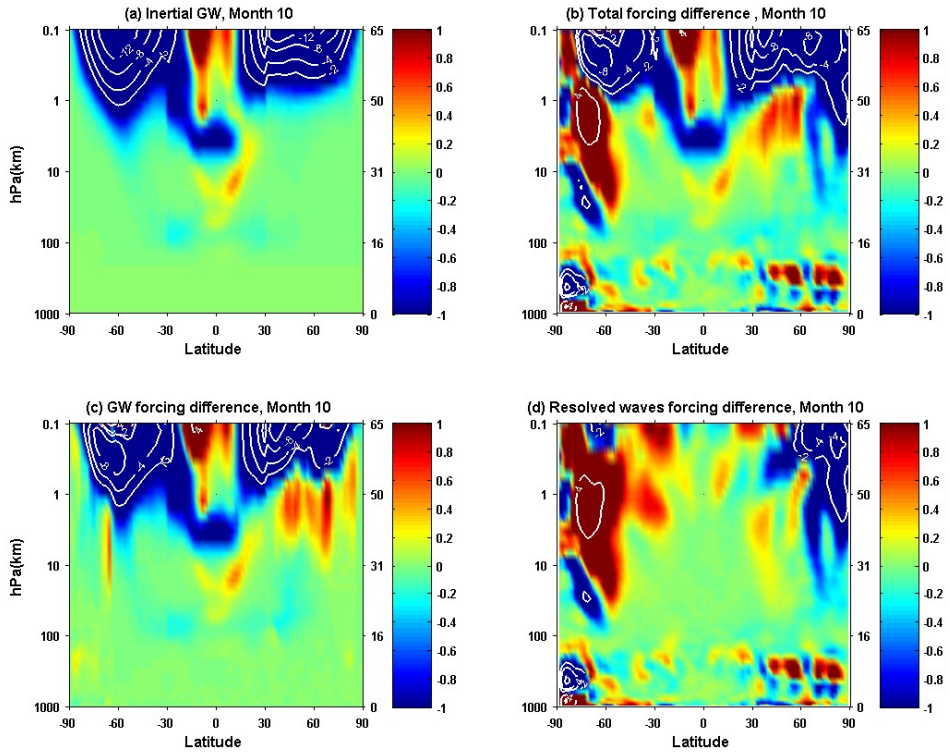

Figure E.10 Similar to Figure 4.10, for October

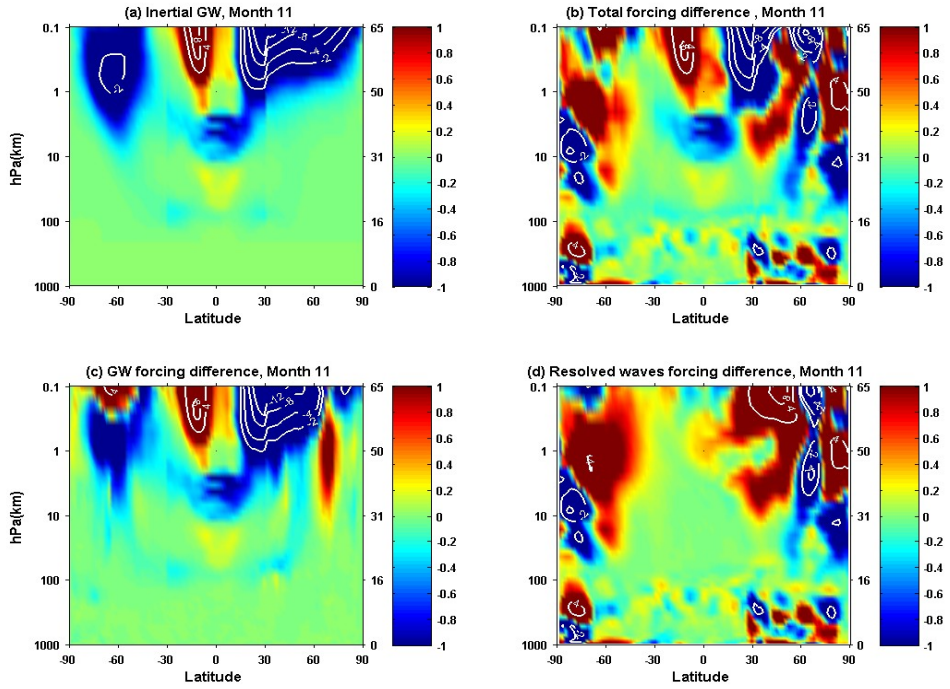

Figure E.11 Similar to Figure 4.14, for November

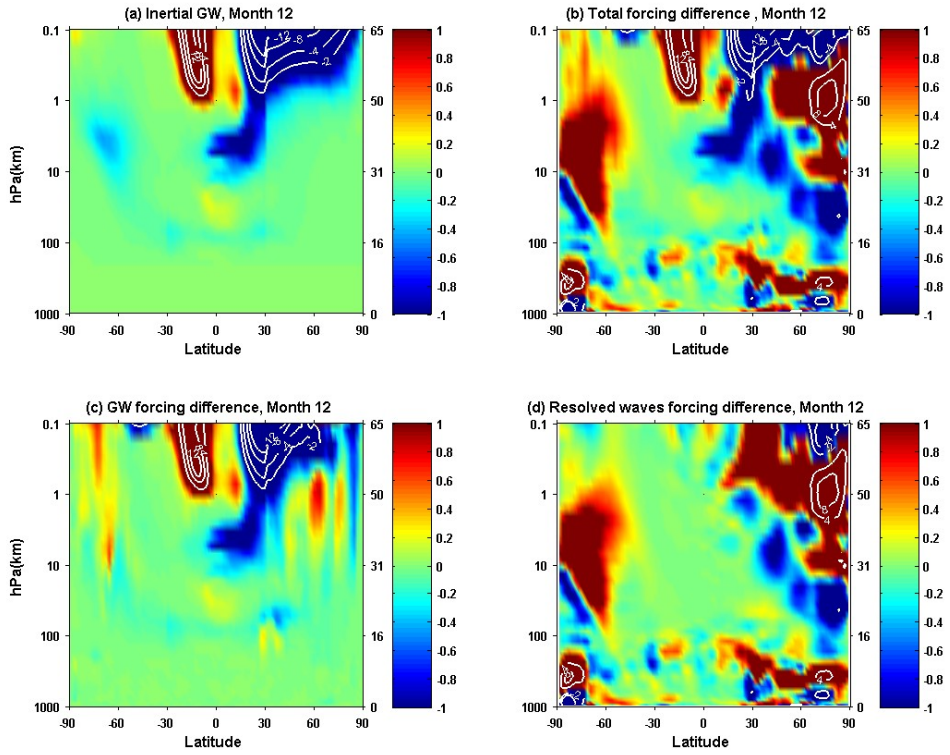

Figure E.12 Similar to Figure 4.14, for December